

HIGH ORDER PSEUDOHOMOLOGY USING  
ZONE PLATES

J. GUR

REPORT NO. 84  
DECEMBER 1978

## ABSTRACT

The reconstruction of pseudoholograms at high orders is investigated for the first time. The purpose of the work is to demonstrate the potential and the power of this new technique for obtaining high resolution x-ray images of imploded pellets in laser pellet-compression experiments. Considerable insight, to the high order focusing capability of zone plates, is gained by first studying the analogies between zone plates and diffraction gratings.

The formal mathematical framework of pseudoholography is then re-derived, this time including the reconstructions at high orders. Generalized expressions for planar and tomographic resolution, transverse and axial point spread functions are derived. The theoretical study predicts a practical submicron resolution. The limitations and prospects of the technique are discussed, and expressions for determining the effects of diffraction in the recording step of a pseudohologram are derived. Unconventional zone plate designs are introduced and the possible improvement of the high order reconstructions is discussed.

The effects of speckle noise in the high order reconstructions are studied. The granularity of the film as well as the serration introduced in the zone plate in the manufacturing process are treated. Three computer programs are used to investigate the transverse and axial performance of zone plates of different designs at various orders, and to simulate the recording and reconstruction of a pseudohologram. The dependence of the quality of the high order reconstructions on the object characteristics is demonstrated. By controlling the  $\gamma$  of the

film and the zone plate design, we can optimize the quality of the high order reconstructions of certain classes of objects. The possibility of using different coded apertures when the reconstruction is to be done digitally is discussed.

An optical simulation of imaging an x-ray source is described, which demonstrates the increase of resolution at higher orders. An extensive experimental study is described for investigating the effects of the  $\gamma$  of the recorded pseudohologram and of the imperfections in the zone plate mask on the quality of the reconstructions at high orders. The construction of an x-ray zone plate camera for laser pellet compression measurements is described. Results from some pellet compression experiments are shown demonstrating an increase of resolution at high orders. A resolution test for the zone plate camera is performed.  $8\mu\text{m}$  resolution in the first order and  $4\mu\text{m}$  resolution in the second order are demonstrated. The resolution in the third order is typically  $3\mu\text{m}$ . Finally, an optical simulation of an x-ray experiment is described showing the feasibility of using a one dimensional zone plate coded aperture to spatially resolved spectra.

TABLE OF CONTENTS

	<u>Page</u>
List of Tables .....	xi
List of Figures .....	xiii
List of Appendices .....	xviii
List of Symbols .....	xix
CHAPTER I: INTRODUCTION .....	1
1.1 References for Chapter I .....	15
CHAPTER II: THEORY .....	18
2.1 The analogy between zone plates and diffraction gratings .....	19
2.1.1 Width of principal orders .....	32
2.1.2 Chromatic resolving power .....	33
2.1.3 Dispersion .....	33
2.1.4 Illumination with a finite source .....	34
2.1.5 The effects of changing the zone shape or the slit shape .....	34
2.1.6 Conclusions from the calculations of the diffraction patterns for gratings and zone plates (Fig. 2.1.4 and Table 2.1.2) .....	36
2.1.7 Phase gratings and zone plates .....	40
2.1.8 Fluxes at higher orders .....	43
2.1.9 Scattering and noise in gratings and zone plates .....	43
2.1.10 Aberrations in zone plates .....	49
2.1.11 Computer simulations .....	52
2.1.11.1 Axial intensity distribution .....	52

TABLE OF CONTENTS, Cont.

	<u>Page</u>
2.1.11.1.1 A discussion regarding the computer program that calculates the axial intensity distribution .....	52
2.1.11.1.2 Conclusions from the plots obtained by the computer program .....	56
2.1.11.2 Transverse intensity distribution .....	63
2.1.11.2.1 Effect of the zone shape on the intensity distribution of various orders .....	63
2.1.11.2.2 The effective number of zones increases at higher orders .....	68
2.1.11.2.3 Comparison between one dimensional and two dimensional zone plates .....	70
2.1.12 References for section 2.1 .....	74
2.2 Limitations and prospects of pseudoholography ...	77
2.2.1 Propagation of the mutual intensity .....	78
2.2.2 High order reconstruction of a pseudohologram .	90
2.2.3 Transverse and axial width of the point spread function .....	97
2.2.4 The transverse resolution in the zone plate pseudoholographic technique .....	99
2.2.5 Tomographic resolution in the zone plate pseudoholographic technique .....	104
2.2.6 Efficiency of reconstructions at higher orders	106
2.2.7 The effects of zone width on the effective dynamic range .....	107
2.2.8 Noise .....	111
2.2.8.1 Quantum noise considerations .....	114

TABLE OF CONTENTS, Cont.

	<u>Page</u>
2.2.9 Methods of reconstruction .....	114
2.2.9.1 Optical methods .....	114
2.2.9.1.1 The direct reconstruction .....	115
2.2.9.1.2 Optical correlations .....	115
2.2.9.1.3 Optical deconvolutions .....	119
2.2.9.2 Digital reconstructions .....	122
2.2.9.3 Hybrid optical reconstructions .....	123
2.2.10 A comparison of the resolution at higher orders between imaging with zone plates and the zone plate pseudoholographic technique .....	123
2.2.11 Comments on one dimensional zone plates .....	125
2.2.11.1 Axial distribution .....	125
2.2.11.2 Transverse distribution .....	127
2.2.12 Computer simulations .....	127
2.2.12.1 Comments on using the propagation program for the investigation of diffraction effects in the recording step of a pseudohologram .....	130
2.2.12.2 Conclusions from the computer simulations ...	130
CHAPTER III: EXPERIMENTAL INVESTIGATION .....	140
3.1 Demonstration that higher resolution can be ob- tained in higher order reconstructions .....	141
3.2 Limitation on the object size .....	146
3.3 Studies of the high order reconstructions .....	150
3.3.1 Analysis of Fig. 3.8 .....	152

TABLE OF CONTENTS, Cont.

	<u>Page</u>
3.3.1.1 Effects of imperfections in the zone plate mask .....	152
3.3.1.2 Artifacts .....	154
3.3.1.2.1 Comparison between the odd and even order reconstructions .....	154
3.3.1.3 Effect of $\gamma$ .....	155
3.3.1.4 Central block .....	155
3.3.1.5 Reconstruction at very high orders .....	155
3.3.1.6 Effects of underexposure .....	156
3.4 Requirements on the zone plate camera .....	156
3.5 Calculation of the zone plate parameters for x-ray pseudoholography of pellet compression experiments .....	162
3.6 The construction of the zone plate camera .....	164
3.6.1 The zone plate used in the x-ray experiments ..	169
3.6.2 Sensitivity of the zone plate camera to misalignment .....	174
3.7 The problem of the destruction of the zone plate by extremely high intensities in laser fusion research .....	174
3.8 The resolution of the zone plate camera .....	176
3.9 Experimental results from laser pellet compression experiments .....	178
3.9.1 Experimental determination of the magnification of the zone plate camera .....	178
3.9.2 Discussion of the results .....	183
3.10 Using one dimensional zone plates for spatially resolved spectra of x-ray self luminous sources	189

TABLE OF CONTENTS, Cont.

	<u>Page</u>
3.11 References for Chapter III .....	200
CHAPTER IV: SUMMARY AND SUGGESTIONS FOR FURTHER INVES- TIGATIONS .....	201

LIST OF TABLES

	<u>Page</u>
1.1 Pinhole camera: Optimization .....	7
1.2 Pinhole camera: Optimization .....	8
1.3 Status of grazing reflection microscopes .....	10
1.4 Comparison between the different x-ray imaging techniques .....	13
2.1.1 Notation for Fresnel zone plates .....	28
2.1.2 Fraunhofer diffraction patterns of gratings and on axis amplitudes of zone plates .....	37
2.1.3 Normalization for zone plates and gratings .....	38
2.1.4 Parameters of the different computer runs, calculating the on axis intensity distribution from zone plates .....	57
2.1.5 Parameters describing the plots in Section 2.1.11.2	64
2.2.1 Parameters of different computer runs calculating the reconstruction of simulated pseudoholograms .	131
3.1 Attenuation of x-rays in different thicknesses of gold foils .....	163
3.2 Explanations to Fig. 3.11a .....	166
3.3 Parameters of the zone plate masters, shown in Fig. 3.12 .....	171
3.4 Parameters of the shots taken on Delta .....	179

LIST OF FIGURES

	<u>Page</u>
1.1 Recording a shadowgram of two point sources using a zone plate mask .....	3
1.2 Pinhole camera geometry .....	6
1.3 Formation of higher order images with a zone plate	11
2.1.1 Diffraction of a spherical wave through a zone plate	20
2.1.2 Formation of a zone plate by interference between two spherical waves .....	24
2.1.3a Cosinusoidal zone plates and Fresnel zone plates drawn in quadratic distance coordinates .....	25
2.1.3b Cosinusoidal zone plates and Fresnel zone plates drawn in real space coordinates .....	27
2.1.4 Amplitude transmission of various zone plates and gratings .....	35
2.1.5 Blazing of a zone plate .....	42
2.1.6 Grain noise in a zone plate .....	45
2.1.7 The serration in a zone plate .....	45
2.1.8 Noise function introduced by random fluctuations in the zone edges of a zone plate .....	47
2.1.9 Effects of noise on the diffraction pattern .....	48
2.1.10 At higher orders the zones get narrower and the effective number of zones gets larger .....	51
2.1.11 Relation between the extent of the input function and the output function when using the FFT algorithm on a sampled function .....	55
2.1.12 Definitions of all the relevant quantities used to represent a zone plate in the computer program ..	58
2.1.13 Axial intensity distribution of light focused by a zone plate of 37 zones: Ideal case and zones with slanted edges .....	59

LIST OF FIGURES, Cont.

	<u>Page</u>
2.1.14 Axial intensity distribution of light focused by a zone plate of 37 zones: Narrow sharp zones and narrow zones with slanted edges .....	61
2.1.15 Axial intensity distribution of light focused by a Fresnel zone plate of 11 zones .....	62
2.1.16 Transverse intensity distribution at various orders of light focused by a zone plate .....	65
2.1.17 Transverse intensity distributions focused by zone plates and a lens .....	69
2.1.18 Transverse intensity distributions from positive one dimensional zone plates .....	71
2.1.19 Transverse intensity distributions from negative one dimensional zone plates .....	72
2.2.1 The geometry for recording a pseudohologram ....	79
2.2.2 Explanation of how 2 projections from 2 different point sources of the same aperture produce the same shadows .....	80
2.2.3 Notation for the stationary phase calculation ..	87
2.2.4 An approximation for the spectrum of x-rays emitted from laser produced plasma .....	87
2.2.5 Notation for Fresnel propagation calculation through a slit of width $r$ .....	91
2.2.6 Recording of depth information with a coded aperture .....	91
2.2.7 The recording step of pseudoholographic technique	101
2.2.8 The reconstruction of a pseudohologram .....	102
2.2.9 Explanation of the reconstruction step .....	102
2.2.10 Derivation of the tomographic resolution of the pseudoholographic technique .....	105

LIST OF FIGURES, Cont.

	<u>Page</u>
2.2.11 The effect of narrowing the zones in a zone plate	108
2.2.12 Methods of optical reconstruction of a pseudo-hologram .....	116
2.2.13 Optical correlation using incoherent light .....	117
2.2.14 Coherent optical system for reconstructing pseudo-holograms .....	117
2.2.15 Optical deconvolution of pseudoholograms .....	120
2.2.16 Comparison between imaging with zone plates at higher orders and a reconstruction of a pseudo-hologram .....	124
2.2.17 Comparison between the sinc function and the $1/\sqrt{u}$ function in the case of one dimensional zone plates	126
2.2.18 Apodization of a one dimensional zone plate in order to achieve on axis intensity distribution, as in the two dimensional zone plate .....	126
2.2.19 Determination of the film size for the computer simulation .....	129
2.2.20 Notation for the source function used in the computer simulations .....	132
2.2.21 Reconstructions of simulated pseudoholograms of two point sources .....	134
2.2.22a Reconstructions of a simulated pseudohologram of two finite sources using 37-zone zone plate .....	135
2.2.22b Reconstruction of a simulated pseudohologram of two finite sources using 100-zone zone plate ....	136
3.1 The recording step of the pseudoholographic technique .....	142
3.2 Two masks used in the optical simulation experiments .....	143

LIST OF FIGURES, Cont.

	<u>Page</u>
3.3 Shadowgrams of two point sources .....	144
3.4 The reconstruction step .....	145
3.5 Experimental results of the optical simulation experiment .....	147
3.6 Moire fringes produced by two overlapping zone plates .....	149
3.7 Pseudoholography as a three stage process .....	151
3.8 Reconstructions along the optical axis .....	153
3.9 The overlap of two rings may produce a third ring	157
3.10 Effects of high aspect ratios .....	161
3.11a The design of the zone plate camera .....	165
3.11b Diagram of the vacuum tank .....	168
3.12 Some zone plate masters .....	170
3.13 The actual zone plate mounted on a Be foil .....	172
3.14 The zone plate camera .....	173
3.15 Illustration for computing the sensitivity of the zone plate camera to motion of the microballoon ..	175
3.16 Resolution test for the zone plate camera .....	177
3.17 Configurations for performing the resolution test	177a
3.18 Illustration for computing the magnification in the zone plate camera .....	180
3.19 Reconstruction of a microballoon .....	184
3.20 Reconstructions of a microballoon and of a stalk	185
3.21 Reconstruction of 8.6 At Ne filled microballoon .	187
3.22 0.195 gr/cc CD <sub>2</sub> microballoon .....	188

LIST OF FIGURES, Cont.

	<u>Page</u>
3.23 Double exposure of two CD <sub>2</sub> foams .....	190
3.24a The zone plate camera is in the plane of the four illuminating beams .....	191
3.24b Microballoon attached to a stalk .....	192
3.25 Experimental configuration for recording pseudo- holograms of spatially resolved spectra .....	193
3.26 Experimental configuration for optical simulation of simulation of pseudoholography of x-ray spa- tially resolved spectra .....	194
3.27 Linear pseudoholograms obtained from the simula- tion experiment described in Fig. 3.26 .....	195
3.28 Experimental results of the optical simulation experiment in spatially resolved spectroscopy ..	197
3.29 Experimental configuration for recording a streaked pseudohologram .....	199

LIST OF APPENDICES

	<u>Page</u>
APPENDIX 1: Listing of a computer program that calculates the on axis intensity distribution ...	205
APPENDIX 2: Listing of a computer program that simulates the propagation of optical field through an optical system .....	216
APPENDIX 3: Listing of a computer program that simulates the recording of a pseudohologram .....	229

LIST OF SYMBOLS

	<u>Page</u>
$a$ Aperture radius.....	19
$a$ Slit boundary.....	85
$a_i$ Amplitude of the field due to point source $i$ .....	109
$A$ Field constant .....	23
$A$ Extent of the input function .....	55
$A$ Radius of the zone plate .....	174
$A'$ Radius of the shadow of the zone plate .....	174
$A_1$ Amplitude of the light from source $S_1$ .....	23
$A_2$ Amplitude of the light from source $S_2$ .....	23
$A(t)$ Aperture function of a grating .....	34
$A(\Delta t)$ Discrete form of the aperture function .....	53
$A(\rho)$ Rotationally symmetric aperture function .....	22
$A'(\rho^2)$ Aperture function in $\rho^2$ domain .....	22
$b$ Slit boundary .....	85
$B_1$ Straight portion of a zone see fig. 2.1.12 .....	56
$B_2$ Straight portion of a zone see fig. 2.1.12 .....	56
$B(x)$ See definition in eq. (2.2.19) .....	86
$B_a(t)$ Amplitude transmittance of an individual zone .....	34
$\tilde{B}_a(u)$ Fourier transform of $B_a(t)$ .....	36
$B_p(t)$ Phase introduced by an individual zone .....	41
$\tilde{B}_p(u)$ Fourier transform of $B_p(t)$ .....	41
$c$ Constant .....	92
$C$ Field constant .....	19

LIST OF SYMBOLS , Cont.

	<u>Page</u>
C Contrast of a hologram or a pseudohologram .....	107
c' Constant .....	81
c'' Constant .....	88
c''' Constant .....	88
C <sub>p</sub> Coefficient determining the efficiency at high orders .....	93
C <sub>p</sub> <sup>1</sup> The coefficient in the special case of a rectangular zone .	106
C <sub>coh</sub> Contrast of a hologram obtained with coherent light .....	107
C <sub>inc</sub> Contrast of a pseudohologram obtained with incoherent light .....	109
Circ $\left[ \xi; \xi_N \right]$ Circular function of radius $\xi_N$ in the $\xi$ domain .....	93
d Ratio of S <sub>1</sub> to S <sub>2</sub> .....	93
d Defined by $\gamma = -2+d$ .....	95
d Radius of the source .....	158
D <sub>z</sub> Diameter of the zone plate .....	178
D <sub>ps</sub> Diameter of the pseudohologram .....	178
E(t) Random process .....	44
$\tilde{E}(u)$ Fourier transform of E(t) .....	46
E( $\xi$ ) Scalar field in the mask plane .....	78
E*( $\xi$ ) Scalar field behind the mask .....	78
E(a) Scalar field in the source plane .....	81
E(X <sub>r</sub> ) Scalar field in the reconstruction plane .....	94
EPS1 Width of the zone see fig. 2.1.12 .....	30
EPS2 Width of the zone see fig. 2.1.12 .....	30
ESCALE Scaling factor for computing the intensity .....	53

LIST OF SYMBOLS, Cont.

	<u>Page</u>
$f$ Transmission of the gold foil .....	159
$F$ 1st order focus of a zone plate .....	32
$F_M$ 1st order focus of Moire formed zone plate .....	148
$F_{ozp}$ 1st order focus of the original zone plate .....	148
$F_p$ The pth order focus of a zone plate .....	106
$\Delta F_p$ Depth of focus at the pth order .....	106
$F/\#$ The F-number of a zone plate or a lens .....	50
$F(X)$ Transmission of the ideal zone plate in X domain .....	111
$FRN$ { Fresnel transform .....	113
$g(t)$ Transmission of uniformly exposed grainy film .....	46
$\tilde{g}(u)$ Fourier transform of $g(t)$ .....	46
$g(\xi)$ Amplitude transmission of the mask .....	83
$G(u)$ Scalar field expressed in u domain .....	36
$G'(u)$ Scalar field neglecting constants .....	22
$G^1(u)$ Scalar one dimensional field .....	125
$G''(u)$ Scalar field neglecting constants and phase factors ....	31
$G(X)$ General expression for the shadow recorded in the pseudo- holographic technique, including diffraction effects ....	119
$G^1(m\Delta u)$ Discrete version of $G(u)$ .....	53
$G^1(\sigma, \phi)$ Scalar field diffracted from a circular aperture .....	22
$G(\theta)$ On axis field distribution in $\theta$ domain .....	93
$h$ Constant defined by eq. (2.2.26) .....	93
$H$ Radius of the source .....	19
$H$ Recorded pseudohologram of the test point source .....	120

LIST OF SYMBOLS, Cont.

	<u>Page</u>
$h(\alpha, X_r, p)$ Spread function .....	96
$h(\alpha, X_r, p, m)$ Spread function .....	97
$h'(\alpha, X_r, p)$ One dimensional spread function for one dimensional pseudoholographic technique .....	127
$I$ Intensity of the interferogram recorded on film .....	23
$I(k)$ Notation for the integral calculated by the stationary phase method .....	86
$I(\alpha)$ Radiant intensity of the source .....	82
$I(X)$ Intensity due diffraction effects .....	88
$I(X)$ Recorded intensity on film .....	94
$I(mX)$ Demagnified version of $I(X)$ .....	97
$I'(X_r)$ Reconstructed amplitude proportional to image intensity	119
$\tilde{I}(u)$ Scalar field proportional to the Fourier transform of $I(X)$	118
$\tilde{I}'(u)$ Filtered version of $I(u)$ .....	118
$I(m\Delta u)$ Discrete version of the intensity in $u$ domain .....	53
$I_R(X)$ Reconstructed intensity by the correlation method.....	118
$I(m\Delta \xi)$ Discrete version of the intensity in $\xi$ domain .....	54
$J_0(\ )$ Bessel function of order 0 .....	22
$J_1(\ )$ Bessel function of order 1 .....	97
$k$ Wave vector .....	19
$2l+1=p$ Order number (see eq. (2.1.17) ) .....	31
$l_1$ Distance from the 1st order focus to the 1st edge of a zone	51
$l_2$ " " " " " " " " 2nd " " " "	51

LIST OF SYMBOLS, Cont.

	<u>Page</u>
$l_3$ Distance from the 3rd order focus to the 1st edge of a zone	51
$l_2$ " " " " " " " " 2nd " " " "	51
$L$ Tomographic resolution at 1st order .....	104
$L_p$ Tomographic resolution at pth order .....	158
$1/m$ Demagnification of the pseudohologram .....	97
$\Delta m$ Error in the magnification .....	181
$M$ Fineness of the zones in a zone plate .....	110
$M(\xi)$ Intensity transmittance of the mask in the $\xi$ domain .....	78
$M(\theta)$ Intensity transmittance of the mask in the $\theta$ domain .....	106
$M(X)$ Intensity transmittance of the mask in the $X$ domain .....	118
$\tilde{M}(u)$ Fourier transform of $M(X)$ .....	118
$N$ Number of point sources in the object .....	109
$N$ Number of zones .....	31
$N_g(X)$ Grain noise function .....	111
$\tilde{N}_g(u)$ Fourier transform of $N_g(X)$ .....	111
$NZONE$ Total number of zones (both clear and opaque) .....	31
$O(X)$ Radiant Intensity of the object .....	118
$\tilde{O}(u)$ Fourier transform of $O(X)$ .....	118
$p$ Order number .....	94
$q$ Zone plate constant in $t$ domain $q=1/\sqrt{NZONE}$ .....	30
$Q$ Zone-plate constant in real space domain $Q=1/\sqrt{NZONE}$ .....	26

LIST OF SYMBOLS, Cont.

	<u>Page</u>
$r$ Width of the outermost zone .....	90
$r'$ Width of the outermost zone on the shadowgram .....	100
$r''$ " " " " " " " " demagnified version of shadowgram .....	103
$r_1$ Distance from point $(X_0, Y_0)$ to point $(X_1, Y_1)$ .....	19
$r_2$ " " " $(X_0, Y_0)$ " " $(X_2, Y_2)$ .....	19
$r_n$ Radius of the $n$ th zone center .....	42
$r_n^0$ Radius of an ideally smooth zone edge .....	44
$r_n(\phi)$ Radius of a real zone edge as a function of $\phi$ .....	44
$R_1$ Distance from the source center to the mask center .....	19
$R_2$ Distance from the mask center to the shadowgram center ....	19
$R_1$ Distance from point source $S_1$ to the film .....	23
$R_2$ " " " " $S_2$ " " " .....	23
$R$ Distance between two sharp clear zones .....	110
$\Delta R$ Width of a sharp clear zone .....	110
$\Delta R_2$ Dispersion along the axis .....	33
$R_{10}$ Axial distance from source $S_1$ to the film .....	23
$R_{20}$ " " " " $S_2$ " " " .....	23
$R_N(\tau)$ Correlation function of the grain noise .....	112
$R_{NEVEN}$ Radius of an even zone edge in a negative zone plate ...	26
$R_{NODD}$ " " " odd " " " " " " " " ...	26
$R_{PEVEN}$ " " " even " " " " " " " " ...	26
$R_{PODD}$ " " " odd " " " " " " " " ...	26
$R(X)$ Defined in eq. (2.2.20) .....	86
$Rect[t;q]$ Rectangular function of diameter $2q$ in the $t$ domain	30

LIST OF SYMBOLS, Cont.

	<u>Page</u>
$S_1$ Area of the Airy disc in the 1st focus .....	43
$S_2$ " " " " " " " 2nd " .....	43
$S_1$ Distance from source plane to mask plane .....	80
$S_2$ " " mask " " film " .....	80
S Extent of the source see fig. 2.2.10 .....	104
$S_N(u)$ Fourier transform of $N_g(X)$ .....	112
$S(X)$ Serration function .....	111
t Quadratic distance coordinate .....	21
t Thickness of the gold foil .....	159
t Variable change .....	95
T Transmission of a developed pseudohologram .....	94
T The finest resolved detail in the source .....	100
$T'$ The separation between the two projected zone plate centers on the shadowgram .....	100
$T''$ The separation between the centers in the reduced shadow- gram .....	100
$t_0$ Constant transmission of the shadowgram.....	94
$\Delta t$ Sampling distance in the t domain .....	53
$T_p$ The resolution at the pth order .....	164
TOTD Width of the input space .....	53
TBD: " " " output " .....	130
u See eq.(2.1.4) most often used .....	21
u See eq.(2.1.10) .....	23
u See eq. (2.2.38) .....	98
u See eq. (2.2.42) .....	99

LIST OF SYMBOLS, Cont.

	<u>Page</u>
$\Delta u$ Sampling distance in $u$ domain .....	53
USCALE Scaling factor for calculating the coordinate in $u$ domain .....	53
USCALE( $\bar{\xi}$ ) Scaling factor for the coordinate in $\bar{\xi}$ domain .....	54
$v$ See eq. (2.1.7) .....	21
$\Delta v$ Fresnel number see eq.(2.2.23) .....	90
$W(u)$ Power spectrum of the noise .....	112
$w$ Number for determining the sharpness of the zone .....	110
$X$ Distance on the film .....	23
$X_0$ Coordinate in the mask plane .....	19
$X_1$ " " " source plane .....	19
$X_2$ " " " film " .....	19
$X_a$ Lower limit of the aperture .....	19
$X_b$ upper " " " " .....	19
$\Delta X$ Width of the principal order .....	33
$X_r$ Coordinate in the reconstruction plane .....	94
$\Delta X_r$ Width of the point spread function .....	99
$X_w$ Half width of the zone .....	110
$Y_0$ Coordinate in the mask plane .....	19
$Y_1$ " " " source " .....	19
$Y_2$ " " " film " .....	19
$Y_a$ Lower limit of the aperture .....	19
$Y_b$ Upper " " " " .....	19

LIST OF SYMBOLS, Cont.

	<u>Page</u>
Z Distance along the optical axis from the zone plate .....	33
Z(t) Transmission of a real zone plate .....	44
Z <sup>0</sup> (t) Transmission of an ideal Fresnel zone plate .....	44
$\tilde{Z}(u)$ Fourier transform of Z(t) .....	46
$\tilde{Z}^0(u)$ Fourier transform of Z <sup>0</sup> (t) .....	46
Z <sub>1</sub> Distance from zone plate to 1st focus .....	96
Z <sub>p</sub> " " " " " pth " .....	95
$\Delta Z$ Depth of focus at the 1st focus .....	98
$\Delta Z_p$ " " " " " pth " .....	98
$\Delta Z$ Axial width of the spread function .....	99
$\alpha$ Angle see fig. 2.1.5 .....	42
$\alpha$ Source coordinate .....	78
$\alpha(\lambda)$ Absorption coefficient of gold .....	159
$\beta$ Angle see fig. 2.1.5 .....	42
$\beta$ Constant that accounts for the fact that the separation between the zones is not constant .....	110
$\gamma$ Angle see fig. 2.1.5 .....	42
$\gamma$ The slope of the H&D curve .....	94
$\Gamma$ Aspect ratio of a zone .....	160
$\Gamma(X_1, X_2)$ Mutual intensity function at the mask plane .....	81
$\Gamma(a_1, a_2)$ " " " " " source plane .....	81
$\delta$ ) Delta function .....	30
$\delta$ Sampling interval .....	54

LIST OF SYMBOLS, Cont.

	<u>Page</u>
$\delta$ Shift in the location of the microballoon .....	174
$\delta$ Shift of the shadowgram .....	174
$\delta_n(r_n)$ Random variable describing the deviation from an ideal zone plate .....	44
$\delta_n(r_n, \phi)$ The random variable is a function of $\phi$ too .....	44
$\zeta$ Normalized coordinate along the optical axis .....	53
$\bar{\zeta}$ Coordinate proportional to $1/\zeta$ .....	54
$\Delta\bar{\zeta}$ Sampling interval in the $\bar{\zeta}$ domain .....	54
$\zeta(t)$ Random process describing the serration in the zone plate	46
$\eta$ Measured magnification .....	181
$\Delta\eta$ Error in $\eta$ .....	181
$\theta$ Azimuth angle in the mask plane .....	19
$\theta$ Distance square coordinate .....	23
$\theta$ Angle see fig. 2.2.10 .....	104
$\theta_j$ Range of $\theta$ that belong to the $j$ th open zone.....	26
$\lambda$ Radiation wavelength .....	19
$\mu$ Geometrical factor eq. (2.2.11) .....	83
$\xi$ Coordinate in the mask plane .....	78
$\xi_0$ Stationary phase point.....	84
$\xi_1$ Radius of the innermost zone (normalized quantity) .....	93
$\xi_N$ " " " outermost " " " .....	93
$\xi'$ Unnormalized coordinate on the mask .....	93

LIST OF SYMBOLS, Cont.

	<u>Page</u>
$\xi_N$ Unnormalized radius of the outermost zone .....	100
$\xi_N^f$ Radius of the outermost zone projected on the film .....	100
$\xi_N^d$ Radius of the outermost zone on the demagnified shadowgram ..	103
$\Delta\xi_N$ Change in the projected outermost zone due to axial motion of a point source .....	104
$\rho$ Normalized radial coordinate on the mask .....	19
$\sigma$ Radial coordinate on the film .....	19
$\sigma$ Width of a Gaussian zone .....	35
$\phi$ Azimuth angle in the film plane .....	19
$\phi_1$ Phase of source $S_1$ .....	23
$\phi_2$ " " " " $S_2$ .....	23
$\phi_i$ Phase of the field at the hologram due to point source $i$ ..	109
$\Delta\phi$ Phase between two point sources .....	23
$\phi(j,q)$ Discrete random process .....	44
$\phi(\xi)$ Phase function .....	83
$\phi'(\xi_0)$ 1st derivative of $\phi(\xi)$ at $\xi_0$ .....	83
$\phi''(\xi_0)$ 2nd derivative of $\phi(\xi)$ at $\xi_0$ .....	83
$\chi$ Defined in eq. (2.1.7) .....	21
$\Omega$ Cone angle of the focussed beam .....	100
$\Omega_1$ Cone angle at the 1st focus .....	43
$\Omega_2$ " " " " 2nd " .....	43
$(1/\alpha)_p$ Reciprocal of the cone angle at the pth focus .....	104

CHAPTER I

INTRODUCTION

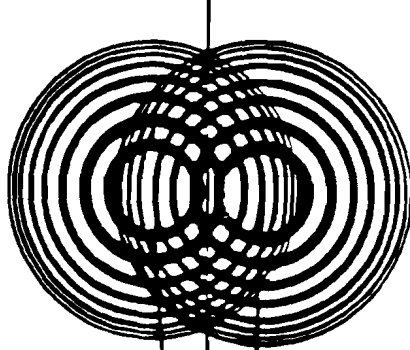
There are two basic approaches to pseudoholography which is frequently called incoherent holography in the literature ([1.1], [1.2], [1.3], [1.4]). In one approach (described in [1.1] and [1.2]) an optical instrument is used to form two images of every point in the object. These two images are coherent with respect to each other, hence they can form interference fringes on a photographic plate. The pseudohologram is thus built up of an incoherent superposition of interference fringes originating from all the points of the object.

In the second approach, which is referred to as coded aperture imaging ([1.5], [1.6], [1.7]), each point in the object casts a shadow of an aperture (a cone plate, an annular aperture, etc.) onto a piece of film (see Fig. 1.1). The pseudohologram in this case is built up of an incoherent superposition of shadows cast by all the points of the object.

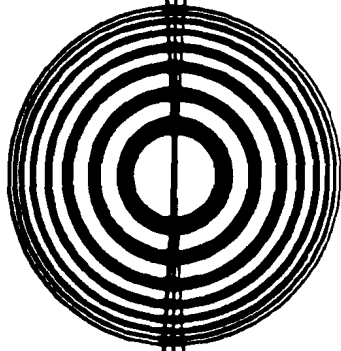
In both approaches the object (which is illuminated by an incoherent\* source, or is an incoherent source itself such as a plasma or a flame), is considered as a collection of point sources which are incoherent with respect to each other. Furthermore, in both methods the pseudohologram is sensitive to the distance of the object from the aperture, or the appropriate optical instrument, and therefore depth information is recorded as well as intensity information. Both methods are two step procedures in which the second step, the reconstruction step, may be performed either optically or digitally. So

\*we will use the term incoherent source although it is rigorously a non physical entity

**SHADOWGRAM**



**ZONE PLATE MASK**



A  
B

**Fig. 1.1**  
**Recording of a shadowgram of two point sources using a zone plate mask.**

far, there has not been any practical application using the first method because of the limitation of being able to record only a small number of points. An improvement has been proposed (Ref. [2.2.11]) to increase the number of points considerably using, instead of the usual two beam interferometer, a lensless Fabry Perot interferometer. Further investigations should be carried out in order to determine whether high quality pseudoholograms can be obtained using this method. Since optical elements such as a beam splitter or a Fabry Perot etalon cannot be constructed for the x-ray region this technique is useless for x-ray investigations.

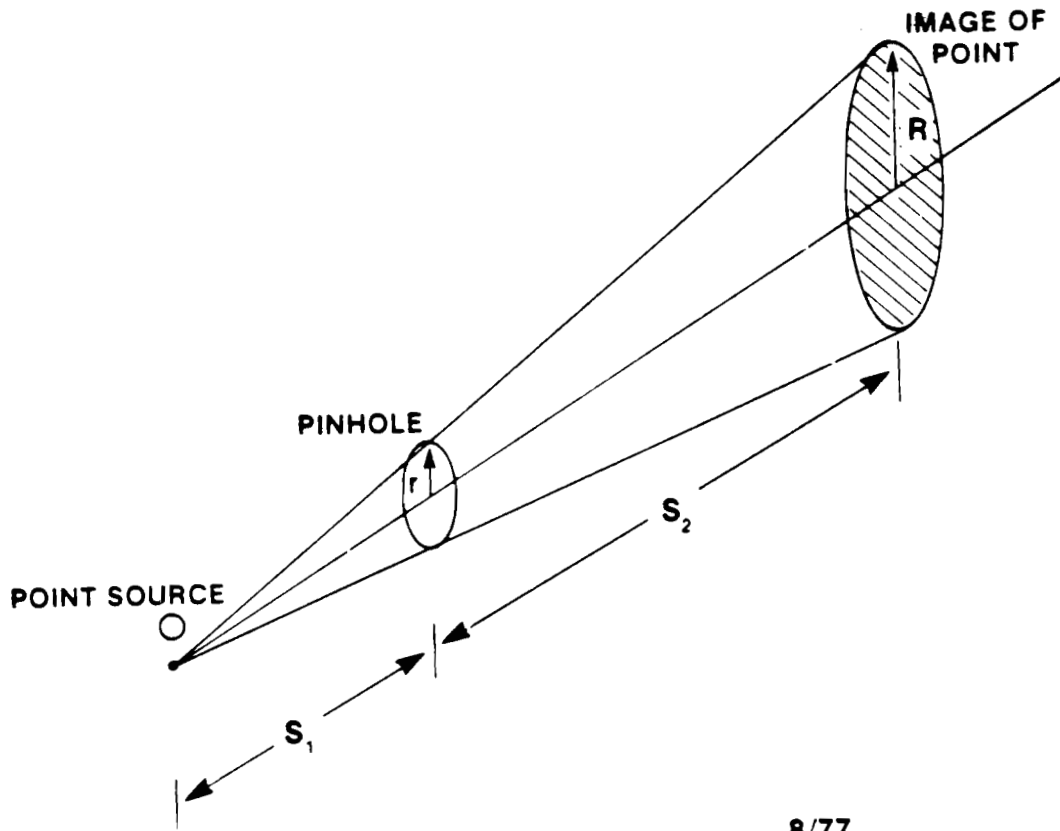
The second method, on the other hand, is not limited to the visible region; in fact, it is most useful in the x-ray region and with nuclear particles where no efficient imaging instrument exists. A useful application of this technique is imaging laser produced plasmas. At the University of Rochester there is a large program devoted to the Laser Fusion Feasibility Project. The experiments reported in this work were performed with a four beam  $\text{Nd}^{+3}$ :glass laser system (DELTA) that was in operation for four years for the purpose of producing high energy density plasmas by compressing gas filled microballoons. On typical shots, the laser delivered 7-10J on the target and the pulse width was typically 30 picoseconds. When the intense laser light hits the glass shell the surface evaporates immediately and the ablated material speeds outward. The associated reaction force drives the remainder of the shell and the gas fill inward and causes compression.

In proposed laser driven pellet compression experiments using a multibeam multi-kilojoule laser it is anticipated that the dimension of the high temperature compressed core will be of the order of  $1\mu\text{m}$ . Three types of instruments are now being used to get spatial information on the x-ray radiation emitted from the core in such experiments:

- (a) The pinhole camera
- (b) The x-ray grazing incidence microscope
- (c) The Fresnel zone plate.

(a) The pinhole camera (Fig. 1.2) is a standard diagnostic tool in laser produced plasma research because it is simple, insensitive to alignment, has a large field of view, is achromatic and relatively inexpensive. The resolution of the pinhole camera is of the order of the pinhole diameter.  $5\mu\text{m}$  seems to be the smallest practical diameter. For a smaller diameter, in order to employ the pinhole optimally, see Tables 1.1 and 1.2, the pinhole would have to be located so close to the microballoon that it will interfere with the target illumination system. Furthermore, for imaging x-rays, the thickness of the foil, in which the pinhole is made, has to be of the order of  $5\mu\text{m}$  and even thicker for hard x-rays to be sufficiently opaque. For high resolution such pinholes are not planar masks; for example  $1\mu\text{m}$  pinhole in a  $5\mu\text{m}$  thickness sheet of gold would be a very long tunnel, which will cause shadowing and scattering problems.

(b) The grazing incidence x-ray microscope is an extremely expensive instrument. It employs either two orthogonally oriented cylindrical mirrors [1.8] or a system of confocal coaxial ellipsoidal and hyper-



8/77

Fig. 1.2

**PINHOLE CAMERA GEOMETRY** UP  
LLE 

**Table 1.1**  
**PINHOLE CAMERA: OPTIMIZATION**

(Notation as in Fig. 1.2)  
from ref [2.2.7]

$$r_{\text{opt}}^2 = 0.9 \lambda \left( \frac{S_1 S_2}{S_1 + S_2} \right)$$

R set by resolution of recording medium,

$$R \geq 25 \mu\text{m}$$

$$\frac{R}{r} \cong \frac{S_2}{S_1} = M, \quad \text{magnification}$$

$$\begin{aligned} r_{\text{opt}}^2 &= 0.9 \lambda S_1 \left( \frac{S_2/S_1}{1 + S_2/S_1} \right) \\ &= 0.9 \lambda S_1 \left( \frac{M}{1 + M} \right) \end{aligned}$$

Typically,  $M \geq 5$  so

$$S_{1\text{opt}} > \frac{r_{\text{opt}}^2}{0.9 \lambda}$$

Table 1.2

**PINHOLE CAMERA : OPTIMIZATION** 

**EXAMPLES :**

$\lambda = 6 \text{ \AA}$  ( $h\nu \sim 2 \text{ KeV}$ )

$2r$ ( $\mu\text{m}$ )	10	6	2	1
$S_1$ (cm)	4.6	1.7	0.2	0.05

$\lambda = 1 \text{ \AA}$  ( $h\nu \sim 12 \text{ KeV}$ )

$2r$ ( $\mu\text{m}$ )	10	6	2	1
$S_1$ (cm)	25	9.1	1.0	0.25

**NOTE :  $2r$  IS APPROXIMATE RESOLUTION IN OBJECT SPACE**

holoidal mirrors [1.9]. The resolution of this system seems to be limited by surface roughness. For reflecting surfaces with  $50\text{\AA}$  rms roughness, calculations show that the resolution is about  $1-2\mu\text{m}$  [1.10]. A practical device [1.10], however, is reported to have  $3-5\mu\text{m}$  resolution. The instrument is also limited to wavelengths  $>2\lambda$ , hence no hard x-ray image or  $\alpha$ -particle image can be obtained in this way. The grazing incidence angle is of the order of  $1^\circ$  at this angle the aberrations become so severe that the field of view becomes exceedingly small and the alignment becomes very difficult. A summary of different x-ray grazing incidence microscopes is given in Table 1.3.

(c) The zone plate is being used in two modes of operation: 1. imaging mode and 2. shadowgraphy mode.

1. The imaging mode (see Fig. 1.3).

The zone plate has been used as a focussing device for imaging stellar x-ray sources [1.11]. In Ref. [1.12] a description of the use of a zone plate as an x-ray lens is given. Currently zone plates are made for imaging soft x-rays with resolution of the order of  $0.5\mu\text{m}$  with quasi monochromatic radiation like synchrotron radiation [1.13]. They can be manufactured by an interferometric technique with extremely high number of zones (1000-2000) and can be corrected for spherical aberration by using an aspheric wavefront in the interferometer [1.14]. Furthermore, we do not need to make the zones completely opaque [1.15], because the phase shift introduced by partially transparent metallic zones will always improve image forming efficiency. We can also blaze the zones in an analogous manner to that of a grating, and get high

**Table 1.3**  
**STATUS OF GRAZING REFLECTION MICROSCOPES** 

<u>FOCUSING SYSTEM</u>	<u>LIMITING ABERRATION</u>	<u>PRACTICAL RESOLUTION</u>	<u>PRACTICAL FIELD OF VIEW</u>
<b>ONE MIRROR :</b>			
1. Spherical	Astigmatism	—	—
2 Ellipsoidal (Wolter)	Spherical	10 $\mu$ x 40 $\mu$	—
<b>TWO MIRROR :</b>			
1. Kirkpatrick-Baez	Spherical	3 $\mu$	200 $\mu$
2. Aspherical (Wolter)	Coma	N.A.	300 $\mu$
3. Wolter-Schwarzschild	Field Curvature	N.A.	N.A.
<b>COMPOUND MIRROR :</b>			
1. 3-Mirror	N.A.	N.A.	N.A.
2. 4-Mirror	N.A.	N.A.	N.A.

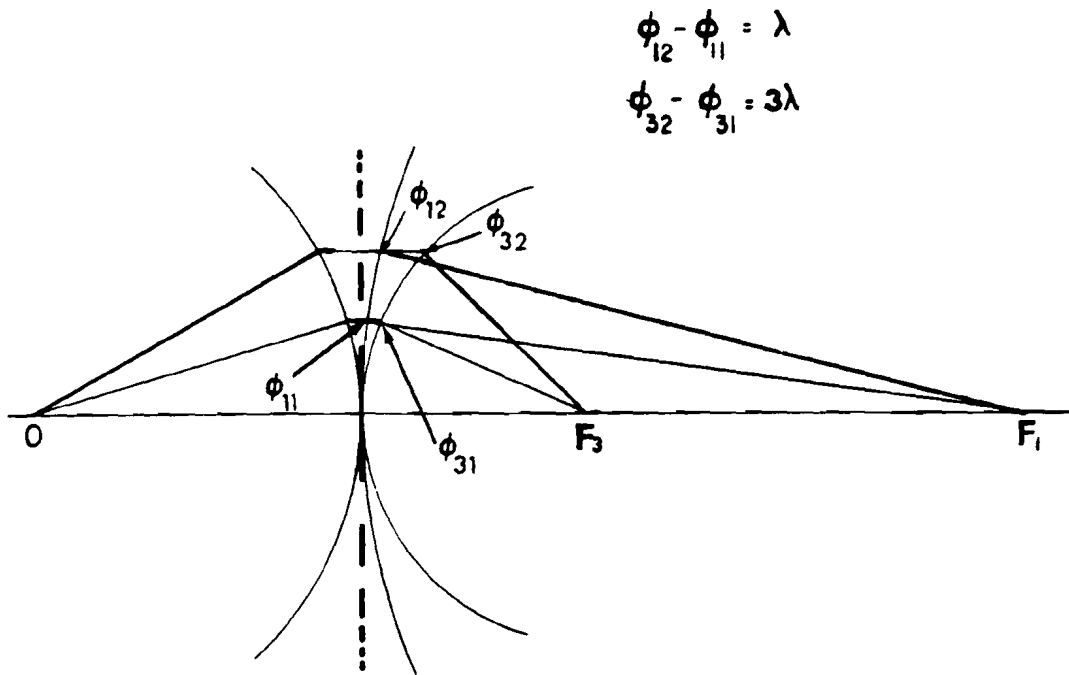


Fig. 1.3

**FORMATION OF HIGHER ORDER  
IMAGES WITH A ZONE PLATE**



efficiency at a specific order. Laser produced plasmas emit a broad spectrum; and since the zone plate focal length is inversely proportional to the focal length (as will be discussed later) the dispersion is so great that direct imaging is impractical. In addition, it is not useful for particles or hard x-rays, it is sensitive to alignment and has a limited field of view. In spite of a few claims for improving the resolution in higher order imaging [1.14], [1.16], it will be shown that this is not possible in the imaging mode and the resolution is determined by the width of the outermost zone.

2. Coded aperture mode. Merz [1.19] was the first to use the zone plate in the coded aperture mode for imaging stellar x-ray sources. This technique was then applied to nuclear medicine [1.20] by H. H. Barrett. However, the latter results were not very attractive because the imaged object was too large for the zone plate. (The limit on the object size is of the order of the size of the innermost zone.) Ceglio [1.21] applied this technique to the investigation of laser produced plasmas, the application of concern to us.

In our study we have analyzed various features of coded aperture imaging including the resolving power in higher order reconstructions, and the limitations of the method including grain noise in the film, diffraction effects, and fabrication defects in the zone plate mask. We find that improved resolution is achieved in high order reconstructions, and that contrary to a previous report [1.18] diffraction effects are not, in principle, the limitation in resolution when recording a soft x-ray spectrum.

In Table 1.4 a comparison between all the methods reviewed here

	PINHOLE CAMERA	GRAZING INCIDENCE MICROSCOPE	ZONE PLATE IMAGING	ZONE PLATE PSEUDO-HOLOGRAPHY
Practical resolution	5 $\mu\text{m}$	3-5 $\mu\text{m}$	0.3 $\mu\text{m}$	1 $\mu\text{m}$
Resolution limited by	Pinhole size	surface roughness	outermost zone	speckle noise
Distance from target	$\lesssim 1$ cm	$\gtrsim 10$ cm	$\gtrsim 10$ cm	$\lesssim 1$ cm
Sensitivity to alignment	insensitive	very sensitive	very sensitive	insensitive
Field of view	large (1-3 mm)	small (200 $\mu\text{m}$ )	small (200 $\mu\text{m}$ )	large (1-3 mm)
Restriction on target diameter	none	$\gtrsim$ field of view	$\gtrsim$ field of view	$\geq$ innermost zone
Spectral region	$\lambda < 7\text{\AA}$ ; Nuc. rad.	$\lambda > 2\text{\AA}$ ; No nuc. rad.	$\lambda > 1\text{\AA}$ ; No nuc. rad.	$\lambda \leq 7\text{\AA}$ ; Nuc. rad.
Chrom. aberration	none	none	very severe	none
No. of steps in process	real time photog. image	real time photog. image	Real time photog. image	two-step process
Spectral region limited by	diffraction	materials for grazing incidence	manufacturing problems	diffraction
Tomographic capability	none	none	none	moderate tomographic resolution
Cost	\$1,000	\$250-500 K	\$2,000	\$2,000

Table 1.4  
COMPARISON BETWEEN THE DIFFERENT X-RAY IMAGING TECHNIQUES

is given.

We will first present an analogy between zone plates and gratings. Then the coded imaging technique will be analyzed stressing its potential at higher order reconstructions. Also, the possibility of using different coded apertures when the reconstruction is to be done digitally will be discussed. An optical simulation of imaging an x-ray source is then described, which demonstrates the increase of resolution at higher orders. The construction of an x-ray zone plate camera for laser pellet compression measurements is described. Results from some pellet compression experiments are shown demonstrating an increase of resolution at higher orders. The potential of one dimensional zone plate coded aperture is then discussed. Finally, an optical simulation of an x-ray experiment is described, showing the feasibility of applying the idea to spatially resolved spectra.

1.1 REFERENCES

- 1.1 G. Cochran, "New Method of Making Fresnel Transformations with Incoherent Light", J. Opt. Soc. Am. 56, 1513 (1966).
- 1.2 A. W. Lohmann, "Wavefront Reconstruction for Incoherent Objects", J. Opt. Soc. Am. 55, 1555 (1965).
- 1.3 H. R. Worthington, Jr., "Production of Holograms with Incoherent Illumination", J. Opt. Soc. Am. 56, 1937 (1966).
- 1.4 Tadao Tsuruta, "Holography with Extended Incoherent Source", J. Opt. Soc. Am. 60, 47 (1970).
- 1.5 H. J. Caulfield and A. D. Williams, "An Introduction to Holography by Shadow Casting", Opt. Eng. 12, 3 (1973).
- 1.6 H. H. Barrett and D. T. Wilson, G. D. "Fresnel Zone Plate Imaging in Radiology and Nuclear Medicine", Opt. Eng. 12, 8 (1973).
- 1.7 W. L. Rogers, L. W. Jones, W. H. Beierwalters, "Imaging in Nuclear Medicine with Incoherent Holography", Opt. Eng. 12, 13 (1973).
- 1.8 F. Seward, J. Dent, M. Boyle, L. Koppel, T. Harper, P. Stoermy, and A. Toor, "Calibrated 'Four Color' X-Ray Microscope for Laser Plasma Diagnostics", Sci. Instrum. 47, 464 (1976).
- 1.9 R. C. Chase, J. K. Silk, "Ellipsoid - Hyperboloid X-Ray Imaging Instrument for Laser Pellet Diagnostics", Appl. Opt. 14, 2094 (1975).
- 1.10 M. J. Boyle, "Grazing Incidence X-Ray Microscopy of Laser Fusion Targets", SPIE 106 X-Ray Imaging 86 (1977).

- 1.11 J. H. Dijkstra, W. deGraaf and L. J. Lontwaard, "Construction of Apodised Zone Plates for Solar X-Ray Image Formation", in *New Techniques in Space Astronomy*, ed. F. Labuhn and R. Lust IAU Symposium (Reidel Dordrecht, Netherland) 41, 207 (1971).
- 1.12 N. M. Ceglio, "Tomography of Laser Fusion Plasmas", 8th International Conference on X-Ray Optics and Microanalysis and 12th Annual Conference of the Microbeam Analysis, Boston, Massachusetts (1977). p. 57A.
- 1.13 B. Niemann, D. Rudolph and G. Schmahl, "X-Ray Microscopy with Synchrotron Radiation", *Appl Opt.* 15, 1883 (1976).
- 1.14 G. Schmahl, D. Rudolf and B. Niemann, "X-Ray Microscopy of Biological Specimens with Zone Plates and Synchrotron Radiation", 8th International Conference on X-Ray Optics and Microanalysis and 12th Annual Conference of Microbeam Analysis, Boston, Mass. (1977). p. 57A.
- 1.15 J. Kirtz, "Thin Zone Plates for Soft X-Rays", 8th International Conference on X-Ray Optics and Microanalysis and 12th Annual Conference on Microbeam Analysis, Boston, Mass. (1977). p. 59A.
- 1.16 Germain Boivin, "Use of a Fresnel Zone Plate for Optical Image Formation with Short Wavelength Radiations", *Appl Opt.* 16, 1071 (1977).
- 1.17 N. M. Ceglio, "X-Ray Microscopy of Laser Fusion Plasmas Using Coded Imaging Techniques", *SPIE 106 X-Ray Imaging* 55 (1977).
- 1.18 N. M. Ceglio, D. T. Atwood and E. V. George, "Zone Plate Coded Imaging of Laser Produced Plasmas", *J. Appl. Phys.* 48, 1566 (1977).

- 1.19 L. Mertz and N. O. Young, "Fresnel Transformation of Images", Proc. Int. Conf. on Opt. Instr., London 305 (1961).
- 1.20 H. H. Barrett, J. Nucl. Med. 13, 382 (1972).
- 1.21 N. M. Ceglio, "Zone Plate Coded Imaging on a Microscopic Scale", J. Appl. Phys. 48, 1563 (1977).

CHAPTER II

THEORY

## 2.1 The analogy between zone plates and diffraction gratings.

Consider the system in Fig. 2.1.1. A spherical wave is diffracted by a mask  $A(X_0, Y_0)$ . Using the Fresnel Kirchhoff integral (see Ref. [2.1.1] page 382) we can write the amplitude at any distance  $Z$  from the diffracting aperture. Assuming small angles (less than  $30^\circ$ ) we can neglect the obliquity factor in the integral. Also, for a fixed  $Z$  the change in  $1/r_1$  and  $1/r_2$  over the range of integration is negligible compared to the change of the phase, so we replace these terms by the axial values  $1/R_1$  and  $1/R_2$  of  $1/r_1$  and  $1/r_2$  respectively and write them outside the integral. The amplitude  $G(X_2, Y_2)$  is then:

$$G(X_2, Y_2) = \frac{iC}{\lambda R_1 R_2} \int_a^b \int_a^b A(X_0, Y_0) e^{iK(r_1+r_2)} dx_0 dy_0 \quad (2.1.1)$$

where  $r_1$  is the distance between a point on the plane  $(X_0, Y_0)$  and a point on the plane  $(X_1, Y_1)$ ,  $r_2$  is the distance between a point on the plane  $(X_0, Y_0)$  and a point on the plane  $(X_2, Y_2)$ ,  $K$  is the wave number, and  $C$  is a constant. Expanding  $r_1$  and  $r_2$  in the exponent we get

$$r_1 = R_1 + \frac{1}{2R_1} (X_0 - X_1)^2 + \frac{1}{2R_1} (Y_0 - Y_1)^2 \quad (2.1.2)$$

$$r_2 = R_2 + \frac{1}{2R_2} (X_0 - X_2)^2 + \frac{1}{2R_2} (Y_0 - Y_2)^2 \quad (2.1.3)$$

Using planar polar coordinates in each of the three planes we have

$$X_0 = \rho a \cos \theta; \quad X_1 = H \cos \alpha; \quad X_2 = \sigma \cos \phi$$

$$Y_0 = \rho a \sin \theta; \quad Y_1 = H \sin \alpha; \quad Y_2 = \sigma \sin \phi \quad (2.1.4)$$

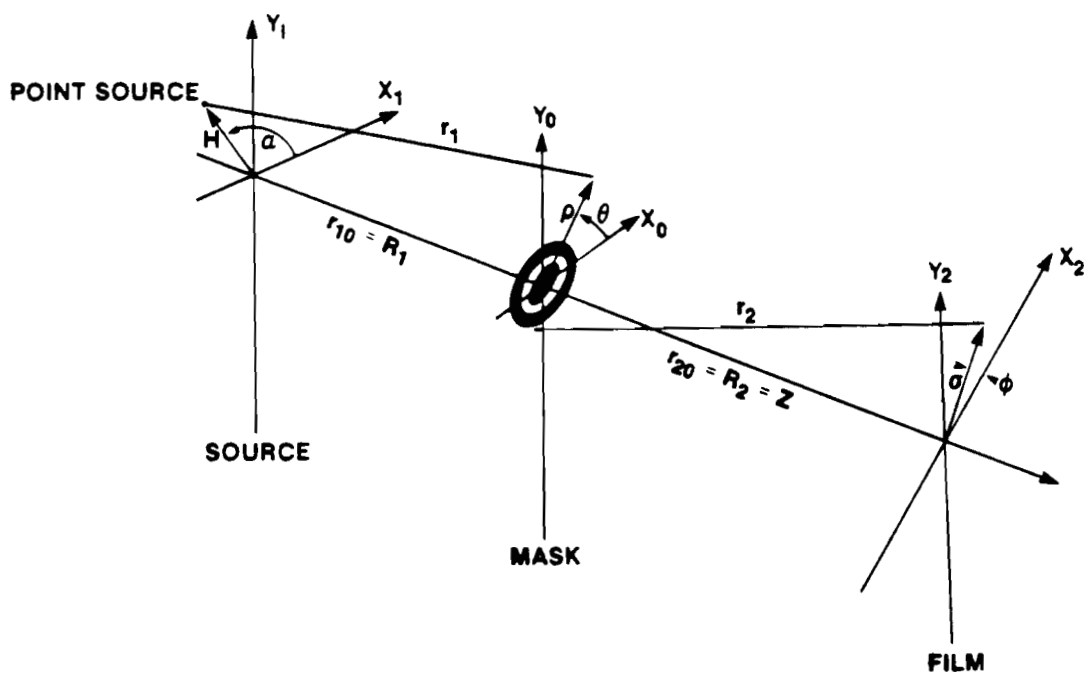


Fig. 2.1.1  
Diffraction of a spherical wave through a zone plate.

$$dX_0 dY_0 = a^2 \rho d\rho d\theta; \quad u = \frac{a^2}{2\lambda} \left( \frac{1}{R_1} + \frac{1}{R_2} \right),$$

where  $(\rho a, \theta)$ ,  $(H, \alpha)$  and  $(\sigma, \phi)$  are the coordinates in the mask, source and film planes respectively;  $a$  is the aperture radius and  $\rho$  is the fractional radius. Using (2.1.2), (2.1.3), (2.1.4) in (2.1.1) we get:

$$G(\sigma, \phi) = \frac{iAa^2}{\lambda R_1 R_2} e^{iK(R_1+R_2)} e^{iKH^2/2R_1} e^{iK\sigma^2/2R_2} \quad (2.1.5)$$

$$\int_0^{2\pi} \int_0^1 A(\rho) e^{2\pi i u \rho^2} e^{(-iK\sigma\rho/R_2)\cos(\theta-\phi) - (iKH\rho/R_1)\cos(\theta-\alpha)} \rho d\theta d\rho.$$

Consider the terms that involve angles:

$$\begin{aligned} -K\rho a \left\{ \frac{\sigma}{R_2} \cos(\theta-\phi) + \frac{H}{R_1} \cos(\theta-\alpha) \right\} &= \quad (2.1.6) \\ &= -K\rho a \left\{ \cos \theta \left[ \frac{H \cos \alpha}{R_1} + \frac{\sigma \cos \phi}{R_2} \right] + \sin \theta \left[ \frac{H \sin \alpha}{R_1} + \frac{\sigma \sin \phi}{R_2} \right] \right\}, \\ &= -K\rho a v \cos(\theta-\chi), \end{aligned}$$

where

$$\begin{aligned} \cos \chi &= \left[ \frac{H \cos \alpha}{R_1} + \frac{\sigma \cos \phi}{R_2} \right] / v, \quad (2.1.7) \\ \sin \chi &= \left[ \frac{H \sin \alpha}{R_1} + \frac{\sigma \sin \phi}{R_2} \right] / v, \\ v^2 &= (H/R_1)^2 + (\sigma/R_2)^2 + 2H\sigma/R_1 R_2 \cos(\phi-\alpha). \end{aligned}$$

Let  $H/R_1$  be the object field angle and  $\sigma/R_2$  be the image field angle.

Let us change variables:  $\rho^2 = t$ ;  $\rho d\rho = \frac{1}{2} dt$ .

Until now the discussion was general and could be applied to gratings as well as to zone plates. We now limit the discussion to rotationally symmetric apertures, i.e.  $A(\rho)$  is rotationally symmetric.

Then  $A'(\rho^2) = A(t)$ . Using an identity for Bessel functions [2.12]

$$\frac{1}{2\pi} \int_0^{2\pi} e^{-iK\rho a v \cos(\theta-\chi)} d\theta = J_0(K\rho a v), \text{ and considering only the inte-}$$

gral in Eq. (2.1.5) we get:

$$G'(\sigma, \phi) = \int_0^1 A(t) e^{2\pi i t u} J_0(v\sqrt{t}) dt \quad . \quad (2.1.8)$$

The prime denotes that all the constants were omitted from the formula. Eq. (2.1.8) is the most general expression for the field diffracted from an axially symmetric circular aperture on which a spherical wave of radius  $R_1$  is incident.

Consider the intensity on axis when a point source situated on axis is illuminating a zone plate. In this case  $H=\sigma=0$ ; therefore  $v=0$  and  $J_0(K\rho a v)=1$  and we get from (2.1.8)

$$G'(u) = \int_0^1 A(t) e^{2\pi i u t} dt \quad . \quad (2.1.9)$$

This is exactly the Fourier transform of the aperture written in the  $t$ -domain rather than in the  $\rho$ -domain.

We thus see that the on axis intensity distribution of rotationally

symmetric, two-dimensional, apertures is completely analogous to the far field intensity distribution diffracted by a one-dimensional aperture. Therefore, any result derived in one domain can be immediately transferred to the analogous domain.

We will consider a special class of rotationally symmetric apertures: Fresnel zone plates and a few of their derivatives. The term Fresnel zone plate refers only to a special class of apertures as shown in Fig. 2.1.3. Other general apertures which have some similarities to Fresnel zone plates will simply be called zone plates.

Since we deal with apertures derived from the Fresnel zone plate, let us clarify the notation by first considering Fig. 2.1.2. A cosinusoidal zone plate may be produced by recording the interference from two coherent sources on axis. Let  $A_1, A_2; \phi_1, \phi_2; R_1, R_2$  be the amplitudes, phases, and distances of sources 1 and 2, respectively, from the screen, and assume that  $A_1/R_1 = A_2/R_2 = A$ . Let us use the following definitions:  $u = \left[ \frac{1}{R_{10}} - \frac{1}{R_{20}} \right] \frac{\pi}{\lambda}$ ;  $\Delta\phi = R_{10} - R_{20} + \phi_1 - \phi_2$ ;  $x =$  distance on the screen. From Fig. 2.1.1 and 2.1.2 we then have

$$I = 2A^2 \left[ 1 + \cos \left( \frac{x^2 u}{4} + \Delta\phi \right) \right] \quad (2.1.10)$$

In Fig. 2.1.3a Eq. (2.1.10) is plotted for four different source phases. The corresponding Fresnel zone plates that are derived from them are also shown. All plots are in the  $\theta = \frac{ux}{4}$  coordinate. Zone plates of type (c) and (d) are most commonly employed. (c) is called a positive

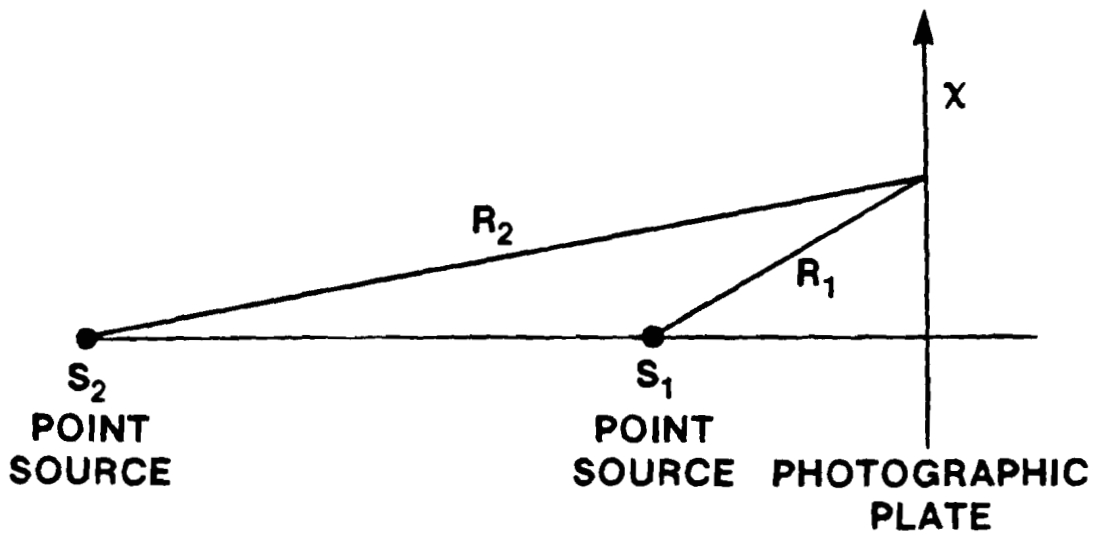


**Fig. 2.1.2**  
**Formation of a zone plate by interference of two spherical waves.**

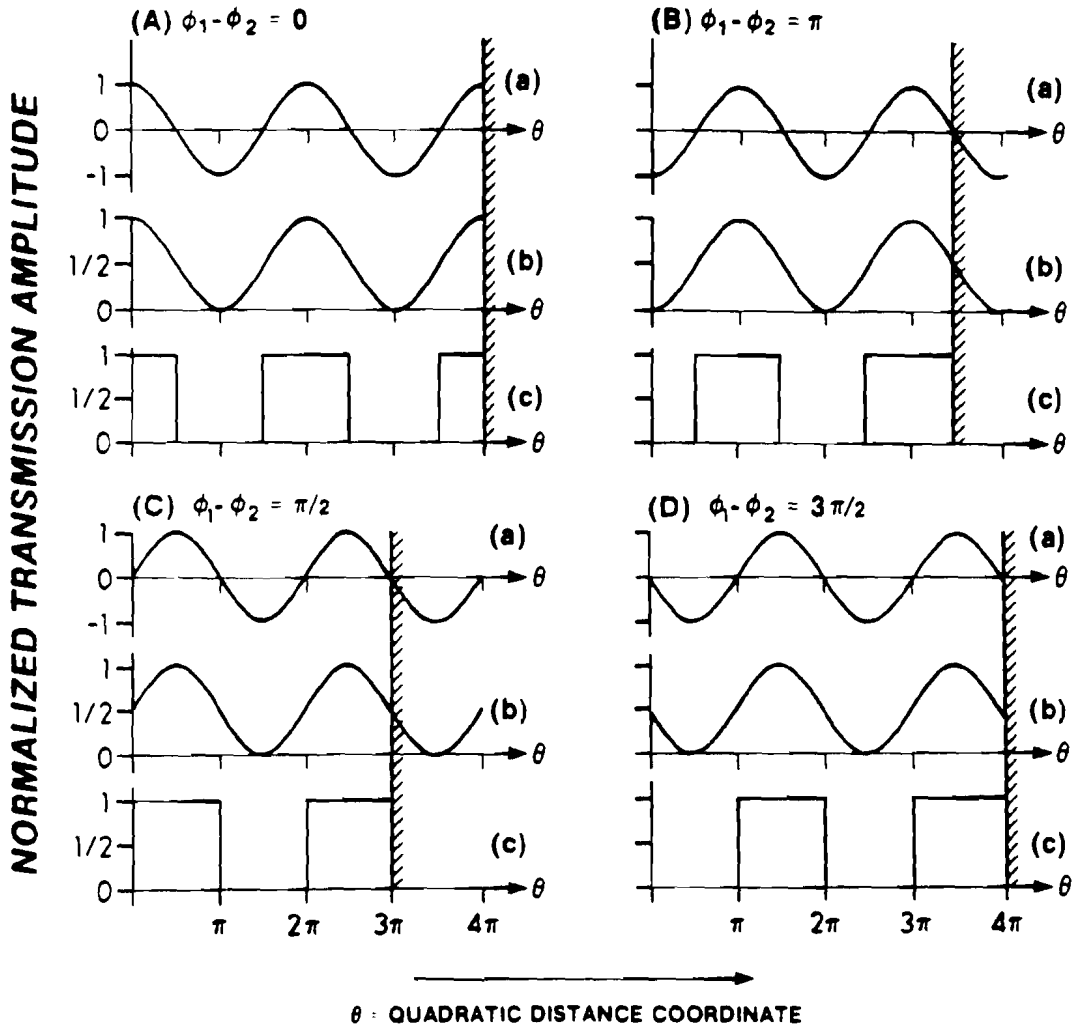


Fig. 2.1.3a  
 The cosinusoidal zone plates produced by interference of two spherical waves and the corresponding Fresnel zone plates drawn in  $\theta$  domain. Cases A, B, C, D are phase differences  $\phi_1 - \phi_2 = 0, \pi, \pi/2, 3\pi/2$  respectively. For each case (a) represents the cos part of eq. (2.1.10), (b) the intensity in eq. (2.1.10) and (c) the corresponding Fresnel zone plate. Case C is the positive Fresnel zone plate. Case D is the negative Fresnel zone plate.

zone plate and (d) is called a negative zone plate. (They differ by a phase of  $\pi$ .) In Fig. 2.1.3 b positive zone plates in real space are shown. From Fig. 2.1.3 a we see that positive zone plates always have an odd number of zones (transparent and opaque). The number of open zones exceeds by one the number of opaque zones. The negative zone plate has an even number of zones.

In Table 2.1.1 (1) we list the location of the zone edges (in the  $\theta$ -coordinate for the four cases in Fig. 2.1.3 a. In (2) we list the boundaries of the open zone in each case. Finally we generalize in (5) these expressions in order to obtain an expression for an arbitrary zone plate width and shape. From Table 2.1.1 it is possible to write an expression from which all the four cases in Table 2.1.1 can be derived. The range of  $\theta$  that belongs to the  $j^{\text{th}}$  open zone denoted by  $\theta_j$  is:

$$(2j - \frac{1}{2})\pi + \Delta\phi \leq \theta_j \leq (2j + \frac{1}{2})\pi + \Delta\phi \quad (2.1.11)$$

where  $\Delta\phi = \phi_1 - \phi_2 = (0, \pi, \pi/2, 3\pi/2)$  according to Fig. 2.1.3 a.

In a computer calculation of the diffracted intensity distributions from various zone plates we find it convenient to define RPEVEN, RPODD; RNEVEN, RNODD to be the radii of an even numbered or an odd numbered zone edge respectively in a positive or negative zone plate respectively, and EPS1 and EPS2 to be the fractional width of the zone plates as in Fig. 2.1.4 b. Q is the zone plate constant (i.e.  $Q = 1/\sqrt{NZONE}$ ), and NZONE is the total number of zones. Using these definitions and Table 2.1.1 we can write the following results:

1. Positive zone plate (NZONE = odd number; open center)

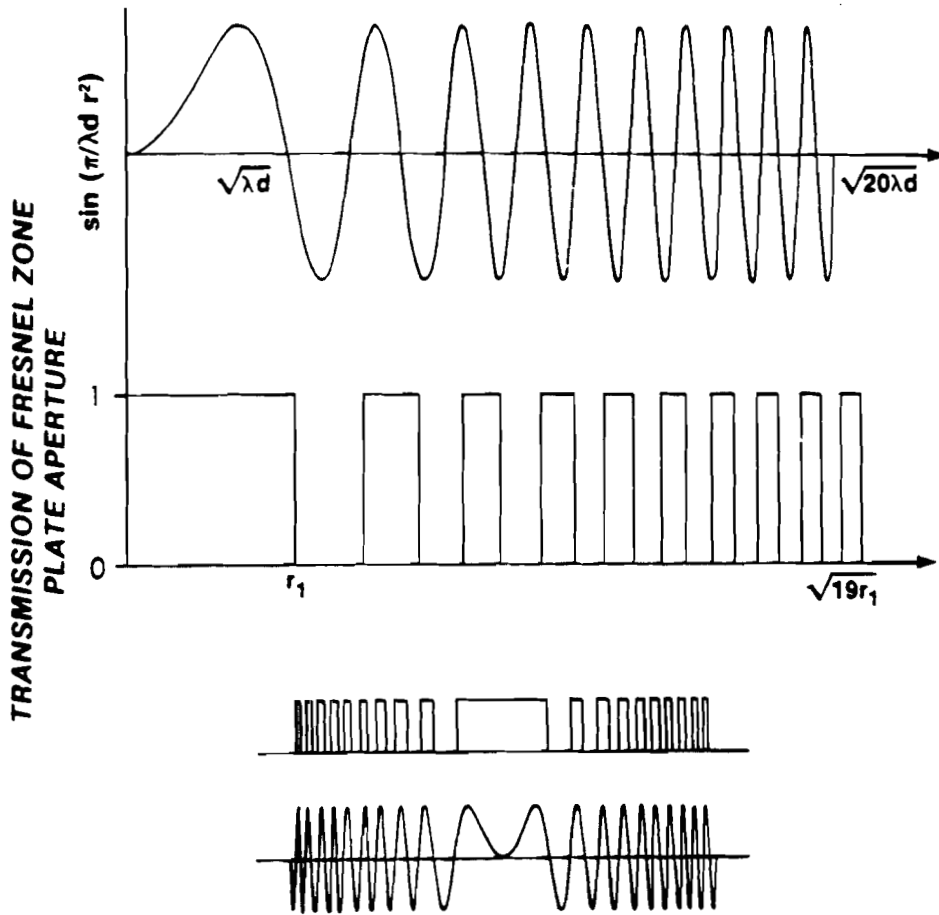


Fig. 2.1.3b  
Cosinusoidal zone plates and Fresnel zone plates drawn in real space coordinate.

Table 2.1.1: Notation for Fresnel Zone Plates

Number	Zone Plate Edge Locations	A	B	C	D
		$\phi_1 - \phi_2 = 0$	$\phi_1 - \phi_2 = \pi$	$\phi_1 - \phi_2 = \frac{\pi}{2}$	$\phi_1 - \phi_2 = \frac{3\pi}{2}$
	$\theta_0$	0	$\pi/2$	0	$\pi$
	$\theta_1$	$\pi/2$	$3\pi/2$	$\pi$	$2\pi$
(1)	$\theta_2$	$3\pi/2$	$5\pi/2$	$2\pi$	$3\pi$
	$\theta_3$	$5\pi/2$	$7\pi/2$	$3\pi$	$4\pi$
	$\theta_4$	$7\pi/2$		$4\pi$	
	<u>Open Zone Boundaries</u>				
	$j = 0$	$0 \rightarrow \pi/2$	$\pi/2 \rightarrow 3\pi/2$	$0 \rightarrow \pi$	$\pi \rightarrow 2\pi$
(2)	$j = 1$	$3\pi/2 \rightarrow 5\pi/2$	$5\pi/2 \rightarrow 7\pi/2$	$2\pi \rightarrow 3\pi$	$3\pi \rightarrow 4\pi$
	$j = 2$	$7\pi/2 \rightarrow 8\pi/2$			
(3)	<u>General Form for Zone Boundaries</u>	$(2j - \frac{1}{2})\pi \rightarrow (2j + \frac{1}{2})\pi$	$(2j + \frac{1}{2})\pi \rightarrow (2j + \frac{3}{2})\pi$	$2j\pi \rightarrow (2j + 1)\pi$	$(2j + 1)\pi \rightarrow 2(j + 1)\pi$

Table 2.1.1: Continued

Number	Comments	Zone Plate Type (according to Fig. 2.1.3a)			
		A	B	C	D
(4)	<u>Equivalent Form</u>	- - -	- - -	$\frac{4j\pi}{2} + \frac{2(2j+1)\pi}{2}$	$\frac{2(2j+1)\pi}{2} + \frac{4(j+1)\pi}{2}$
(5)	<u>Final Form</u>	- - -	- - -	$\left(\frac{4j+1}{2} - \frac{1}{2}\right)\pi + \left(\frac{4j+1}{2} + \frac{1}{2}\right)\pi$	$\left(\frac{4j+3}{2} - \frac{1}{2}\right)\pi + \left(\frac{4j+3}{2} + \frac{1}{2}\right)\pi$
(6)	<u>Location of Zone Centers</u>	- - -	- - -	$\frac{(4j+1)}{2}\pi$	$\frac{(4j+3)}{2}\pi$

$$RPEVEN = [(4M+1)/2 - EPS1]^{\frac{1}{2}}Q; \quad RPODD = [(4M+1)/2 + EPS2]^{\frac{1}{2}}Q \quad (2.1.12)$$

where  $M = 0, \dots, (NZONE-1)/2$

2. Negative zone plate (NZONE = even number; opaque center)

$$RNODD = [(4M+3)/2 - EPS1]^{\frac{1}{2}}Q; \quad RNEVEN = [(4M+3)/2 + EPS2]^{\frac{1}{2}}Q \quad (2.1.13)$$

where  $EPS1, EPS2 \leq 0.5$  but for a Fresnel zone plate  $EPS1 = EPS2 = 0.5$ .

As an example we calculate (2.1.9) for a positive zone plate. Since the equation is in the form of a Fourier transform, we may consider the analogous case of the Fraunhofer diffraction pattern of a grating. We derive it explicitly because of misleading results in the literature 2.1.4, [2.1.5], [2.1.6] and [2.1.7]. Denote by  $N$  the total number of zones (both clear and opaque) From (2.1.9) we have:

$$G'(u) = \int_{-\infty}^{\infty} \sum_n \delta(t - 2nq - \frac{q}{2}) * \text{Rect}[t;q] e^{2\pi i u t} dt \quad (2.1.14)$$

Using the convolution theorem and the fact that

$$\int_{-\infty}^{\infty} \text{Rect}[t;q] e^{2\pi i u t} dt = \frac{\sin \pi u q}{\pi u}$$

we have:

$$G'(u) = e^{2\pi i(uq/2)} \sum_{n=0}^{(N-1)/2} e^{2\pi i 2nqu} \frac{\sin \pi uq}{\pi u}, \quad (2.1.15a)$$

or

$$G'(u) = e^{\pi i Nqu} \frac{\sin[\pi uq(N+1)]}{\sin(2\pi qu)} \frac{\sin[\pi uq]}{\pi u}, \quad (2.1.15b)$$

From (2.1.15 b) and (2.1.5) we get for the amplitude (neglecting the phase factors):

$$G''(u) = \frac{1}{2\lambda R_1 R_2} \frac{\pi A a^2}{2} \frac{\sin[\pi qu(N+1)]}{\cos(\pi qu)} \frac{1}{\pi u} \quad (2.1.15c)$$

Assume  $R_1 \rightarrow \infty$  (collimated light);  $A/R_1 \rightarrow E = \text{constant}$ . Substituting for  $u$  from (2.1.4) into (2.1.15 c) we have the remarkable result:

$$G''(u) = \frac{E}{2} \frac{\sin[\pi qu(N+1)]}{\cos(\pi qu)} \quad (2.1.16)$$

From 2.1.16 it is obvious that all the foci have the same peak on-axis intensity. The locations of the foci are found by taking the limit of (2.1.16) as  $\cos(\pi qu) \rightarrow 0$ , or  $u \rightarrow (2\ell+1)\frac{1}{2q}$  and by using (2.1.4) for  $u$  the locations will be found later. Substituting for  $u$  we get the limit:

$$\lim_{u \rightarrow (2\ell+1)1/2q} \frac{\sin[\pi qu(N+1)]}{\cos(\pi qu)} = \frac{(N+1)}{2} (-1)^{\ell-1} \quad (2.1.17)$$

From (2.1.5) and (2.1.7) we write the total phase function using  $R_1 \rightarrow \infty$  and  $\sigma = 0$  as:  $\phi = \frac{\pi}{2} + KR_{20} - \frac{\pi(N+1)}{2} - \pi l$ . Hence successive odd

order foci have successive phase changes of  $\pi$ . (Not including the phase due to distance  $KR_{20}$ .) From  $\pi qu = (2l+1)\frac{\pi}{2}$ ,  $u = \frac{a^2}{2\lambda R_2}$  and  $q = \frac{1}{N}$  we

get, denoting the order number by  $p$ , the locations of the foci:

$$R_2 = \frac{a^2}{N\lambda} \frac{1}{p} = \frac{F}{p} \quad (2.1.18)$$

Let us explore more specific examples of the analogy between zone plates and gratings.

### 2.1.1 Spread of the principal orders.

Eq. (2.1.15 b) is the formula for the on-axis intensity of a zone plate but it is also the expression of the intensity in the Fraunhofer plane of a diffraction grating. The only difference is the coordinate  $u$ . In the zone plate case,  $u = a^2/2\lambda R_2$  while in the grating case,  $u = (d\lambda/2\lambda R_2)\frac{1}{q}$  where  $\lambda$  is the distance on a transverse plane;  $d$  is the slit size width;  $q = \frac{1}{N}$ . For a given  $N$  the spread of the principal orders is constant in the  $u$  domain. This is true in the grating case and also in the zone plate case in  $u$  domain. However it is not true for zone plates in real domain where, as we go to higher orders, the spread on axis gets smaller. From (2.1.15 b), using the two definitions of  $u$ , we get the spread of principal orders (using small angle approximations).

For ruled gratings:  $\Delta X = \frac{\lambda Z}{Nd}$

For zone plates:  $\Delta R_2 = \frac{\lambda}{\frac{(N+1)}{2}} \frac{R_2^2}{qa^2}$

### 2.1.2 Chromatic Resolving Power.

Both gratings and zone plates can be used as spectrometers. While the dispersion in gratings occurs in transverse plane, a zone plate can be used as an axial spectrometer. In both cases the important quantity is the chromatic resolving power. From Ref. [2.1.1] p.106 (let  $M$  be the order number) we have for gratings that

$$\frac{\Delta \lambda}{\lambda} = \frac{1}{NM} \quad (2.1.19a)$$

The same calculation for a zone plate gives

$$\frac{\Delta \lambda}{\lambda} = \frac{1}{\frac{(N+2)}{2}(2l+1)} \quad (2.1.19b)$$

which is analogous to (2.1.19a).

### 2.1.3 Dispersion.

In a grating the dispersion along a one-dimensional coordinate  $X$  is given in Ref. [2.1.1]. p.106:

$$\Delta X = \frac{Z \Delta \lambda}{Nd}$$

In a zone plate the dispersion along the optical axis is:

$$\Delta R_2 = R_2^2 / qa^2 \cdot \Delta \lambda / \frac{(N+1)}{2}$$

or 
$$\frac{\Delta R_2}{R_2} = \frac{\Delta \lambda}{\lambda}$$

Hence, if we want to use the zone plate in the imaging mode only,

quasimonochromatic radiation must be used.

#### 2.1.4 Illumination with a Finite Source.

Assume at first that the source is planar and perpendicular to the optical axis. Spherical waves from different points are incident on a grating at different angles and give rise to grating patterns slightly displaced with respect to each other. Note that this is true either in the Fraunhofer plane or at the image plane of the point source when a lens is used. Thus if the source is incoherent then the diffraction pattern will be a convolution of the source with the diffraction pattern produced by collimated light. The direct analog in a zone plate will be a longitudinal line source. The convolution is exact in  $1/z$  coordinates but in  $z$  coordinates the axial spread of higher orders will shrink. A transverse source, however, will be imaged to a transverse source as with a lens.

#### 2.1.5 The Effects of Changing the Zone Shape or the Slit Shape.

For this discussion we will work with the analogy between amplitude gratings and zone plates. In Fig. 2.1.4 a few examples of different zone plates are shown. We can describe the on-axis intensity distributions using the same procedures as before. Let  $B_g(t)$  be the individual amplitude slit shape (or the zone shape in the  $r^2$  domain). The aperture function of the grating (or the zone plate) can then be written:

$$A(t) = \sum_n \delta(t - 2nq - \frac{q}{2}) \cdot \text{Rect} \left[ t - \frac{qN}{2}; \frac{Nq}{2} \right] * B_g(t) \quad . \quad (2.1.20)$$

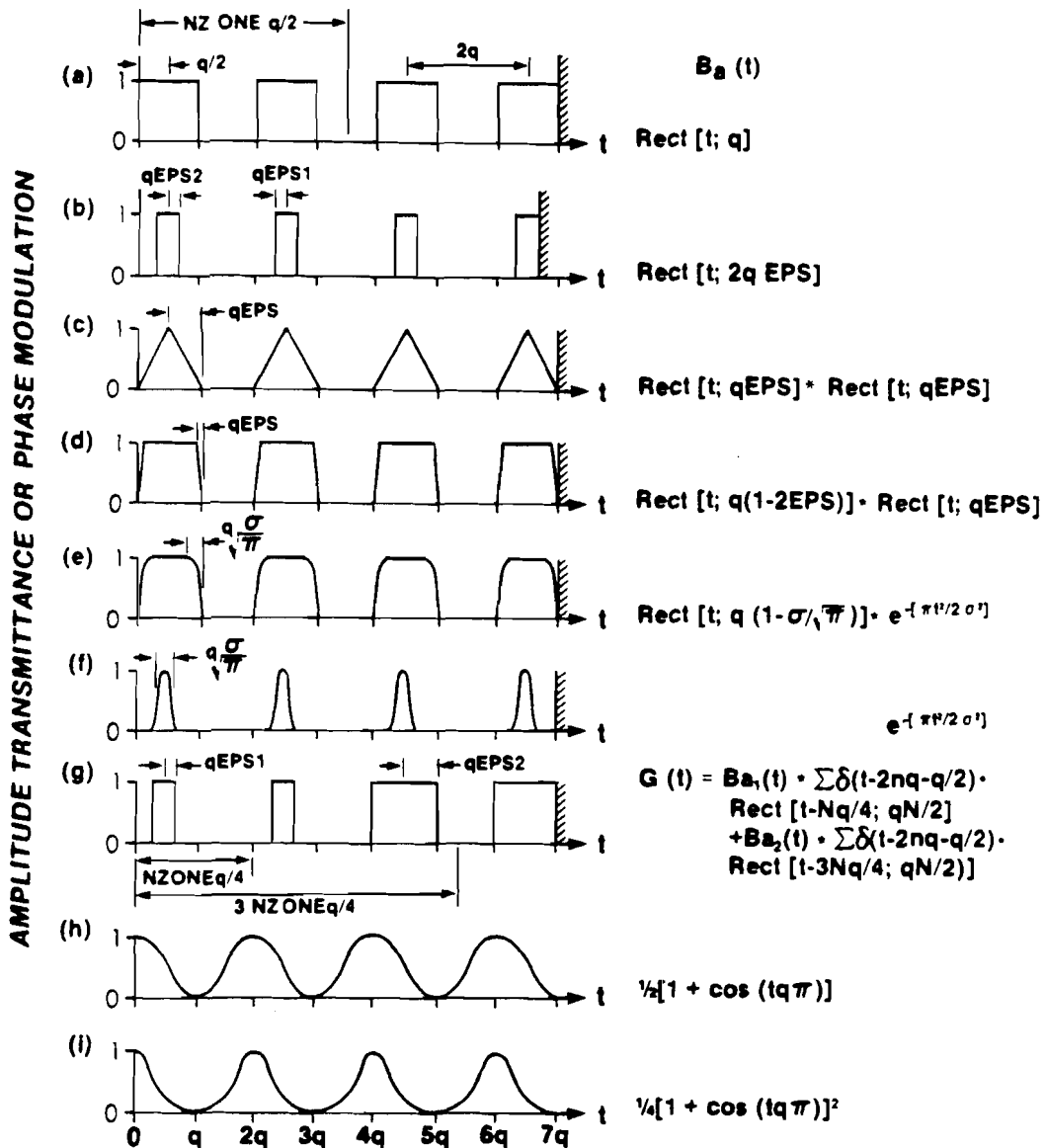


Fig. 2.1.4

Amplitude transmission or phase modulation of zone plates ( $t$  = distance square coordinate), or of amplitude or phase gratings ( $t$  = real distance coordinate). (a) Fresnel zone plate (positive), (b) zone plate with narrow zones, (c) triangular zones, (d) zone plate with slanted edges, (e) edges smoothed with a Gaussian function, (f) narrow Gaussian zones, (g) zone plate with two different zone widths, (h) cosinusoidal zone plate, (i) cosinusoidal zone plate recorded with  $\gamma = 2$ .

Neglecting constants and phases, the diffraction pattern is, therefore:

$$G(u) = \frac{\sin[\pi qu(N+1)]}{\sin[\pi qu]} \cdot \tilde{B}_a(u) \quad (2.1.21)$$

The  $\tilde{B}_a(u)$  and the corresponding  $G(u)$  are calculated in Table 2.1.2. There are two methods of normalization. In the first we normalize the intensity of the diffraction pattern with respect to the zero order. This is a useful procedure when the energy diffracted in the zero order is measurable as in the case of amplitude zone plates illuminated with collimated light. However the zero order can be eliminated in phase gratings, and in the case of zone plates illuminated with a collimated beam, the energy in the zero order is not focussable. In these cases we normalize the diffracted intensity with respect to the first order. Examples of a few normalized expressions are given in Table 2.1.3.

#### 2.1.6 Conclusions from the Calculations of the Diffraction Patterns for Gratings and Zone Plates (Fig. 2.1.4 and Table 2.1.2).

1. The on-axis intensity in higher orders in zone plates, depends strongly upon the shape of the individual zones.
2. It is not possible to eliminate the zero order with only an amplitude modulation in the grating. The presence of the zero order causes background problems both when imaging with zone plates and in reconstruction in pseudoholography.
3. If the zone plates have very sharp edges, as in Fig. 2.1.4.a, the peak on-axis intensity will stay the same at all odd orders. If the zones are made narrower as in Fig. 2.1.4 b even numbered foci

Table 2.1.2: Fraunhofer Diffraction Patterns of Gratings and On-Axis Amplitudes of Zone Plates  
( Neglecting the phase factors )

# from Fig. 2.1.4	$\tilde{B}_a(u)$	$G(u)$
4a	$\frac{\sin(\pi u)}{\pi u}$	$\frac{iE \sin[\pi u q(N+1)]}{\sin[\pi u q]} \cdot \sin(\pi u q)$
4b	$\frac{\sin(\pi u q 2EPS)}{\pi u}$	$\frac{iE \sin[\pi u q(N+1)]}{\sin[\pi u q 2]} \cdot \sin(\pi u q 2EPS)$
4c	$\frac{\sin^2(\pi u qEPS)}{(\pi u)^2}$	$\frac{iE \sin[\pi u q(N+1)]}{\sin[\pi u q 2]} \cdot \frac{\sin^2(\pi u qEPS)}{\pi u}$
4d	$\frac{\sin[\pi u q(\frac{1-2EPS}{2})]}{\pi u} \cdot \frac{\sin(\pi u qEPS)}{\pi u}$	$\frac{iE \sin[\pi u q(N+1)]}{\sin[\pi u q 2]} \cdot \sin[\pi u q(\frac{1-2EPS}{2})] \cdot \frac{\sin(\pi u qEPS)}{\pi u}$
4e	$\frac{\sin[\pi u q(1 - \frac{\sigma}{\sqrt{\pi}})] (\sqrt{2} \sigma) \exp[-2\pi\sigma^2 u^2]}{\pi u}$	$\frac{iE \sin[\pi u q(N+1)]}{\sin[\pi u q 2]} \cdot \sin[\pi u q(1 - \frac{\sigma}{\sqrt{\pi}})] (\sqrt{2} \sigma) \exp[-2\pi\sigma^2 u^2]$
4f	$\sqrt{2} \sigma \exp[-2\pi\sigma^2 u^2]$	$\frac{iE \sin[\pi u q(N+1)]}{\sin[\pi u q 2]} \cdot u\sqrt{2} \sigma \exp[-2\pi\sigma^2 u^2]$
4g		$\frac{iE \sin[\pi u q(\frac{N+1}{2})]}{\sin[\pi u q 2]} \cdot u e^{i\phi} [\tilde{B}_{a_1}(u) + \tilde{B}_{a_2}(u) e^{i(\phi_2 - \phi_1)}]$
4h		$iE u(\delta(u) + \frac{1}{2}\delta(u - \frac{q}{2}) + \frac{1}{2}\delta(u + \frac{q}{2}))$
4i		$iE u(\frac{3}{2}\delta(u) + \delta(u - \frac{q}{2}) + \frac{1}{4}\delta(u - q) + \frac{1}{4}\delta(u + q))$

Table 2.1.3: Normalization for Zone Plates and Gratings

# from Fig. 2.1.4	Normalization (Grating Case) $\frac{G(u)}{G(0)}$	Normalization (Zone Plates Case) $\frac{G(u)}{G(1/2q)}$
4a	$\frac{2}{(N+1)} \frac{\sin[\pi u q (N+1)]}{\sin[\pi u q 2]} \frac{\sin(\pi u q)}{(\pi u q)}$	$\frac{2}{(N+1)} \frac{\sin[\pi u q (N+1)]}{\sin[\pi u q 2]} \cdot \sin(\pi u q)$
4b	$\frac{2}{(N+1)} \frac{\sin[\pi u q (N+1)]}{\sin[\pi u q 2]} \frac{\sin[\pi u q 2 \text{EPS}]}{(\pi u q 2 \text{EPS})}$	$\frac{2}{(N+1)} \frac{\sin[\pi u q (N+1)]}{\sin[\pi u q 2]} \cdot \frac{\sin[\pi u q 2 \text{EPS}]}{\sin(\pi \text{EPS})}$
4c	$\frac{2}{(N+1)} \frac{\sin[\pi u q (N+1)]}{\sin[\pi u q 2]} \frac{\sin^2[\pi u q \text{EPS}]}{(\pi u q \text{EPS})^2}$	$\frac{2}{(N+1)} \frac{\sin[\pi u q (N+1)]}{\sin[\pi u q 2]} \cdot \frac{\sin^2[\pi u q \text{EPS}]}{\sin^2(\pi \text{EPS})} \cdot \frac{1}{(q u 2)}$
4d	$\frac{2}{(N+1)} \frac{\sin[\pi u q (N+1)]}{\sin[\pi u q 2]} \frac{\sin[\pi u q (\frac{1 - \text{EPS}}{2})]}{[\pi u q (\frac{1 - \text{EPS}}{2})]}$	$\frac{2}{(N+1)} \frac{\sin[\pi u q (N+1)]}{\sin[\pi u q 2]} \cdot \frac{\sin[\pi u q (\frac{1 - \text{EPS}}{2})]}{\sin[\pi (\frac{1 - \text{EPS}}{4})]}$
4e	$\frac{2}{(N+1)} \frac{\sin[\pi u q (N+1)]}{\sin[\pi u q 2]} \frac{\sin[\pi u q (1 - \frac{\sigma}{\sqrt{\pi}})]}{[\pi u q (1 - \frac{\sigma}{\sqrt{\pi}})]}$	$\frac{2}{(N+1)} \frac{\sin[\pi u q (N+1)]}{\sin[\pi u q 2]} \cdot \frac{\sin[\pi u q (1 - \frac{\sigma}{\sqrt{\pi}})]}{\sin[\frac{\pi}{2} (1 - \frac{\sigma}{\sqrt{\pi}})]}$
4f	$\frac{2}{(N+1)} \frac{\sin[\pi u q (N+1)]}{\sin[\pi u q 2]} e^{-[2\pi\sigma^2 u^2]}$	$\frac{2}{(N+1)} \frac{\sin[\pi u q (N+1)]}{\sin[\pi u q 2]} \left(\frac{\sigma}{q}\right) e^{-[2\pi\sigma^2 u^2 - \frac{\pi\sigma^2}{2q^2}]}$

appear. Some high even and odd orders may also have a peak intensity corresponding to the ideal case  $EPS=0.5$  depending on the number EPS (see Table 2.1.2.4b).

4. Smoothing of the edges tends to decrease the efficiency at higher orders. For a triangular zone shape (Fig. 2.1.4.c, 2.1.4.d) the decrease is the worst of the examples picked. In case of a Gaussian shape, the decrease is less severe (Fig. 2.1.4.e, 2.1.4.f). There may even be an increase in on-axis intensity at higher orders as may be seen by substituting for  $\gamma$  in Table 2.1.2.4f the value  $1/N$  where  $N$  is the number of zones.

5. Processing the original recording with  $\gamma \neq 1$  changes the apparent shape of the zones. Therefore, the efficiency at higher orders depends very much on the type of processing. Processing may also cause artifacts in pseudoholography as will be discussed later on.

6. Because of the finite dynamic range of the recording medium it is preferable to use zone plates with narrow zones, (as will be seen later on) therefore a zone plate as in Fig. 2.1.4.g seems attractive. The inner zones are much narrower compared to their usual width. This, in addition, will tend to increase the light scattered into higher orders.

7. If the amplitude modulation in the grating is an exact  $\cos^2$  function  $A \cos^2 = A/2(1 + \cos 2\theta)$  then only 0,  $\pm 1$  orders appear and in the case of zone plates only one real focus exists.

### 2.1.7 Phase Gratings and Zone Plates.

In this case there are two modes of operation: (1) transmission, where changes in index of refraction cause diffraction, and (2) reflection, where the relief structure on the surface causes the diffraction. The sinusoidal phase grating was analyzed by Goodman [2.1.2].

In Fig. 2.1.4 a few other examples are listed. Only the sinusoidal example has a simple closed form solution, the others are extremely involved. Kirtz [2.1.8] has calculated a general expression for the example 2.1.4 d (where the vertical axis is now phase). His treatment includes absorption effects as well. He mentioned only zone plates but all his results apply equally well to gratings. Also, he assumes working only in transmission (the analog being transmission gratings).

However, in Ref. [2.1.9] and [2.1.10] the efficiency of reflection gratings is considered with different groove shapes. These results can be applied directly to zone plates working in the reflection mode.

Bleaching of pseudoholograms may be a useful technique to enhance higher order reconstruction. Also reconstruction in reflection should be investigated both with and without aluminum coating on the processed pseudohologram. Coating with Ag or Al will enhance the surface structure while reconstruction without a coating will take advantage of volume effects as well. Using zone plates in reflection introduces new problems such as polarization effects. These were not treated before because the usual use of zone plates was in the transmission mode on axis. This mode of operation may provide an easier way to blaze the pseudohologram to achieve high efficiency at high orders.

The main advantage of phase gratings (or zone plates) over the amplitude counterpart is the possibility of conveniently eliminating the zero order and hence increasing the signal to noise ratio, both in imaging applications as well as with the reconstruction of pseudoholograms. As an example, consider a phase grating or zone plate of the type shown in Fig. 2.1.4 a. Calculating the  $\tilde{B}_p(u)$  which corresponds to  $\tilde{B}_a(u)$  in Eq. (2.1.20) and Table 2.1.1, we get:

$$\tilde{B}_p(u) = \int_{-q}^0 e^{i\phi} dt + \int_0^q dt = q(e^{i\phi} + 1)$$

This will determine the efficiencies at all the orders as we have seen in section 2.1.4. The condition for  $\tilde{B}_p(0)=0$  is that  $\phi=\pi$ . Fig. 2.1.4 a shows this blazed phase grating (when  $\phi = \pi$ ) in which the zero order is eliminated and higher orders are more intense on-axis.

In Fig. 2.1.5 we see the condition for blazing a transmission zone plate for a specific order in analogy with blazed reflecting gratings. In practice we may control the phase modulation by the exposure in the case of reconstructing a pseudohologram. Also, by controlling the magnification of the pseudohologram we may find the right focal length that exactly matches the given modulation to obtain blazing. This technique is completely analogous to gratings and has been used so far only in the far infrared regions [2.1.11 a]. A group at Lawrence Livermore Laboratory has recently announced [2.1.11 b] its intention to blaze zone plates for the x-ray region for use in the imaging mode.

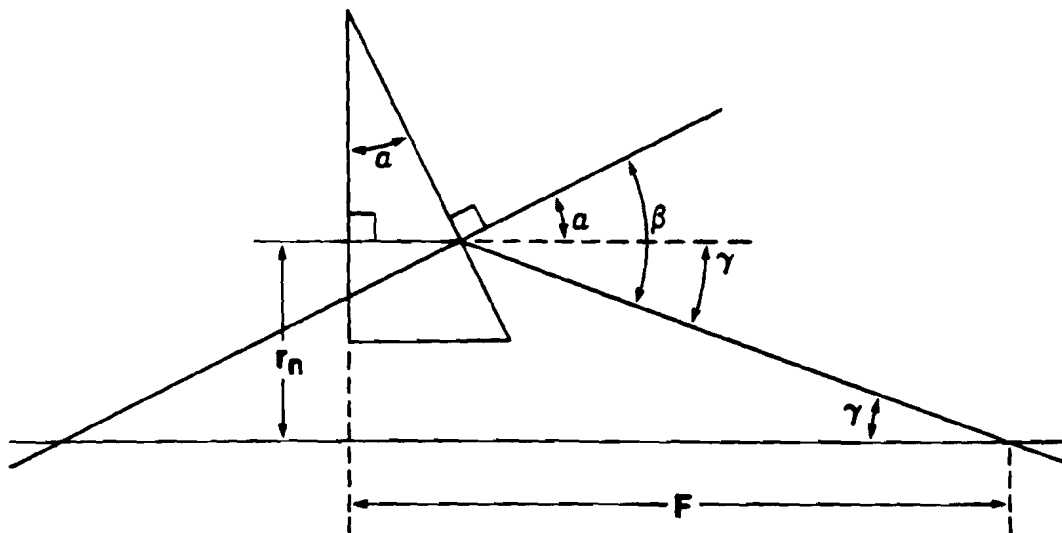


Fig. 2.1.5

Blazing of the zone plate occurs when both the diffracted and the refracted beams have the same direction, in complete analogy with diffraction gratings.  $r_n$  is the  $n$ th radius of the zone plate.  $F$  is the focal length where the zone plate is blazed. If  $n_2$  is the refractive index of the material of which the zone plate is made,  $n_2 \sin \alpha = \sin \beta$ .

### 2.1.8 Fluxes at Higher Orders.

For the example in Fig. 2.1.4.a we have seen that the peak on-axis intensity is the same at all the odd numbered foci. At high orders we approach closer to the zone plate and have a larger cone angle of illumination. This means that incident collimated light will be focussed to a smaller Airy disc. If  $\Omega_1$  is the cone angle at the primary focus,  $p\Omega_1$  is the cone angle at focus number  $p$ . The area of the Airy disc is then  $\frac{1}{p^2}$  where  $S_1$  is the area of the Airy disc at the primary focus. Since the peak intensities are equal but the areas are related as  $1:p^2$ , the number of scattered photons must also be related as  $1:p^2$ .

### 2.1.9 Scattering and Noise in Gratings and Zone Plates.

We may distinguish between two kinds of scattering which lead to speckle patterns in the reconstruction of a pseudohologram and to background noise in case of imaging an incoherent source. In the case of a pseudohologram which is recorded on film, the film grains will cause a speckle pattern when we illuminate with coherent light exactly in the same way as a ground glass produces speckle when illuminated with laser light. This can be treated as a Gaussian random process for which a fairly large literature exists [2.1.12].

The second source of scattering is the zone edges which are not ideally smooth but are really serrated apertures. Little has been done concerning the diffraction pattern of such apertures. (See a recent paper Ref. [2.1.13].) The mathematics becomes exceedingly involved because symmetry is destroyed, and the formalism employed before cannot be used.

If we consider one-dimensional gratings as shown in Fig. 2.1.6, the grain noise contribution can be seen but the serration is not easily visualized. In order to include the serration contribution to the one-dimensional model, we have to consider an ensemble of one-dimensional zone plates (or gratings) with grooves that vary randomly.

To make such a treatment we let  $r_n = r_n^0 + \delta_n(r_n)$ ;  $r_n$  is the radius of a certain zone  $r_n^0$  is the radius of an ideally smooth zone;  $\delta_n(r_n)$  is a random variable. In general, if the aperture function for one member of the ensemble is  $Z(t)$ , and that for the ideal zone plate is  $Z^0(t)$  then we may write  $Z(t) = Z^0(t) + E(t)$  where  $E(t)$  is a random process with spaces of random width. (In two dimensions the problem is more complicated because  $r_n(\phi)$  is also a function of the angle (Fig. 2.1.7) i.e.,  $r_n(\phi) = r_n^0 + \delta_n(r_n, \phi)$ .)

Consider the one-dimensional case.  $E(t)$  is illustrated in Fig. 2.1.8,c. This is a stochastic process with a few restrictions:  
 1.  $E(t)$  can have only 2 values  $-1, +1$ . 2. The spikes have a random width lying between zero and  $q/L$ . 3. One edge of the function is always located at  $t=nq$ . In Fig. 2.1.8.d we see that this random process can be described as a series of impulses. Let  $t_j$  be the solution of the equation:

$$\sin \left\{ \pi \left[ \frac{1}{q} t + \phi(j, q) \right] \right\} = 0 \text{ or } \pi \left[ \frac{t_j}{q} + \phi(j, q) \right] = j\pi$$

where  $j=1, 2, 3, \dots$  and where  $\phi(j, q)$  is a discrete random process satis-

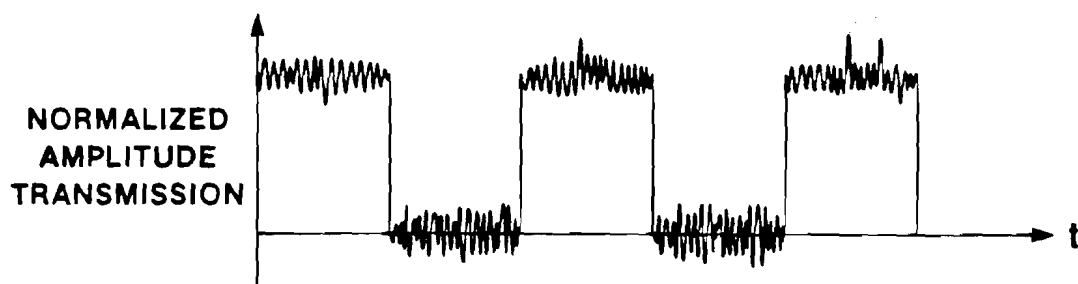


**Fig. 2.1.6**  
Grain noise in a zone plate recorded on film or surface roughness fluctuations in a reflection diffraction grating.  $t$  is the distance square coordinate for a zone plate or the real distance coordinate for gratings.

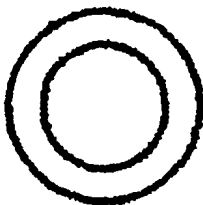


**Fig. 2.1.7**  
A representation of a zone plate (only 2 zones) with the serration introduced in the manufacturing process.

ying  $-\frac{q}{L} \leq \phi(j,q) \leq \frac{q}{L}$  and for every  $j$ ,  $\phi(j,q)$  is a uniformly distributed random variable in the interval  $\left[-\frac{q}{L}; \frac{q}{L}\right]$ . Also let  $N(j)$  be another discrete random process which assumes with probability  $1/2$  for odd or even integral values. With these definitions the random process in Fig. 2.1.8 d can be written as:

$$E(t) = \sum_{j=1}^N \delta(t - t_j) \cdot \cos\left[N(j) \frac{\pi}{2}\right]$$

Consider the diffraction pattern of  $Z(t)$ :  $\tilde{Z}(u) = \tilde{Z}^0(u) + \tilde{E}(u)$ .

The serration acts to produce an additive noise. Calculating  $\langle \tilde{E}(u_1) \tilde{E}(u_2) \rangle$  and  $\langle |\tilde{E}(u)|^2 \rangle$  in terms of  $E(t)$  is possible by assuming stationarity. From  $\langle \tilde{E}(u_1) \tilde{E}(u_2) \rangle$  we may also find the power spectrum [2.1.14] and hence find the characteristics of the scattering on axis for a zone plate, (and on the plane where the diffraction is observed in the case of gratings). Using a one-dimensional model means that the errors are assumed symmetric in the zone plate. This is, of course, not a fully realistic model but it still gives a feeling of what to expect.

The grain noise, on the other hand, acts as a multiplicative noise so that  $Z(t) = Z^0(t) \cdot g(t)$ . Again assuming symmetrical noise we get  $\tilde{Z}(u) = \tilde{Z}^0(u) * \tilde{g}(u)$ . The grain noise spectrum thus convolves with the noise free pattern.

In Fig. 2.1.9 a comparison between the grating and zone plate cases is shown. In the grating case, Fig. 2.1.9.a, the speckle pattern is essentially the same at all orders because the orders

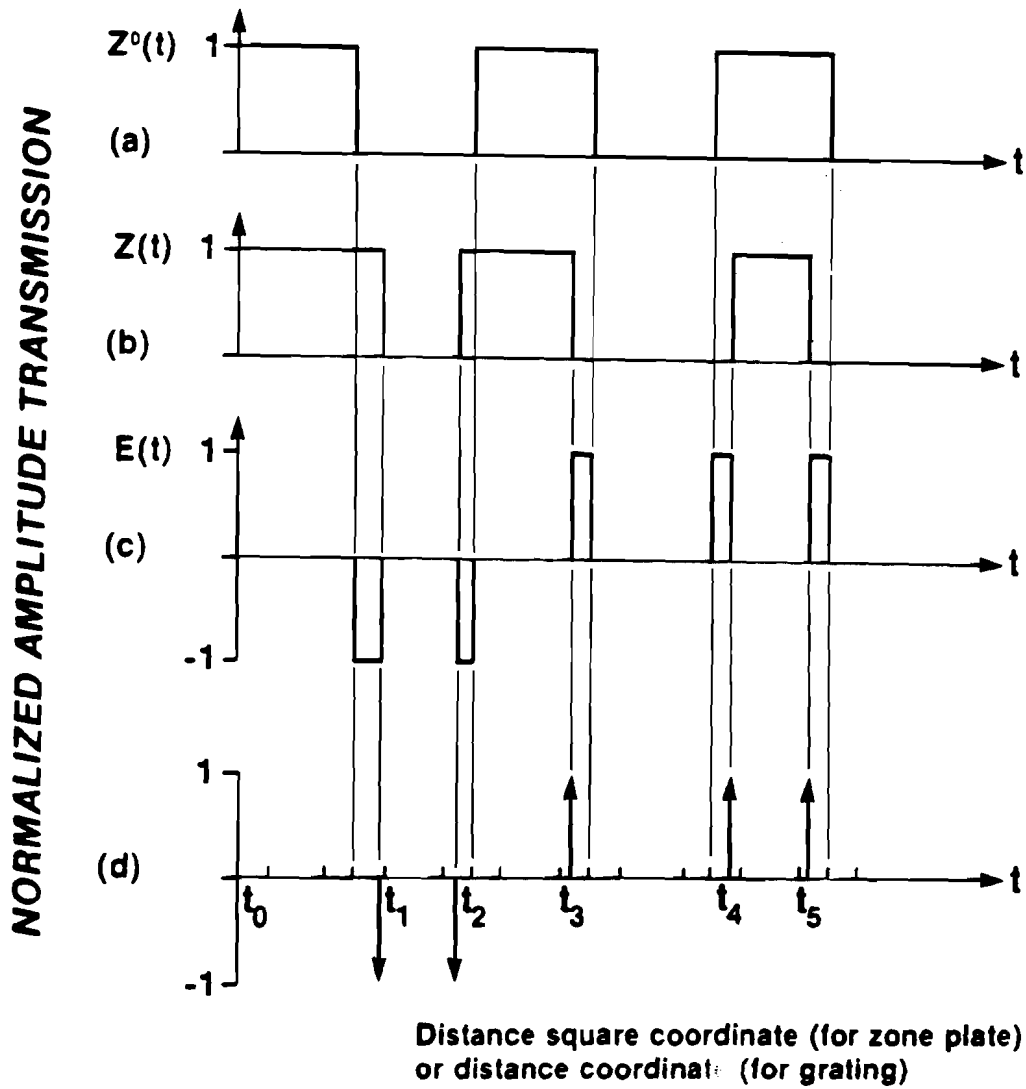


**Fig. 2.1.8**  
Modeling the noise introduced by random fluctuations in the zone radii or imperfections in the straightness of the diffraction grating grooves. (a)  $Z^o(t)$  is the ideal Fresnel zone plate, (b)  $Z(t)$  is the real zone plate, (c)  $E(t) = Z^o(t) - Z(t)$ , (d) random process that describes the deviation from an ideal zone plate.

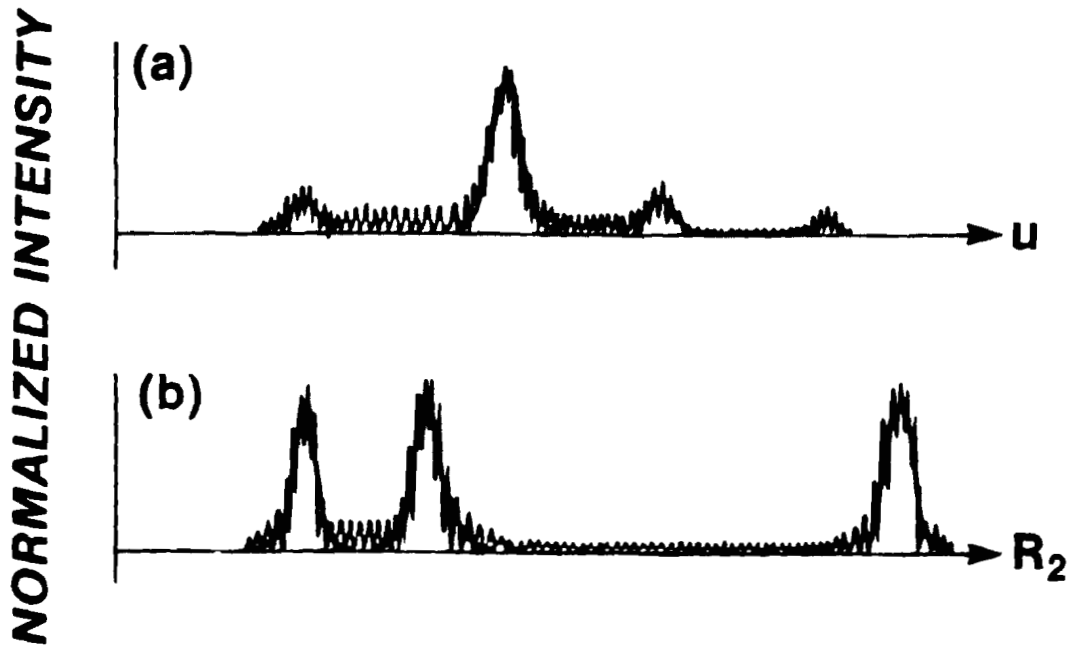


**Fig. 2.1.9**  
**Noise effects. (a) The noise convolves with the diffraction pattern in the case of gratings, (b) the noise convolves with the on axis intensity distribution in the case of zone plates.**

are equally separated. But in the case of zone plates the orders are not equally spaced and the convolved pattern at higher orders must shrink. Hence the appearance of the speckle pattern changes along the axis. (This discussion does not say anything about the transverse distribution of speckle in the different orders. This will be done when Fresnel transformations are considered in a later section.) If we want to examine the fainter high orders it may be useful to employ a converging light beam rather than a collimated light beam. This can reverse the relative axial location of the foci, making the grain noise contribution less severe.

The serration contributes background noise. The only way to reduce this type of noise is to manufacture a better quality zone plate with less serration.

#### 2.1.10 Aberrations in Zone Plates.

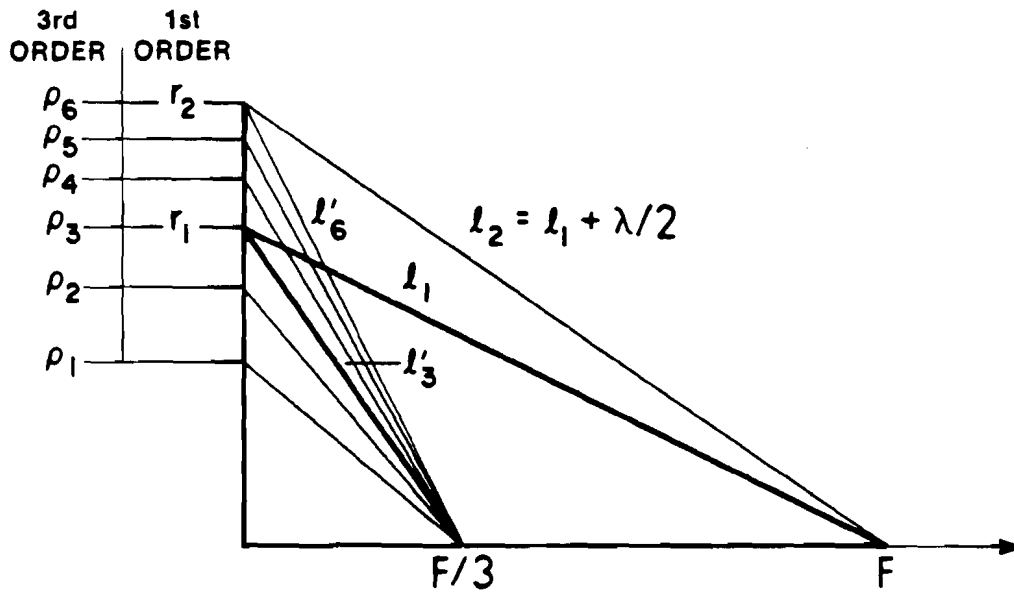
Third order contributions to the aberration function were calculated by Young [2.1.15]. The aberrations arise because of the error introduced in the derivation of (2.1.1), where the square root in the exponent was approximated only to first order.

The first remarkable feature about zone plates in this context is that there is no distortion term as with a regular lens since the chief ray does not deviate as it passes through the zone plate. The second interesting feature is that it is possible to correct for spherical aberration in the production process. One of the methods for manufacturing zone plates is by interfering a plane wavefront and an aspherical wavefront (or 2 spherical wavefronts). In Ref.

[1.14] a method is described, in which an aspheric wavefront is produced and interferes with another spherical wavefront so that the correction is built into the zone plate. In fact, we can always choose radii for two spherical wavefronts (i.e. you don't need an aspherical wavefront) such that by interference will produce the required correction. We thus get an optical device free of both spherical aberration and distortion. Furthermore, if we use the zone plate in the imaging mode, and if it is manufactured in the way which is discussed in an earlier section to enhance higher order efficiency, then by shifting an eye piece from order to order we can get a zooming effect without any additional element. The last two features have not yet been fully realized but it may become practical in the soft x-ray region.

Higher order reconstruction is important in the pseudoholography technique. At higher orders the  $F/\#$  is smaller, hence the aberrations become more pronounced. In Ref. [2.1.15] the condition for image quality of better than  $\lambda/4$  is  $N^2 < 2F/\lambda$ ; where  $N$  is the number of zones,  $F$  is the focal length, and  $\lambda$  is the wavelength of the reconstructing light beam. For  $f=10\text{cm}$ ,  $\lambda=5000\text{\AA}$ ,  $N < 600$  zones. In Fig. 2.1.10 we see an explanation for the fact that at a higher order  $p$  there are effectively  $pN$  zones. If we think of reconstructing at the sixth order we should not use a zone plate with more than 100 zones.

Chromatic aberration is also dependant on the number of zones. The pinhole camera - the simplest zone plate - is free of lateral color.



$$l'_6 = \sqrt{(F/3)^2 + r_2^2} \approx F/3 + \frac{3}{2} \frac{r_2^2}{F} = F/3 + \frac{3}{2} \cdot 2\lambda$$

$$l'_3 = \sqrt{(F/3)^2 + r_1^2} \approx F/3 + \frac{3}{2} \frac{r_1^2}{F} = F/3 + \frac{3}{2} \cdot \lambda$$

$$l'_6 - l'_3 = 3/2\lambda ; \quad l_2 - l_1 = \lambda/2$$

Fig. 2.1.10

At higher orders, the zones get narrower and the effective number of zones gets larger.

### 2.1.11 Computer Simulations.

In order to get a better feeling for the performance of the various zone plate designs, it is useful to plot the intensity distribution of the light at the different foci as a function of zone plate parameters such as  $N$  (the number of zones),  $EPS$  (the width of the individual zone: see Fig. 2.1.4.b) and the zone shape (see Fig. 2.1.4). Two kinds of plots are of interest to us: 1. the axial intensity distribution and 2. the transverse intensity distribution.

#### 2.1.11.1 Axial Intensity Distribution.

2.1.11.1.1. A discussion regarding a computer program that calculates the axial intensity distribution.

The axial distribution is given by Eq. (2.1.9)

$$G'(u) = \int_0^1 A(t) e^{2\pi i u t} dt \quad (2.1.9a)$$

If one is only interested in plotting this distribution in the  $u$  domain, then one can use the Fast Fourier Transform (FFT) algorithm to plot  $G'(u)$ . This distribution is observed in the case of the Fraunhofer diffraction from a grating. However, if we are interested in the axial intensity distribution from zone plates so we have to replot  $G(u)$ , scaling the coordinates in such a way as to get  $G(Z)$ , where  $Z$  is proportional to  $1/u$ . This is a subtle problem which it will be useful to discuss briefly.

We first obtain the discrete form of Eq. (2.1.9 a), the Discrete Fourier Transform (DFT):

$$G(m\Delta u) = \sum_{n=1}^N A(n\Delta t) \exp 2\pi i \frac{nm}{N} \cdot \Delta t \quad (2.1.9b)$$

Eq. (2.1.9.b) is obtained using the following definitions:

$$\Delta t = \frac{TOTD}{N-1} ; \quad \Delta u = \frac{N-1}{TOTD} \frac{1}{N} \quad (2.1.22)$$

where N is the number of samples used, m and n are integers, and TOTD is the size of the space in the input plane. (The size of the aperture itself may be only a fraction of TOTD as will be discussed later.)

From Eq. (2.1.15), (2.1.9 b) and (2.1.22) we may write the intensity distribution  $I(m\Delta u)$  as:

$$I(m\Delta u) = \text{ESCALE} \left| \sum_{n=1}^N A(n\Delta t) \exp 2\pi i \frac{nm}{N} \right|^2 \quad (2.1.9c)$$

where  $\text{ESCALE} = \left( \frac{a^2}{\lambda Z} \cdot \pi \cdot \frac{TOTD}{N-1} \right)^2$ . To find  $\Delta u$  from  $\Delta t$  we use:

$\Delta u = \text{USCALE} \Delta t$  where  $\text{USCALE} = \left( \frac{N-1}{TOTD} \right)^2 \cdot \frac{1}{N}$ .  $I(m\Delta u)$  is thus calculated

by the FFT algorithm and can be plotted using the scaling factors ESCALE and USCALE.

However, we would also like to plot the distribution in real space, i.e. Z space. If Z is the distance in an on axis from the zone plate and TOTDX is the extent of Z space then it is useful to define a quantity by  $Z = \zeta \text{TOTDX}$ . We usually choose  $\text{TOTDX} = F$  where F is the primary focal length. From Eq. (2.1.4),  $u = (a^2/2\lambda Z)$  for collimated light. But  $a^2 = (N \text{ZONE}) \lambda F$  and  $Z = F$ , therefore,  $u = \frac{N \text{ZONE}}{2} \cdot \frac{1}{\zeta}$

where NZONE is the number of zones. Let  $\bar{\zeta} = \frac{1}{\zeta}$ . If now we want to plot  $I(m\Delta\bar{\zeta})$  we have to scale  $\Delta\bar{\zeta} = \text{USCALE}(\bar{\zeta}) \cdot \Delta t$

where 
$$\text{USCALE}(\bar{\zeta}) = \frac{2}{\text{NZONE}} \cdot \frac{1}{N} \cdot \frac{(N-1)}{\text{TOTD}}$$

$\bar{\zeta}$  space is merely a scaled version of  $u$  space. To get the intensity distribution in terms of  $Z = \zeta F = \frac{F}{\zeta}$  we plot  $I(m\Delta\bar{\zeta})$  as a function of  $\frac{1}{\zeta}$ .

The interpolation of sampled data is an important problem in such calculations. As an example suppose that TOTD is the extent of the input space, and A is the width of the aperture function. The sampling interval is  $\Delta = \frac{\text{TOTD}}{N-1}$  in the input space. Therefore, in the transform space the sampling interval will be  $\delta = \frac{1}{\text{TOTD}}$  or  $\delta = \frac{\lambda Z}{\text{TOTD}}$  cm. From this the total width of the transform space is  $\text{TBDM} = \frac{N\lambda Z}{\text{TOTD}}$  (see Fig. 2.1.11 for a visualization of these quantities). If A is comparable with TOTD then the corresponding width in the Fourier domain will be very small with respect to the total space size  $N/\text{TOTD}$  (Fig. 2.1.11.B). To exhibit the pattern we scale down the space coordinate and interpolate between the values of  $I(m\Delta\bar{\zeta})$ . If the scaling factor is too large we may get erroneous results. Therefore, if we choose A to be a small fraction of TOTD then the width in the transform plane will be large compared with the total space size and we will not need to scale and interpolate. However, to do that we will need many more data points so that a compromise must be made.

One of the interpolation procedures is the polynomial inter-

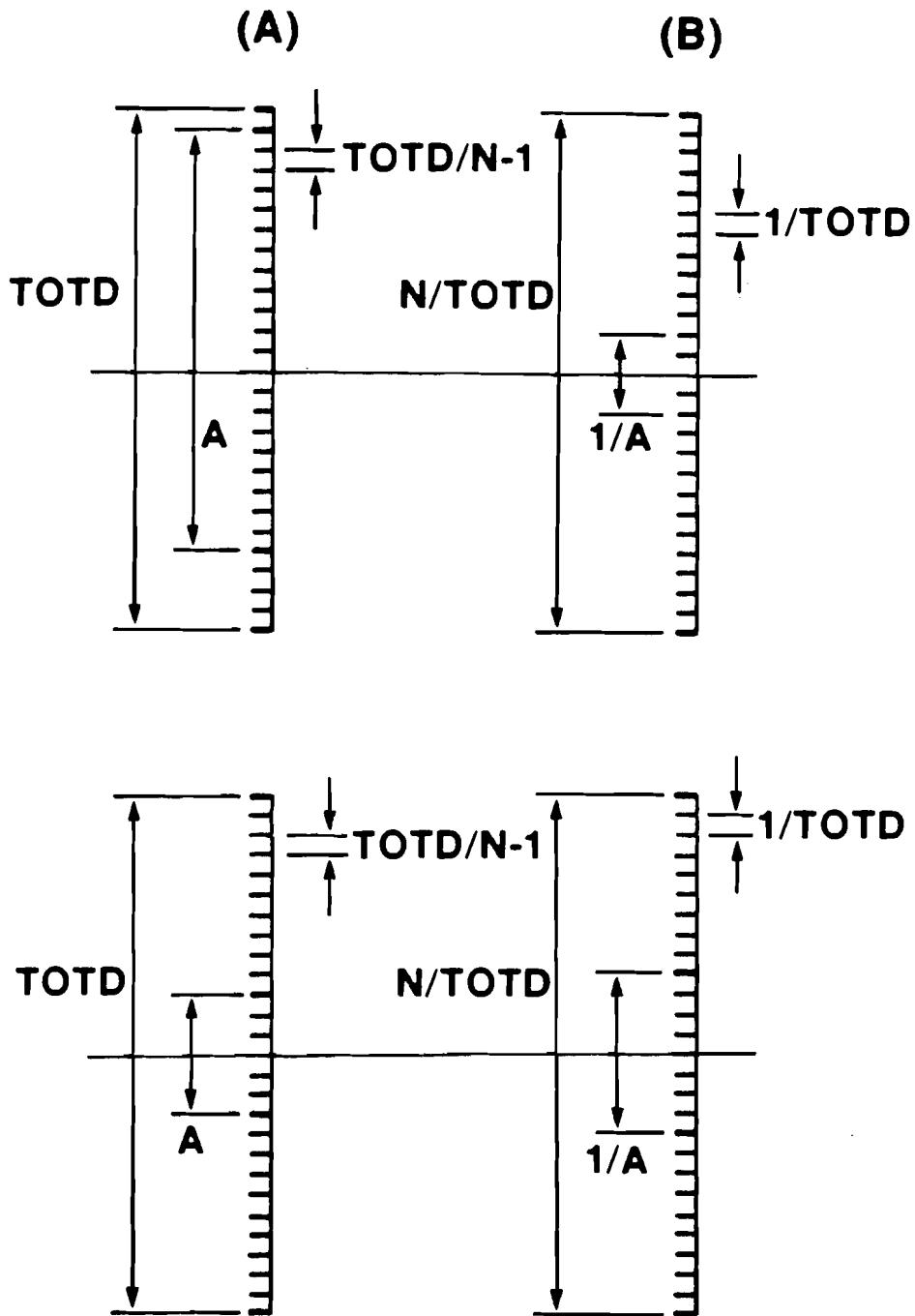


**Fig. 2.1.11**  
Relation between the extent of the input function (A) and the extent of the output function (B) when using the FFT algorithm to compute the Fourier transform of a sampled function.

polation where we fit a polynomial through four successive data points, and then calculate from this polynomial the intermediate data points (see Ref. [2.1.17]). The main problem with this procedure is that it tends to give erroneous results when we scale the plots by a factor larger than 2. To reduce the error we may fit the polynomial through more than four data points but with greatly increased computing time.

Another procedure is described in Ref. [2.1.17]. It is based on the sampling theorem (see Ref. [2.1.14]) by which every band limited function can be fully reconstructed from an infinite series of sampled data values, provided that the sampling frequency is not less than twice its bandwidth. Here errors arise from the fact that we cannot obtain an infinite series of points. However, it turns out that if the parameters are chosen carefully this procedure may be better than the previous one for equivalent computing times.

A computer program based on the remarks mentioned above was written and is listed in Ap. 1.

2.1.11.1.2 Conclusions from the plots obtained by the computer program.

The distribution in the  $1/z$  domain is the familiar Fraunhofer diffraction pattern of a grating and we will not plot it here. However, the distribution in the real space  $z$  is of considerable interest to us here. The different cases are summarized in Table 2.1.4. EPS1, EPS2, B1 and B2 are defined in Fig. 2.1.12. In Fig. 2.1.13 a the case of an idealized Fresnel zone plate is plotted.

Table 2.1.4: Parameters of the Different Computer Runs,  
Calculating the On Axis Intensity Distribution from Zone Plates

<u>Run #</u>	<u>(NZONE) # of Zones</u>	<u>POSITIVE or NEGATIVE Zone Plates</u>	<u>EPS1</u>	<u>EPS2</u>	<u>B1</u>	<u>B2</u>	<u>(N) # of Points</u>	<u>Fig. #</u>
1	37	POSITIVE	0.5	0.5	0.5	0.5	3645	2.1.13a
2	37	POSITIVE	0.5	0.5	0.3	0.3	3645	2.1.13b
3	37	POSITIVE	0.4	0.4	0.4	0.4	3645	2.1.14a
4	37	POSITIVE	0.4	0.4	0.3	0.3	3645	2.1.14b
5	11	POSITIVE	0.5	0.5	0.5	0.5	3645	2.1.15

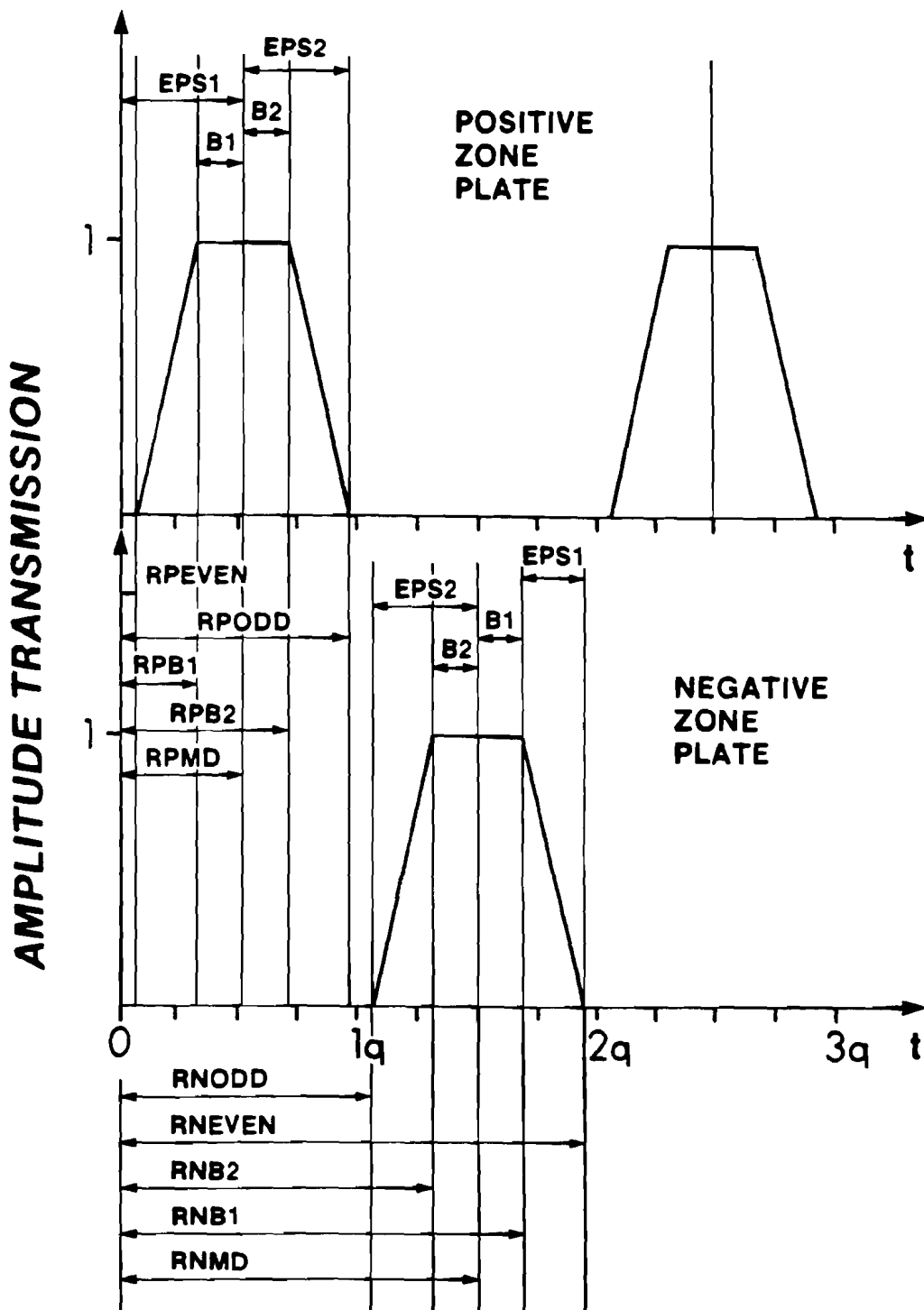
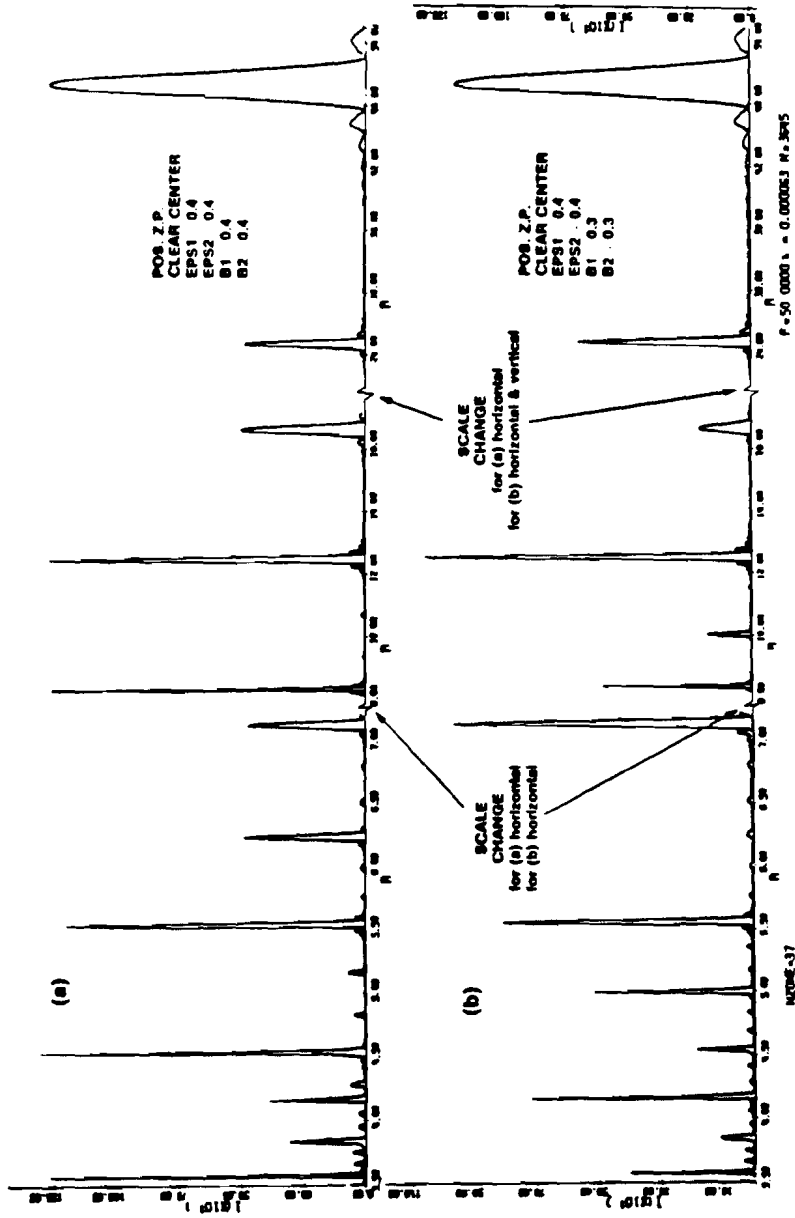


Fig. 2.1.12  
 Definitions of all the relevant quantities used to represent a zone plate in the computer program. (t is the square distance coordinate.)



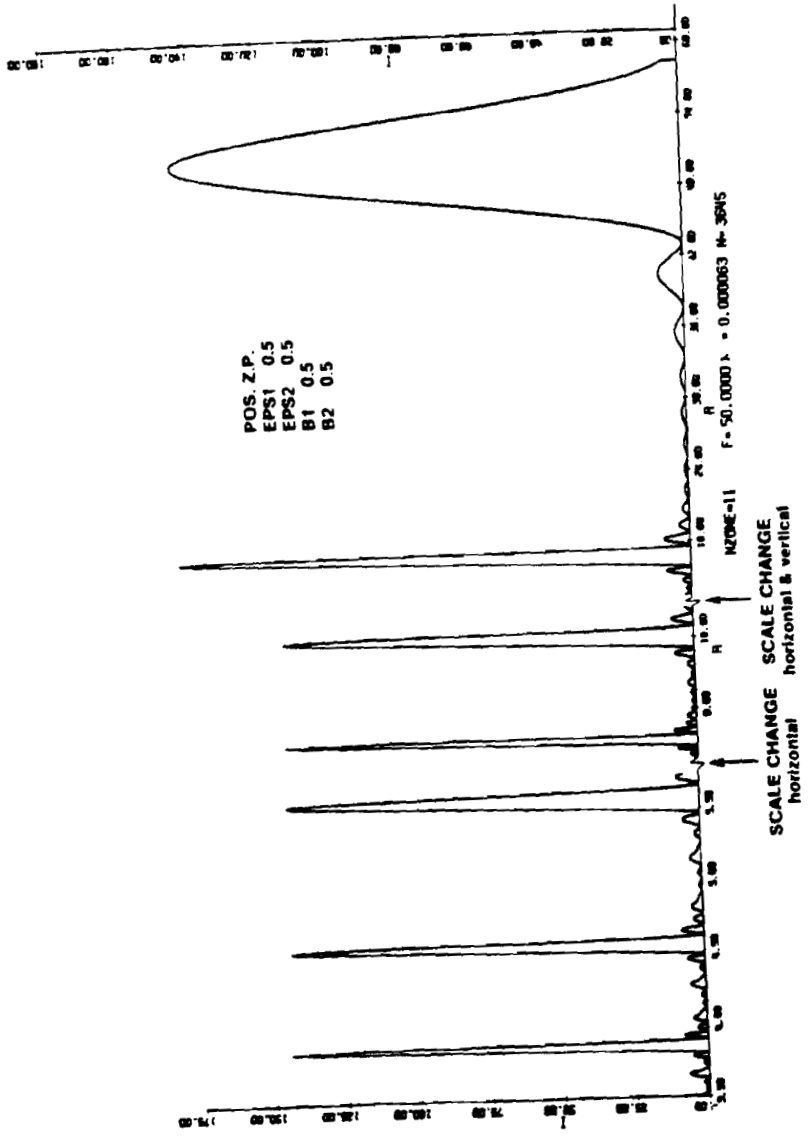
Only odd foci appear and all have exactly the same on axis intensity as predicted by Eq. (2.1.17). In order to show the different orders the plot had to be scaled up at higher orders. The case 37 zones was depicted since this is the number of zones in the zone plate used in the x-ray experiment. In the first order the width of the spike is quite large: about 3cm. This limits seriously the tomographic capability of the system. No attempt was made to calculate higher orders than the 11th order. In Fig. 2.1.13.b the case of the same zone width but with slanted edges is plotted. Even orders appear but they are strongly attenuated. The odd orders are also attenuated. The decrease in the width at higher orders is clearly demonstrated enabling higher tomographic resolution at higher orders. Although the effect of slanted edges is to attenuate the higher orders we may still find orders with appreciable on axis intensity in this case. In Fig. 2.1.14 two cases with narrow zones are plotted. In Fig. 2.1.14.a the edges are straight, while in Fig. 2.1.14.b they are slanted. Comparing Fig. 2.1.14.b with 2.1.13.b we see that when the zones are narrower, slanted edges do not cause as much attenuation as with zones which have the ideal width of a Fresnel zone plate. This suggests that we may be able to design a zone plate where high orders have still an appreciable on axis intensity in spite of the fact that diffraction effects are present in the recording step of the pseudohologram.

In Fig. 2.1.15 the case of 11 zones is shown, to demonstrate the critical dependence of the width of the orders as function of the number of zones in the zone plate. In this case the first order



### 2.1.14

**Axial intensity distribution of light focused by a zone plate of 37 zones. (a) Narrow and sharp zones (EPS=0.4, B=0.4). (b) Narrow zones with slanted edges (EPS=0.4, B=0.3).**



2.1.15 Axial intensity distribution of light focused by a Fresnel zone plate of 11 zones.

extends over 18cm while in Fig. 2.1.14, over 3cm.

#### 2.1.11.2 Transverse Intensity Distribution.

For a fixed  $Z$  Eq. (2.1.1) gives the transverse intensity distribution. Using the small angle approximation (e.g. (2.1.2) and (2.1.3)), Eq. (2.1.1) can be written as a Fresnel transformation. A computer program is available to calculate this integral (see Ref. [2.1.17]). This program was modified to suit our needs and used to plot the transverse intensity distribution as a function of  $N$ ,  $EPS$ , and zone shape. The calculation was done for the case where a plane wave is incident on a zone plate and is brought to a series of foci.

The different cases are summarized in Table 2.1.5

##### 2.1.11.2.1 Effect of the zone shape on the intensity distribution of the various orders.

In Fig. 2.1.16 we plot two cases: (a) the ideal Fresnel zone plate ( $EPS = 0.5$ ), (b) zone plate with narrow zones. In the case (a) the even orders are very weak, about two orders of magnitude weaker than the odd orders. In theory they should be zero but since we are sampling the aperture with finite number of points, an error is introduced and the even orders are not identically zero. All the odd orders are of equal height as predicted by Eq. (2.1.17). The width reduces from about  $200\mu\text{m}$  in the first order to about  $20\mu\text{m}$  in the 9th order. In the case (b) even orders appear and can become quite strong. In this case some higher orders are even stronger than the first order (for example, 2nd order and fifth order). Hence,

Table 2.1.5: Parameters describing the plots in section 2.1.11.2

<u>#</u>	<u>NZONE</u>	<u>EPS1</u>	<u>EPS2</u>	<u>B1</u>	<u>B2</u>	<u>F</u>	<u>N</u>	<u>Fig. #</u>	<u>POS/ NEG</u>	<u>Order</u>	<u>Dim.</u>
1	37	0.5	0.5	0.5	0.5	150	2048	2.1.16a	POS	1-10	2
2	37	0.3	0.3	0.3	0.3	150	2048	2.1.16b	POS	1-10	2
3	11	0.5	0.5	0.5	0.5	150	2048	2.1.17a	POS	3	2
4	33	0.5	0.5	0.5	0.5	50	2048	2.1.17b	POS	1	2
5	11	0.5	0.5	0.5	0.5	50	2048	2.1.17c	POS	1	2
6	Lens	---	---	---	---	50	2048	2.1.17d	---	---	2
7	11	0.5	0.5	0.5	0.5	150	6144	2.1.18a	POS	1,3,5	1
8	37	0.5	0.5	0.5	0.5	150	6144	2.1.18b	POS	1,3,5	1
9	61	0.5	0.5	0.5	0.5	150	6144	2.1.18c	POS	1,3,5	1
10	11	0.5	0.5	0.5	0.5	150	6144	2.1.19a	NEG	1,3,5	1
11	37	0.5	0.5	0.5	0.5	150	6144	2.1.19b	NEG	1,3,5	1
12	61	0.5	0.5	0.5	0.5	150	6144	2.1.19c	NEG	1,3,5	1

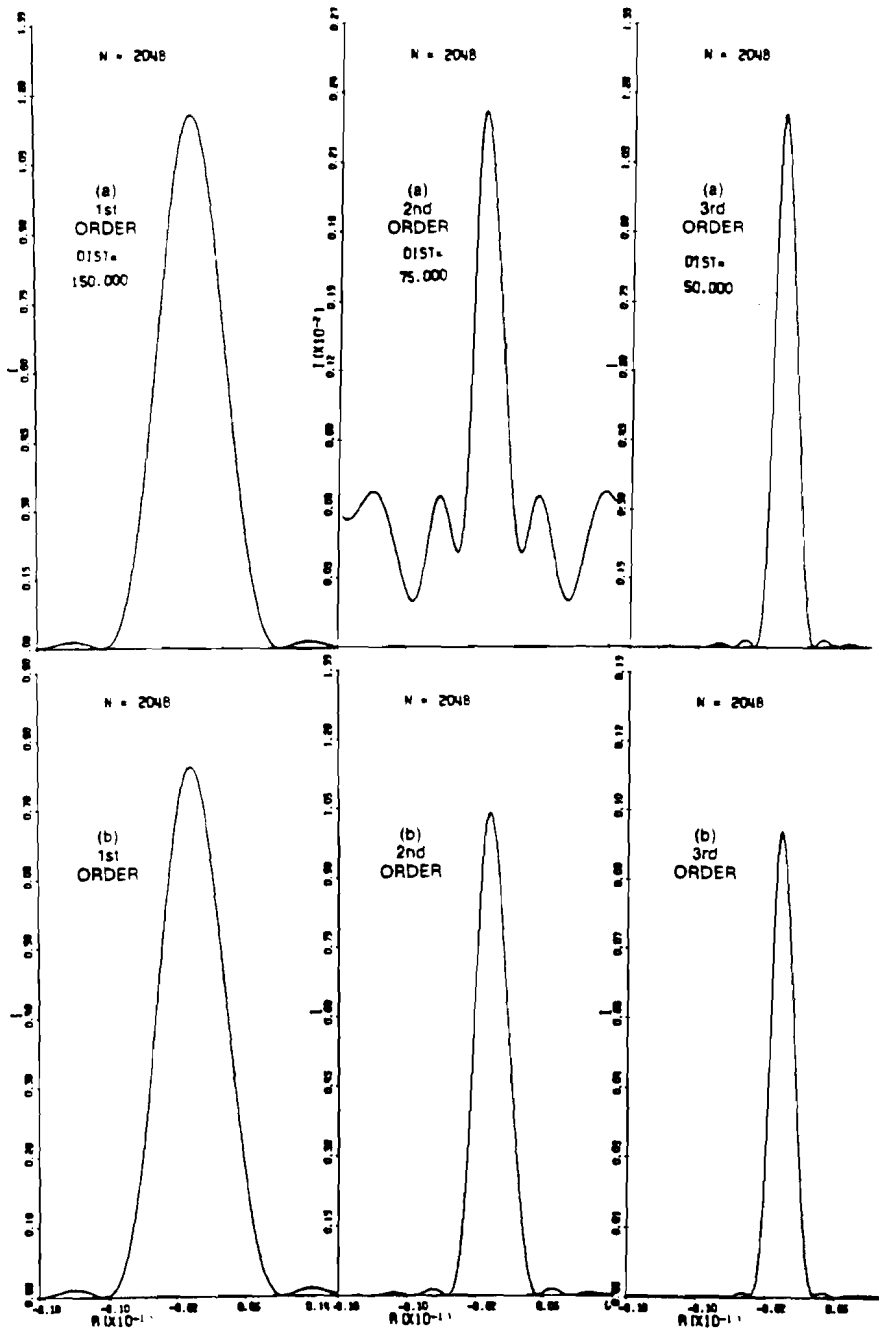


**Fig. 2.1.16**  
Transverse intensity distribution at various orders of light focused by a zone plate. (a) Fresnel zone plate (EPS = 0.5), (b) modified zone plate (EPS = 0.3) (See Fig. 2.2.12 for notation.)

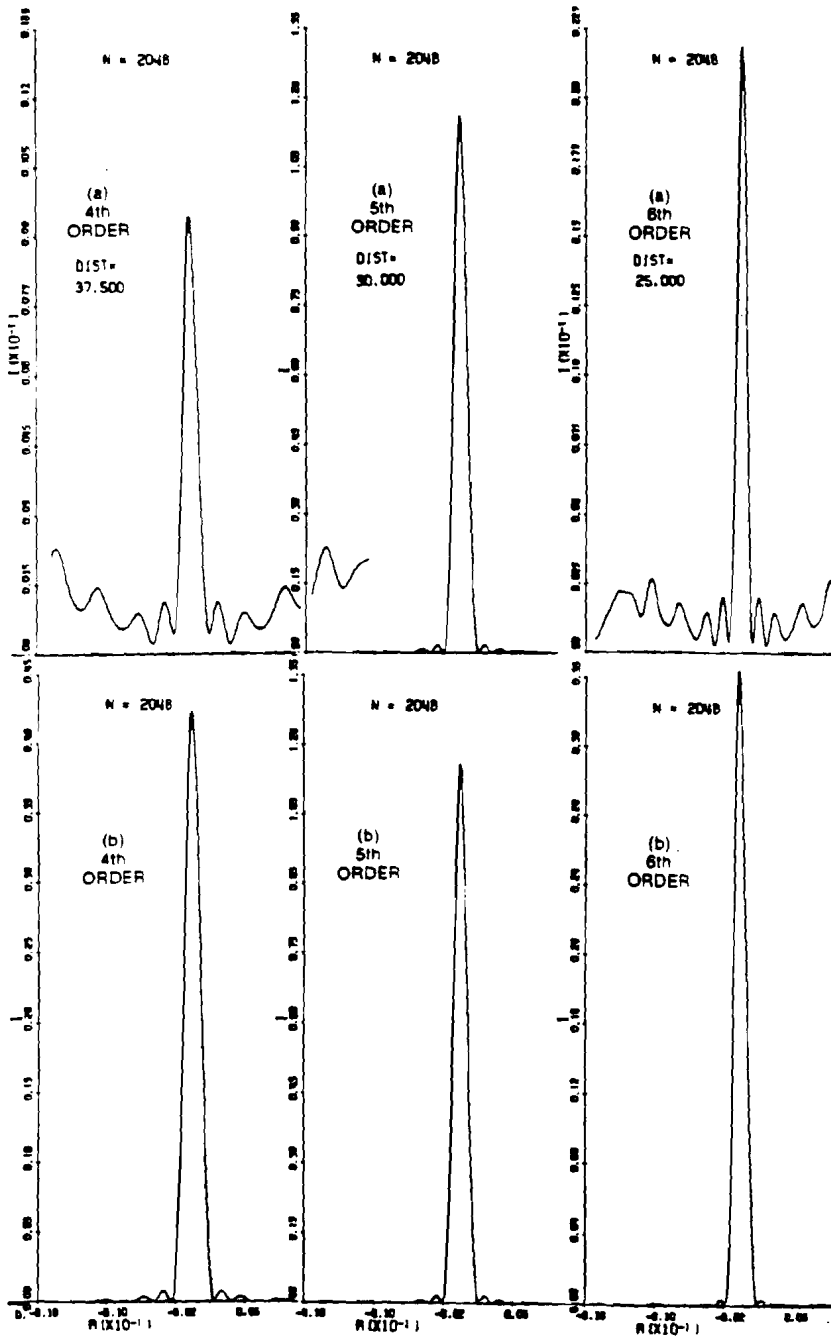


Fig. 2.1.16 (cont.)

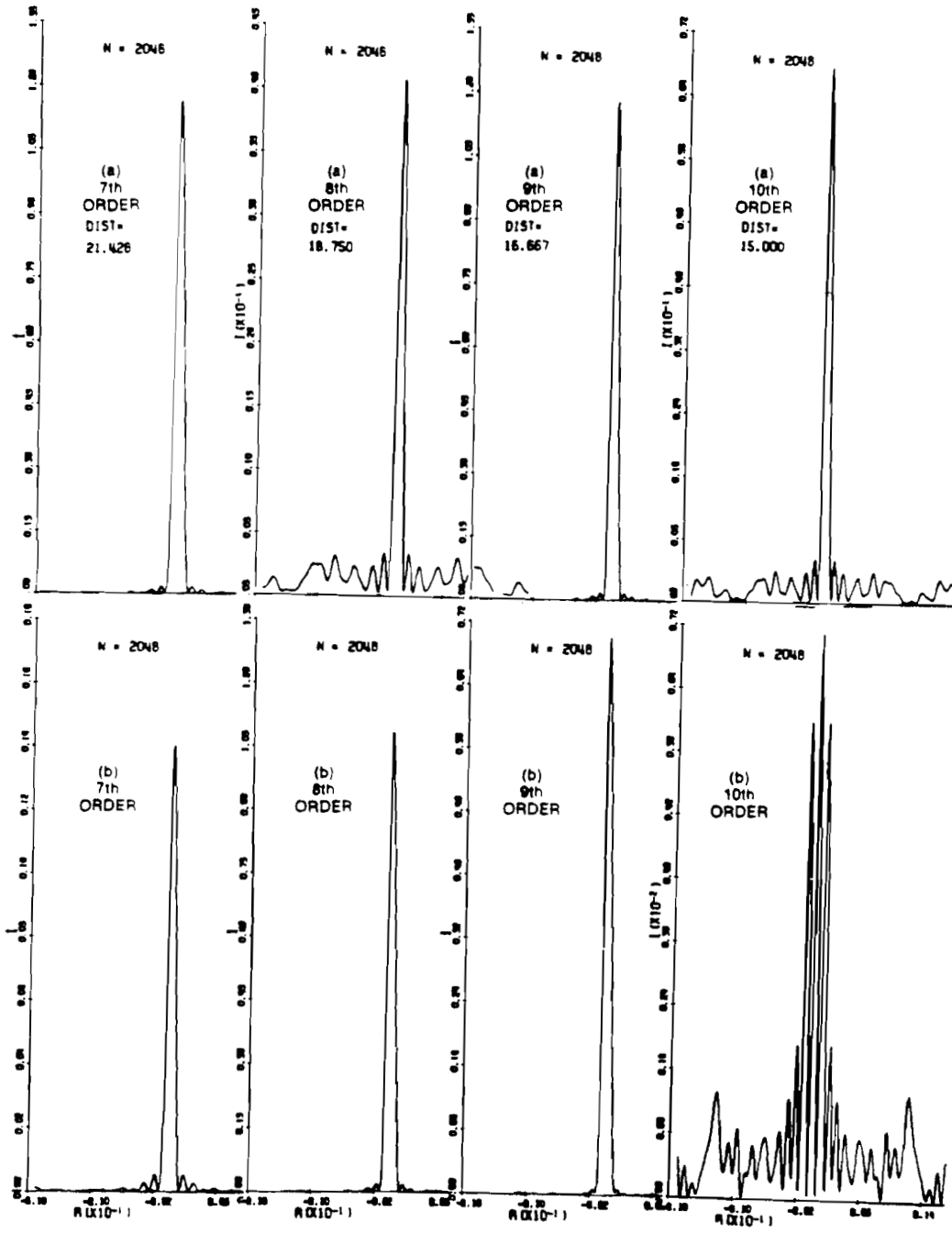


Fig. 2.1.16 (cont.)

narrowing the zones has sometimes the effect of blazing the zone plate directing more light to higher orders at the expense of lower orders.

2.1.11.2.2 The effective number of zones increases at higher orders.

In Fig. 2.1.17.a we plot the transverse intensity distribution of a zone plate, of 11 zones and 150cm focal length, at the third order. In Fig. 2.1.17.b we plot the transverse intensity distribution of a zone plate, of 33 zones and 50cm focal length, at the first order. Since the  $F/\#$  is smaller in the latter case we get higher intensity but the shape of the curve and the width of the pattern are very similar. There is a little difference in the secondary lobes. In the case of 2.1.17.a the intensity of the secondary lobes does not decrease as fast as in 2.1.17.b. This causes background in imaging and in reconstruction at high orders of a pseudohologram. However, for larger number of zones this effect becomes negligible. We thus see that the effective number of zones at the third order of 2.1.17.a is the same as the number of zones at the first order of 2.1.17.b.

Also it is interesting to compare the transverse intensity distribution of a zone plate and a lens of comparable focal length and aperture. From 2.1.17.c and 2.1.17.d we conclude that the efficiency of a zone plate is approximately 12%. Also the third lobe in 2.1.17.c is higher than the second while in 2.1.17.d the intensity of the secondary lobes decreases fast as a function of the distance from the center. This again demonstrates the problem when using a zone plate with small number of zones, i.e.: the secondary lobes contribute to the background and decrease the signal to noise ratio.

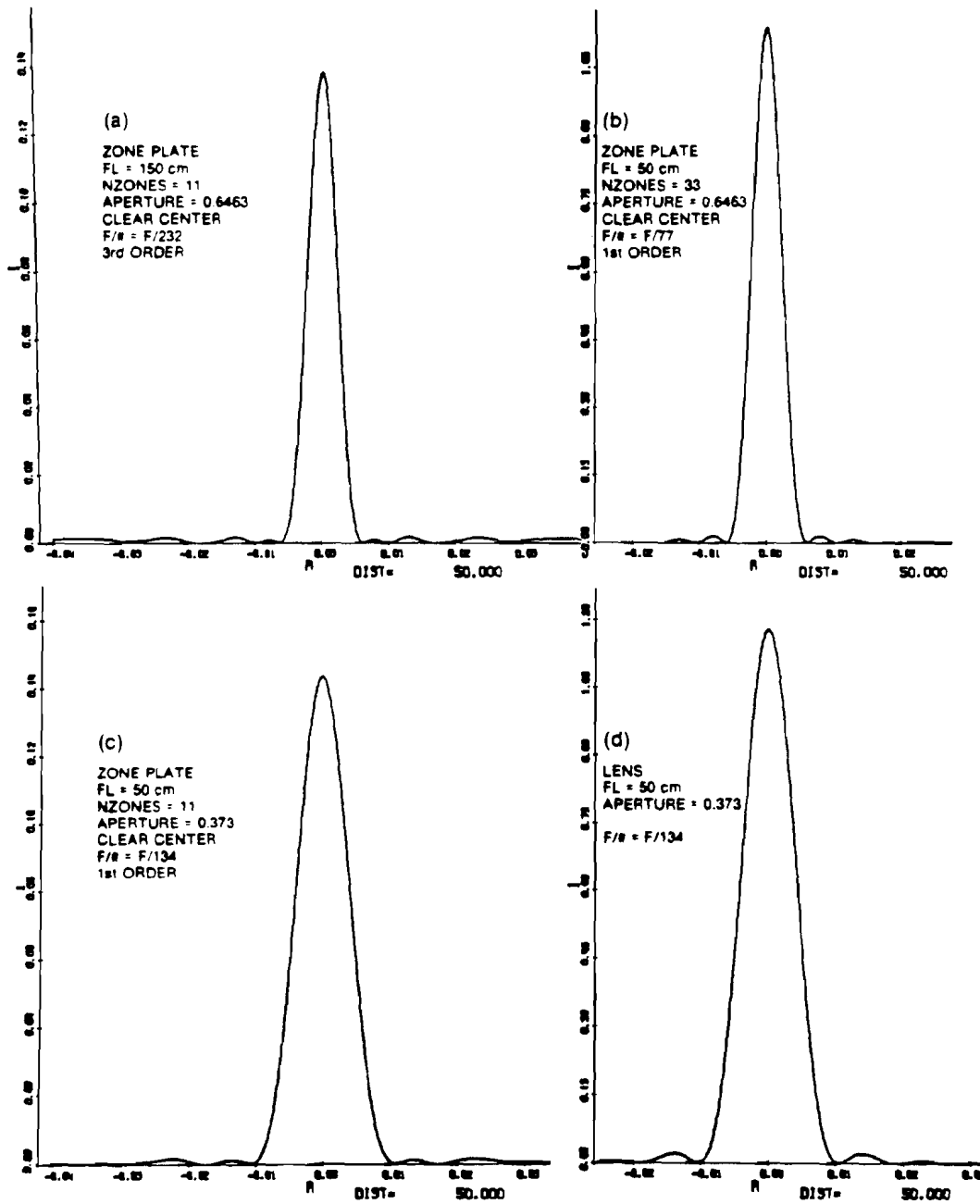


**Fig. 2.1.17**  
**Transverse intensity distributions focused by zone plates and a lens.**

### 2.1.11.2.3 Comparison between one-dimensional and two-dimensional zone plates.

In Fig. 2.1.18 the transverse intensity distributions of light focussed by one-dimensional zone plates are shown. By comparing Fig. 2.1.18 with 2.1.16 and 2.1.17 we conclude that two-dimensional zone plate pseudoholography is much more efficient than one-dimensional zone plate pseudoholography. First of all the on axis intensity decreases at higher orders while for the two-dimensional case it does not change. And secondly, the background problem is much more severe in the one-dimensional case. In order to achieve satisfactory results, we must use a one-dimensional zone plate with at least 100 to 150 zones. In the two-dimensional case, on the other hand, 40 zones will give reasonably good reconstruction. In Fig. 2.1.19 the case of negative one-dimensional zone plate is illustrated. It can be seen that as long as the object is smaller than the innermost zone then the one-dimensional zone plate is still useful for pseudoholography.

If higher order reconstructions are needed then the object size is further limited as can be seen in Fig. 2.1.19 at DIST = 50 or DIST = 30, which correspond to third and fifth orders respectively.

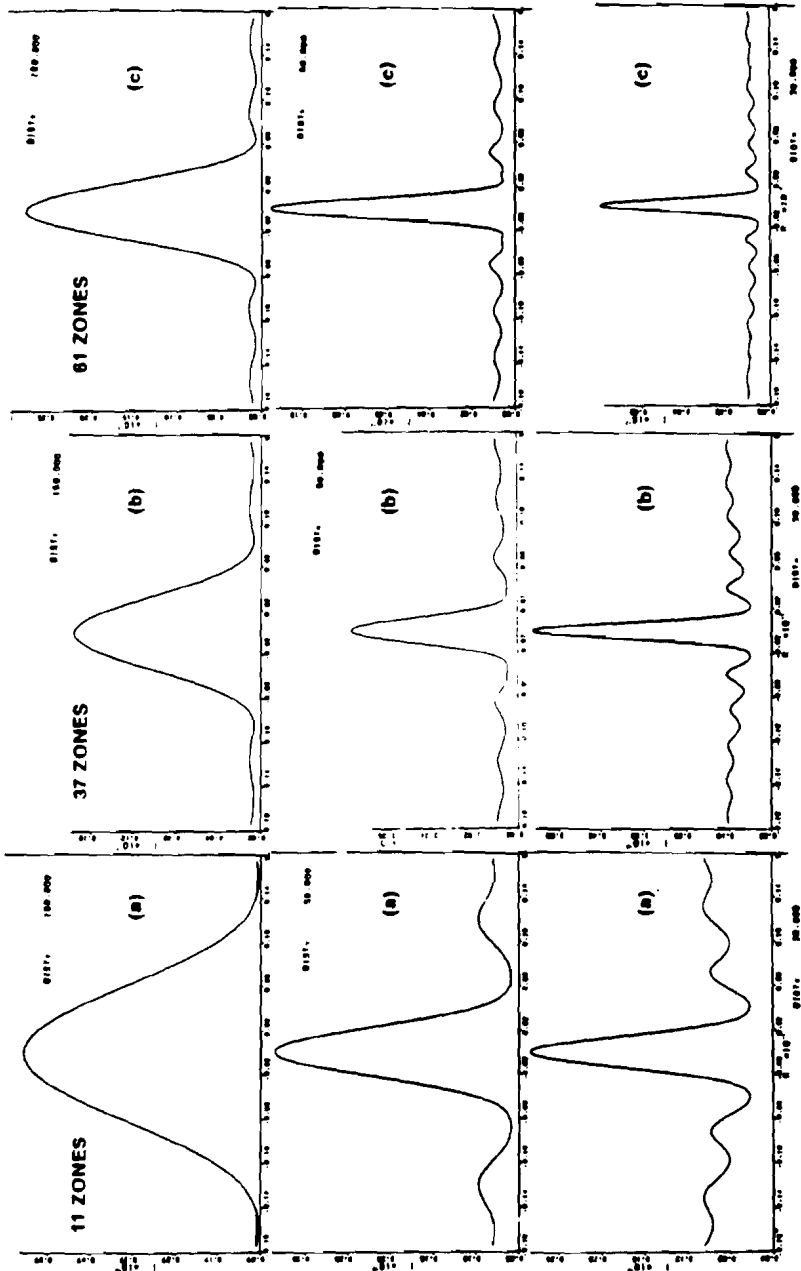


**Fig. 2.1.18**  
Transverse intensity distributions of light focused by one dimensional positive zone plates. DIST is the distance from the zone plate in cm, 150 cm being the front order focus. (a), (b) and (c) are 11, 37, 61 zones zone plate cases respectively.

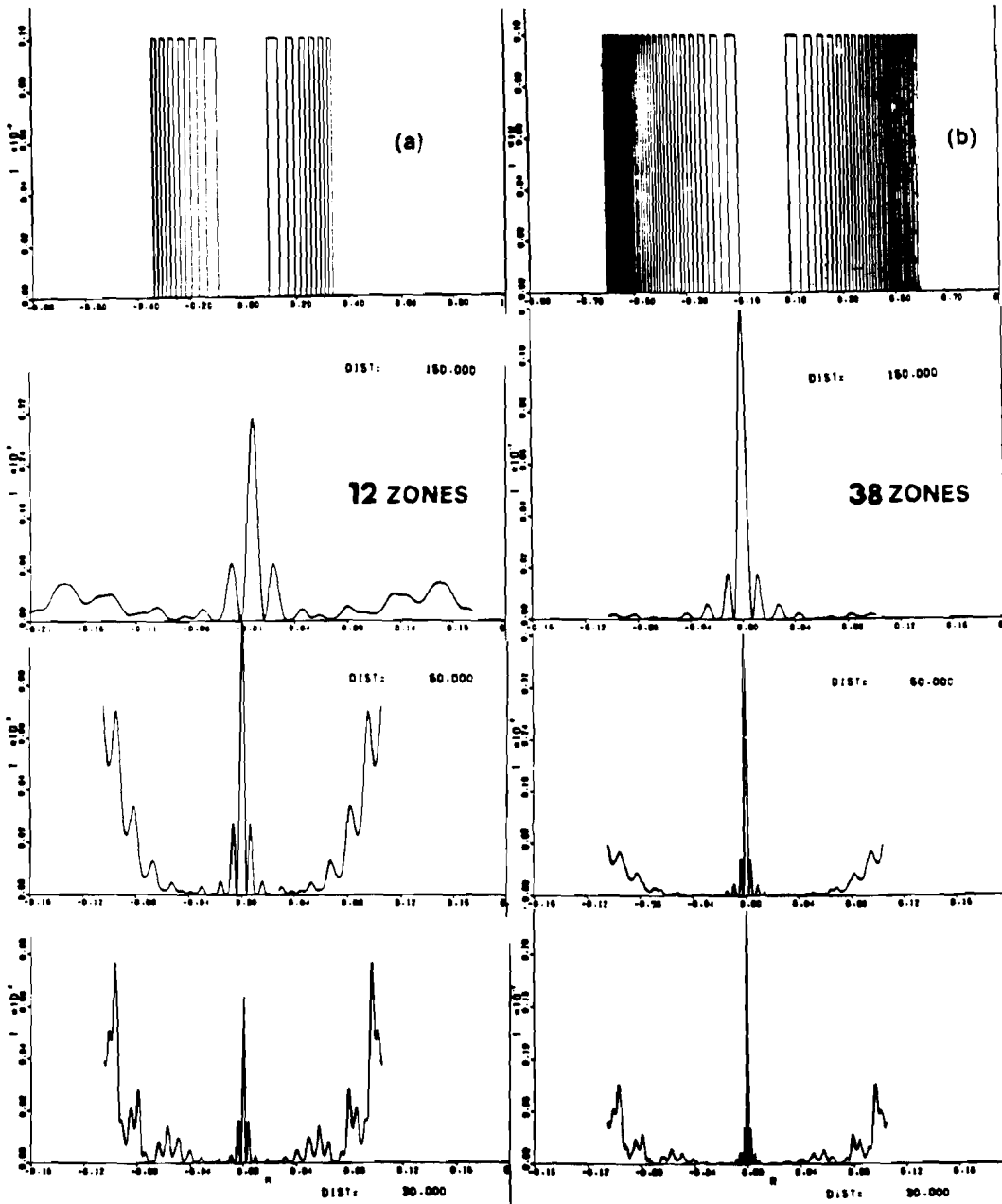


**Fig. 2.1.19**  
Transverse intensity distributions of light focused by one dimensional negative zone plates. DIST = 150, 50, 30 correspond to the first, third and fifth order foci. (a), (b) and (c) are 12, 38 and 62 zones zone plate cases respectively.

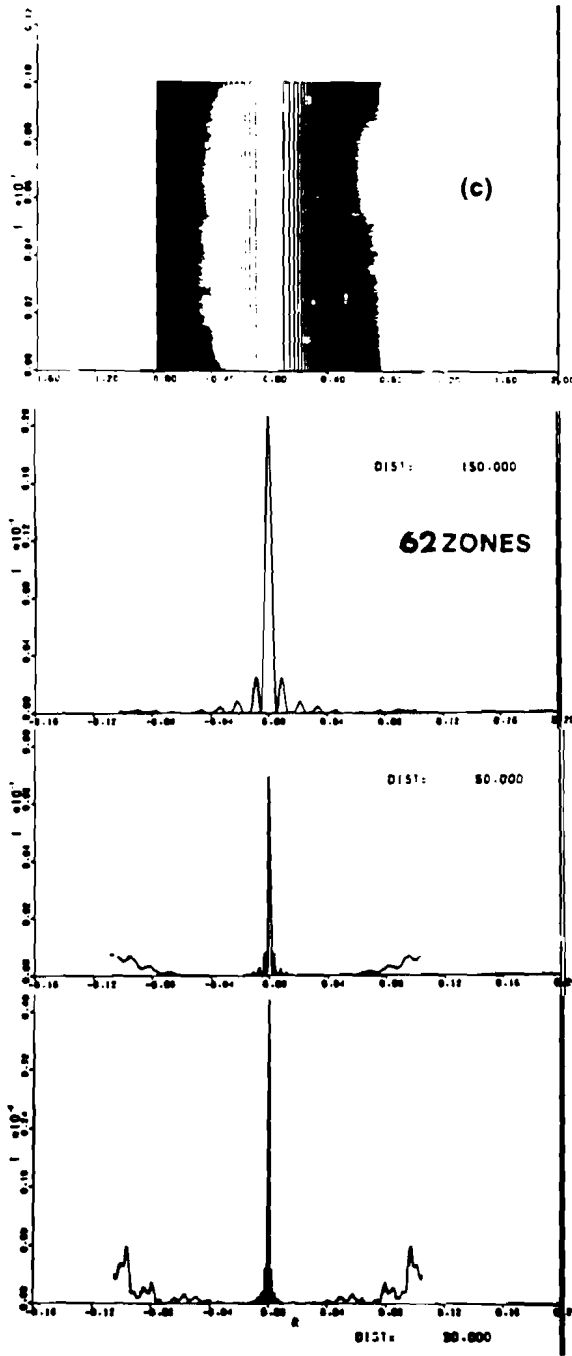


Fig. 2.1.19 (cont.)

2.1.12 REFERENCES

- 2.1.1 M. Born and E. Wolf, "Principles of Optics", (Pergamon press)  
5th Edition.
- 2.1.2 J. W. Goodman, "Introduction to Fourier Optics", (McGraw-Hill)  
1968, p. 12, eq. 2-14.
- 2.1.3 R. G. Simpson and H. H. Barrett, "Coded Aperture Imaging" in  
"Imaging in Diagnostic Medicine", Ed. S. Nudelman (Plenum  
Publishing Corp., NY).
- 2.1.4 Alberic Boivin, "On the Theory of Diffraction by Concentric  
Arrays of Ring-Shaped Apertures", J. Opt. Soc. Am. 42, 60 (1952).  
See discussion following Eq. 28, p. 63. The conditions for  
maxima  $y=(2j+1)2\pi$  are given but he does not stress the fact  
that  $\omega$  too changes in the same way.
- 2.1.5 Milburn Sussman, "Elementary Theory of Zone Plates", Am. J.  
Phys. 28, 394 (1960). See Fig. 4, p. 396.
- 2.1.6 Henri Arsenault, "Diffraction Theory of Fresnel Zone Plates",  
J. Opt. Soc. Am. 58, 1536 (1968). See Eq. 11 and the immediate  
conclusion that irradiance goes as  $1/(2j+1)^2\pi^2$ .
- 2.1.7 There is a series of papers discussing the efficiency of higher  
orders.
- (a) G. S. Waldman, J. Opt. Soc. Am. 56, 215 (1966).
- (b) M. H. Harmon and H. H. M. Chan, "Zone Plate Theory Based  
on Holography", Appl. Opt. 6, 317 (1967).
- (c) Kenneth I. Clifford and Gary S. Waldman, "Comments on Zone  
Plate Theory Based on Holography", Appl. Opt. 6, 1415 (1967).

- (d) M. Horman, "Reply to Comments on Zone Plate Theory Based on Holography", Appl. Opt. 6, 1415 (1967).
- 2.1.8 J. Kirtz, "Phase Zone Plates for X-Rays and the Extreme U.V.", J. Opt. Soc. Am. 64, 304 (1974).
- 2.1.9 L. S. Cheo, J. Shmoys and A. Hessel, "On Simultaneous Blazing of Triangular Groove Diffraction Gratings", J. Opt. Soc. Am. 67, 1686 (1978).
- 2.1.10 E. V. Jull, J. W. Heath, and G. R. Ebbeson, "Gratings That Diffract All Incident Energy", J. Opt. Soc. Am. 67, 557 (1977).
- 2.1.11a A. Walsh, "Echelette Zone Plates for Use in Far Infrared Spectrometry", J. Opt. Soc. Am. 42, 213 (1952).
- 2.1.11b N. M. Ceglie and H. I. Smith, "An Efficient Lensing Element for X-Rays", 8th International Conference on X-Ray Optics and 12th Annual Conference of the Microbeam Analysis, Aug. 1977, Boston, Mass. p. 202A.
- 2.1.12 (a) J. C. Dainty Ed., "Laser Speckle and Related Phenomena", Springer - Verlag (1975).
- (b) J. C. Dainty, "The Statistics of Speckle Patterns", Progress in Optics, E. Wolf Ed., North Holland (1976).
- 2.1.13 N. George and G. M. Morris, "Randomly Serrated Edges, Lines, and Apertures", J. Opt. Soc. Am. 67, 1416 ThK77 (1977).
- 2.1.14 A. Papoulis, "Probability Random Variables and Stochastic Processes", McGraw-Hill (1965).
- 2.1.15 M. Young, "Zone Plates and Their Aberrations", J. Opt. Soc. Am. 62, 972 (1972).
- 2.1.16 J. F. James and R. S. Sternberg, "The Design of Optical Spec-

trometers", (Chapman & Hall, Ltd., London 1969) p. 64.

2.1.17 E. Krisl, PhD. Thesis, "Apodization of Coherent Optical Systems", University of Rochester, (1978).

2.1.18 D. Stigliani, Jr., R. Mittra, R.G. Semonin, "Resolving Power of a Zone Plate", J. Opt. Soc. Am. 57, 610 (1967).

## 2.2 Limitations and Prospects of Pseudoholography.

The technique was introduced by Merz and Young [2.2.2] to astronomy, applied to nuclear medicine by Barrett [2.2.3] and to laser produced plasmas by Ceglie [2.2.4]. Although a theoretical treatment of pseudoholography has already been given (Ref. [2.2.1] and Ref. [2.2.14]) these authors overlooked the reconstructions at higher order foci. For certain x-ray imaging applications the importance of pseudoholography relies heavily on the fact that a significant increase of resolution occurs in the higher order reconstructions. It thus seems appropriate to rederive the relevant relations in pseudoholography, this time including the high orders as well.

The main limitation of this method is the fact that for an extended continuous source the signal to noise ratio in the reconstruction decreases significantly. This disadvantage is alleviated somewhat if the object is smaller than the innermost zone. Also, it has been assumed ([2.2.1], [2.2.2], [2.2.3], [2.2.4] and references therein) that the shadow casting process can be described strictly by geometrical optics. In practice the system is partially coherent and diffraction cannot generally be neglected. These effects will be included in our treatment of the propagation of the mutual intensity for describing the coded aperture shadowgraphy technique. This will allow us to discuss enhancement techniques in cases where diffraction effects contribute to the deterioration of the pseudohologram.

### 2.2.1 Propagation of the Mutual Intensity.

Consider a plane view of the system. The coordinates are denoted as one-dimensional quantities but they represent two-dimensional vectors in some cases (this is done to simplify the notation). The recording of the shadowgram is illustrated in Fig. 2.2.1. From geometrical considerations (based on similarity between triangles and proportional relationships), the projections of the mask onto the film from any point in the source plane gives a magnified version of the mask. This is illustrated in Fig. 2.2.2.

Let  $E(\alpha)$  be the monochromatic field radiated from the point source in the plane  $\alpha$  and let  $\sqrt{M(\xi)}$  be the amplitude transmittance of the mask in the plane  $\xi$  ( $M(\xi)$  being the intensity transmittance). Treating the one-dimensional drawing for simplicity, we propagate the spherical wave from the plane  $\alpha$  to the plane  $\xi$ . After multiplying by the mask function we propagate to the plane  $X$ . Using the Fresnel Kirchhoff integral and neglecting the obliquity factor we get

$$E(\xi) = \frac{i}{\lambda} \int_{-\infty}^{\infty} E(\alpha) \frac{e^{iKr(\xi,\alpha)}}{r(\xi,\alpha)} d\alpha \quad (2.2.1)$$

Behind the mask we have:

$$E^+(\xi) = E(\xi) \sqrt{M(\xi)} \quad (2.2.2)$$

We let the field at the plane  $\xi$  propagate to the plane  $X$ . Using the Fresnel Kirchhoff integral once more and substituting for  $E^+(\xi)$  and  $E(\xi)$  from (2.2.1) we get:

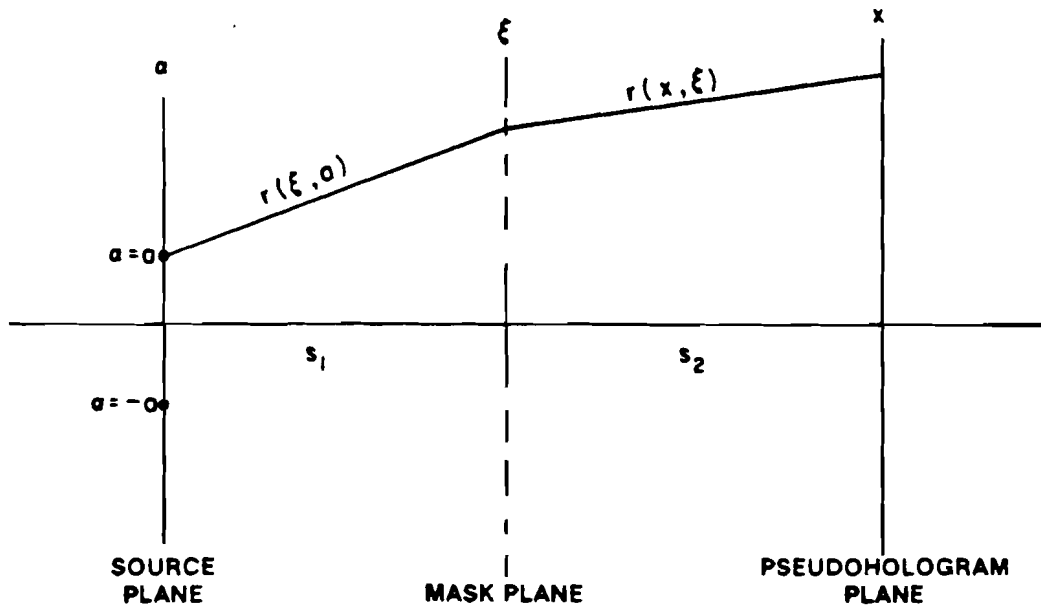


Fig. 2.2.1  
The geometry for recording a pseudohologram.

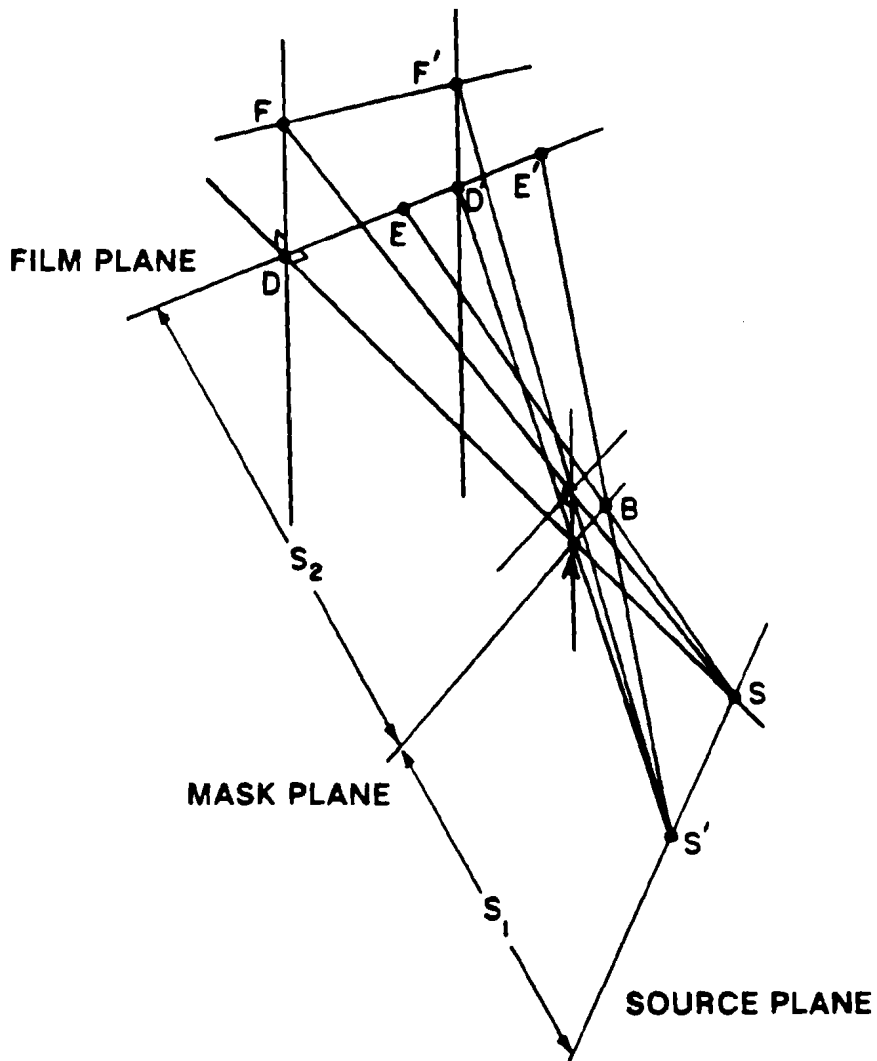


Fig. 2.2.2  
Explanation of how 2 projections from two point sources  $S$ ,  $S'$ , of the same aperture produce the same shadows.  
 $\Delta S'BA \sim \Delta S'E'D'$ ;  $\Delta SBA \sim \Delta SED$  but  $AB$  is common to both cases so  $\overline{DE} = \overline{D'E'}$ .

$$E(X) = \frac{1}{\lambda^2} \int \int E(\alpha) \sqrt{M(\xi)} \frac{e^{iK[r(\xi, \alpha) + r(\xi, X)]}}{r(\xi, \alpha) \cdot r(\xi, X)} d\alpha d\xi \quad (2.2.3)$$

Let us use the following assumptions:

- (1)  $r(\xi, \alpha)$   $r(\xi, X)$  in the denominator change slowly compared to the exponent and can be taken outside the integral, and written as  $S_1$  and  $S_2$ .
- (2) The paraxial approximation is valid and for  $r(\xi, \alpha)$  and  $r(\xi, X)$  we retain only the first order term.

We then can write (2.2.3) as:

$$E(X) = c' \int \int E(\alpha) \sqrt{M(\xi)} e^{iK \left[ \frac{\alpha^2}{2S_1} + \frac{\xi^2}{2} \left( \frac{1}{S_1} + \frac{1}{S_2} \right) - \xi \left( \frac{\alpha}{S_1} + \frac{X}{S_2} \right) \right]} d\alpha d\xi \quad (2.2.4)$$

where  $c' = [\text{phase factor}] / \lambda^2 S_1 S_2$ .

We are interested in the intensity in the plane X:

$$I(X) = \langle E(X) E^*(X) \rangle \quad (2.2.5)$$

where  $\langle \rangle$  denotes ensemble average.

(2.2.5) is a special case of the general mutual intensity function:

$$\Gamma(X_1, X_2) = \langle E(X_1) E^*(X_2) \rangle \quad (2.2.6)$$

and  $I(X) = \Gamma(X, X)$ . Substituting for  $E(X_1)$  and  $E(X_2)$  from (2.2.4) into (2.2.6) we can find the rule for the propagation of the mutual intensity in terms of its value at the source

$$\Gamma(\alpha_1, \alpha_2) = \langle E(\alpha_1) E^*(\alpha_2) \rangle \quad (2.2.7)$$

Although in general  $\Gamma(\alpha_1, \alpha_2)$  may have a finite width we will simplify the derivation by assuming:

$$\Gamma(\alpha_1, \alpha_2) = I(\alpha) \delta(\alpha_1 - \alpha_2) \quad (2.2.8)$$

This is a nonphysical assumption even for a black body source (where the width of the coherence function is of the order of the average wavelength of radiation emitted from this source) and it is used only to facilitate the calculation. Using (2.2.4) - (2.2.8) we can write the intensity as follows:

$$I(X) = c' \int I(\alpha) \left| \left[ \int \sqrt{M(\xi)} e^{iK \left[ \frac{1}{2} \left( \frac{1}{S_1} + \frac{1}{S_2} \right) \xi^2 - \xi \left( \frac{\alpha}{S_1} + \frac{X}{S_2} \right) \right]} d\xi \right]^2 \right| d\alpha \quad (2.2.9)$$

The quantity in the square brackets is the diffraction pattern of the mask from a point source  $\alpha$ . We are interested in the geometrical optics limit which is expressed as the limit

$$\lambda \rightarrow 0 \quad \text{or} \quad K \rightarrow \infty \quad (2.2.10)$$

In this case the stationary phase method (Ref. [2.2.5]) can be used to evaluate (2.2.9). The phase term is:

$$\phi(\xi) = \frac{1}{2} \mu \xi^2 - \xi \left( \frac{\alpha}{s_1} + \frac{\chi}{s_2} \right) + s_1 + s_2 + \frac{\alpha^2}{2s_1} + \frac{\chi^2}{2s_2} + \dots \quad (2.2.11)$$

where  $\mu = \left( \frac{1}{s_1} + \frac{1}{s_2} \right)$ . The term in the brackets in (2.2.9) is written

as:

$$I(K) = \int_a^b g(\xi) e^{iK\phi(\xi)} d\xi \quad (2.2.12)$$

where  $g(\xi) = \sqrt{M(\xi)}$  and  $\xi$  is a one-dimensional quantity. From Ref. [2.2.6] we may approximate (2.2.12) by

$$I(K) \sim \sqrt{\frac{2\pi}{K\phi''(\xi_0)}} g(\xi_0) e^{iK\phi(\xi_0)} e^{\pm i\frac{\pi}{4}} + \frac{1}{K} \left[ \frac{g(b)}{\phi'(b)} e^{iK\phi(b)} - \frac{g(a)}{\phi'(a)} e^{iK\phi(a)} \right] + \dots \quad (2.2.13)$$

where  $\phi'(\xi_0) = 0$ ;  $\phi''(\xi_0) \neq 0$ ;  $\phi'(a) \neq 0$ ;  $\phi'(b) \neq 0$  and where  $\phi'(\xi_0)$  and  $\phi''(\xi_0)$  are the first and second derivatives with respect to  $\xi$ , evaluated using the leading terms in the expansion for the phase (2.2.11). We take the + sign for  $\phi''(\xi_0) > 0$  and the - sign for  $\phi''(\xi_0) < 0$ .  $a$  and  $b$  are the boundaries of the aperture.

The first term in (2.2.13) describes the geometrical shadow while the second term denotes the contributions from diffraction. We will now evaluate the first term explicitly.

From  $\phi'(\xi_0) = 0$  we get

$$\xi_0 = \frac{1}{\mu} \left( \frac{a}{s_1} + \frac{x}{s_2} \right) . \quad (2.2.14)$$

Also  $\phi''(\xi_0) = \mu$ . Let us denote the one-dimensional intensity by  $I^1$  and the two-dimensional intensity by  $I^2$ . From (2.2.9), (2.2.12) and (2.2.13) we have

$$I^1(x) = \frac{c'}{\lambda\mu} \int_{-\infty}^{\infty} I^1(\alpha) M(\xi_0) d\alpha \quad (2.2.15)$$

In the two-dimensional case the constant outside the integral is  $\left(\sqrt{\frac{\lambda}{\mu}}\right)^2$  and so, substituting for  $c'$  from (2.2.4), we get

$$\begin{aligned} I^2(x) &= \frac{1}{\lambda^2} \left(\frac{2\pi}{K\mu}\right)^2 \frac{1}{(s_1 s_2)^2} \int_{-\infty}^{\infty} I^2(\alpha) M(\xi_0) d\alpha \\ &= \frac{1}{(s_1 + s_2)^2} \int_{-\infty}^{\infty} I^2(\alpha) M(\xi_0) d\alpha \end{aligned} \quad (2.2.15a)$$

This is the result used in Ref. [2.2.1] p. 33.

This result is often quoted in pseudoholography: the intensity on the film plane is given by the convolution of the source function and the mask function. However, the condition  $\lambda \rightarrow 0$  is usually true only for nuclear radiation, nuclear particles and very hard x-ray radiation. The x-rays emitted from laser produced plasmas are typically in the region  $1 - 8\text{\AA}$  and therefore diffraction effects may not be negligible. Let us now examine the second term in (2.2.13). To

simplify matters the calculation will be one-dimensional.

Consider the simple case of a slit on axis as in Fig. 2.2.3. The symmetry in this example allows us to get  $g(a) = g(-a)$  where  $a, b$  are the slit boundaries. Also, from (2.2.11) we get:

$$\begin{aligned}\phi(a) &= s_1 + s_2 + \frac{\mu a^2}{2} - a\left(\frac{\alpha}{s_1} + \frac{\chi}{s_2}\right) + \frac{\alpha^2}{2 \cdot s_1} + \frac{\chi^2}{2 \cdot s_2} \\ \phi(-a) &= s_1 + s_2 + \frac{\mu a^2}{2} + a\left(\frac{\alpha}{s_1} + \frac{\chi}{s_2}\right) + \frac{\alpha^2}{2 \cdot s_1} + \frac{\chi^2}{2 \cdot s_2}\end{aligned}\tag{2.2.17}$$

$$\phi'(a) = \mu a - \left(\frac{\alpha}{s_1} + \frac{\chi}{s_2}\right)$$

$$\phi'(-a) = -\mu a - \left(\frac{\alpha}{s_1} + \frac{\chi}{s_2}\right)$$

Using the above approximation the second term in (2.2.13) can be written as:

$$\frac{1}{K} \frac{g(a)}{\phi'(a)} e^{iK\phi(a)} \cdot \left\{ 1 - \frac{\phi'(a)}{\phi'(-a)} e^{iK[\phi(-a) - \phi(a)]} \right\}\tag{2.2.18}$$

where  $g(\xi) = \sqrt{M(\xi)}$  and the factor  $1/(r(\xi, x) r(\xi, a))$  was taken outside the integral as before. Since  $\phi'(a) \neq 0$  and  $\phi'(-a) \neq 0$ , (2.2.18) does not hold at the boundary of the geometrical shadow.

Assuming  $\alpha = 0$  for simplicity and using (2.2.17) we get

$$\phi(-a) - \phi(a) = \frac{2aX}{S_2} \tag{2.2.19}$$

$$\frac{\phi'(a)}{\phi'(-a)} = \frac{\frac{X}{S_2} - \mu a}{\frac{X}{S_2} + \mu a} \equiv B(X)$$

Let us divide the discussion into the two regions in Fig. 2.2.3.

Region I is the geometrical shadow region and region II is the illuminated region.

In region II,  $\frac{\phi'(a)}{\phi'(-a)} \ll 1$  near the boundary. We thus can neglect this term. From (2.2.13) and (2.2.18) using the fact that  $g(a) - g(\xi_0)$  near the boundary and that  $\phi''(\xi_0) = \mu$ , we have in region II

$$I(K) - g(\xi_0) \sqrt{\frac{2\pi}{K\mu}} e^{iK\phi(\xi_0)} \left\{ 1 + \frac{1}{\sqrt{\frac{2\pi}{K\mu}} K(a\mu - \frac{X}{S_2})} e^{iK[\phi(a) - \phi(\xi_0)]} \right\} \tag{2.2.20}$$

Using (2.2.17),  $\alpha = 0$ . Substituting for  $\xi_0$  from (2.2.14) and denoting

$$\frac{R(X)}{\sqrt{K}} = \frac{1}{\sqrt{\frac{2\pi}{K\mu}} K(a\mu - \frac{X}{S_2})}, \text{ the intensity in region II near the boundary}$$

can be written from (2.2.9) as

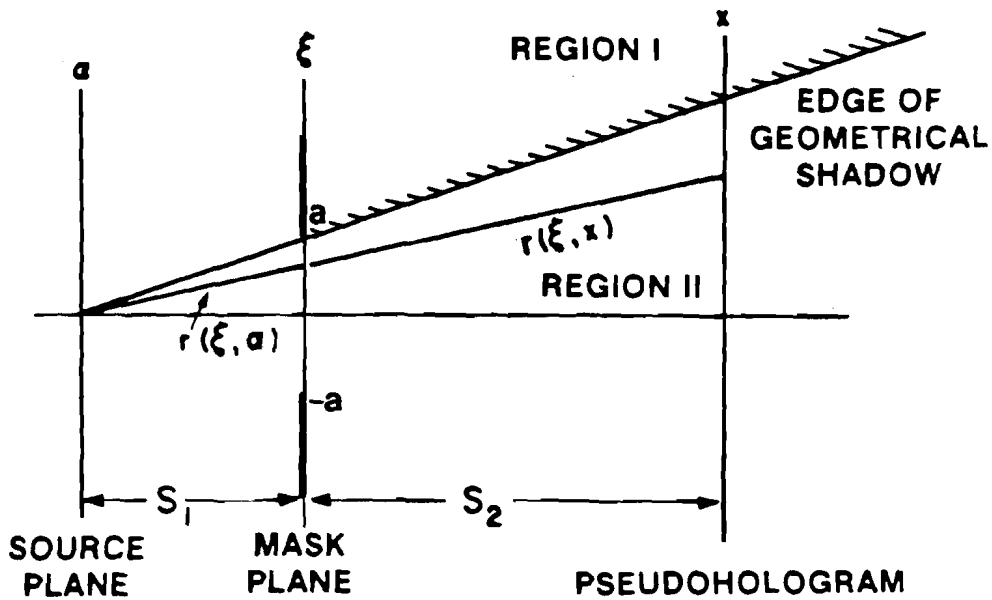


Fig. 2.2.3

Notation for stationary phase calculation of the diffraction pattern from a slit.

$$r(\xi, a) = [(\xi - a)^2 + S_1^2]^{1/2}; \quad r(\xi, x) = [(\xi - x)^2 + S_2^2]^{1/2}$$

In a typical experiment:

$$\text{Max } \{a\} < 10^{-2} \text{ cm}; \quad \text{Max } \{a\} < 5 \times 10^{-4} \text{ cm}; \quad S_1 \sim 1 \text{ cm}; \\ S_2 \sim 16 \text{ cm}.$$

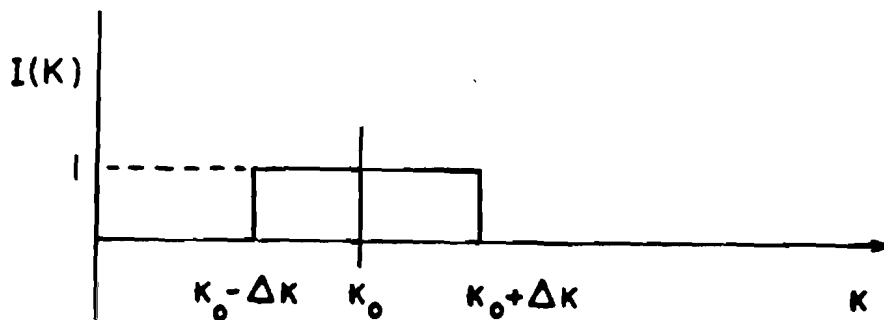


Fig. 2.2.4

An approximation for the spectrum of x-rays emitted from laser produced plasma.  $K$  = wave number,  $I(K)$  = normalized intensity distribution.

$$I(X) = c' (I(K) I^*(K)) \quad (2.2.21)$$

$$= c'' \left\{ 1 + \frac{R^2(X)}{K} + \frac{2R(X)}{\sqrt{K}} \cos \left[ K \left( \frac{\mu a^2}{2} + \frac{X^2}{2\mu S_2^2} + \frac{aX}{S_2} \right) \right] \right\}$$

where  $c'$ ,  $c''$  are constants independent of  $K$ .

In region I the first order of (2.2.13) vanishes identically and we are left with the second order terms in (2.2.18). We then have:

$$I(X) = \frac{c'''}{K} \left[ 1 + B^2(X) + 2B(X) \cos \left( \frac{2KaX}{S_2} \right) \right] \quad (2.2.22)$$

The constants and the power of  $K$  used in (2.2.21) and in (2.2.22) are for the two-dimensional case although the expression (2.2.20) is for the one-dimensional case. This is a simplification that will give us some indication of the real case.

Until now only monochromatic light was assumed. In a real plasma the spectrum is very complicated and contains characteristic lines as well as a continuous spectrum. Again, to simplify we assume a spectral distribution as shown in Fig. 2.2.4. Expressions (2.2.21) and (2.2.22) must be integrated over the range  $[K_0 - K, K_0 + K]$ . The terms involving Cos function are difficult to integrate and to

put in closed form. While they can be written as an infinite series, they are difficult to visualize. However, from (2.2.21) and (2.2.22) we see that integrating the cos function will tend to smooth out the fluctuations so that the shadow will be smoother than the typical Fresnel diffraction pattern of a slit (as in Ref. [2.2.7] for example). Hence the shadows cast by a broadband source will approximate the mask more faithfully than those cases with monochromatic radiation.

The expressions (2.2.21) and (2.2.22) could be computed numerically. The results would give us the shape of the recorded zones and, by Fourier Transform, the efficiency at higher orders could be calculated. We might then determine which configuration would still give an appreciable efficiency at higher orders.

A second method would be to numerically propagate a spherical wave through the mask to a film plane and to compute the intensity transmittance. We would then numerically reconstruct the pseudohologram with an incident plane wave and compute the intensities at all orders. We could thus determine the configuration with which higher orders are still useful. However, as will be explained later, this is a very difficult calculation because we need to perform operations with vectors with much more than 30,000 elements. To simulate the experimental conditions we would need to simulate polychromatic radiation in the calculation. This means repeating the above procedure for different wavelengths. These procedures must be employed if an accurate criterion is needed for closing the width of the outermost zone in a given pseudoholographic configuration.

Instead, we may develop a rough rule of thumb for determining the

maximum wavelength which is useful in a given setup. From the geometry illustrated in Fig. 2.2.5 we may define a quantity  $\Delta v$ ,

$$\Delta v = r \left[ \frac{2\mu}{\lambda} \right]^{\frac{1}{2}} \quad (2.2.23)$$

where  $\mu = \frac{1}{S_1} + \frac{1}{S_2}$  and  $r$  is the slit width. From Ref. [2.2.7] p. 194

$(\Delta v)^2 = 14$  is an acceptable criterion to avoid diffraction so that

when  $\mu = \frac{1}{S_1} + \frac{1}{S_2} \approx 1 \text{ cm}^{-1}$  we get from (2.2.23)

$$\lambda \leq \frac{r^2}{7} \text{ \AA} \quad (2.2.24)$$

where  $r$  is in  $\mu\text{m}$ . The criterion (2.2.24) is more stringent for reconstruction at higher orders than in the first order. For each order  $p$ ,  $\Delta v$  must be chosen so that the reconstructed intensity at this order will be appreciably larger than the noise. For third order reconstructions  $(\Delta v)^2 = 16$  seems to be acceptable by considering Ref. [2.2.7] p. 194, and so we require  $\lambda \leq \frac{r^2}{8} \text{ \AA}$  for third order reconstruction.

### 2.2.2 High Order Reconstruction of a Pseudohologram.

Using the zone plate in the coded aperture mode in first order reconstruction gives a resolution comparable to that of the pinhole camera, where the pinhole diameter is approximately equal to the width of the outermost zone. It has been shown (see Ref. [2.2.14]) that for simple objects, there is a net gain in signal to noise ratio in the zone plate coded aperture mode. However, this gain is not critical for imaging laser produced plasmas because the x-ray intensity is so great that it does not represent an exposure limita-

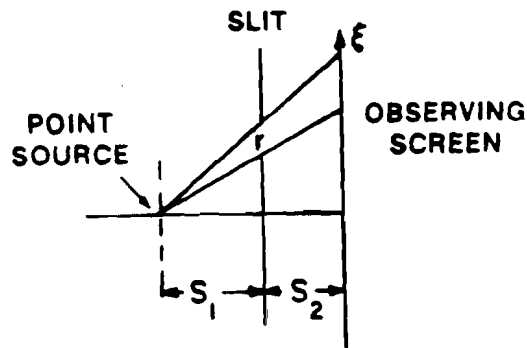


Fig. 2.2.5  
Notation for Fresnel propagation calculation  
through a slit of width  $r$ .

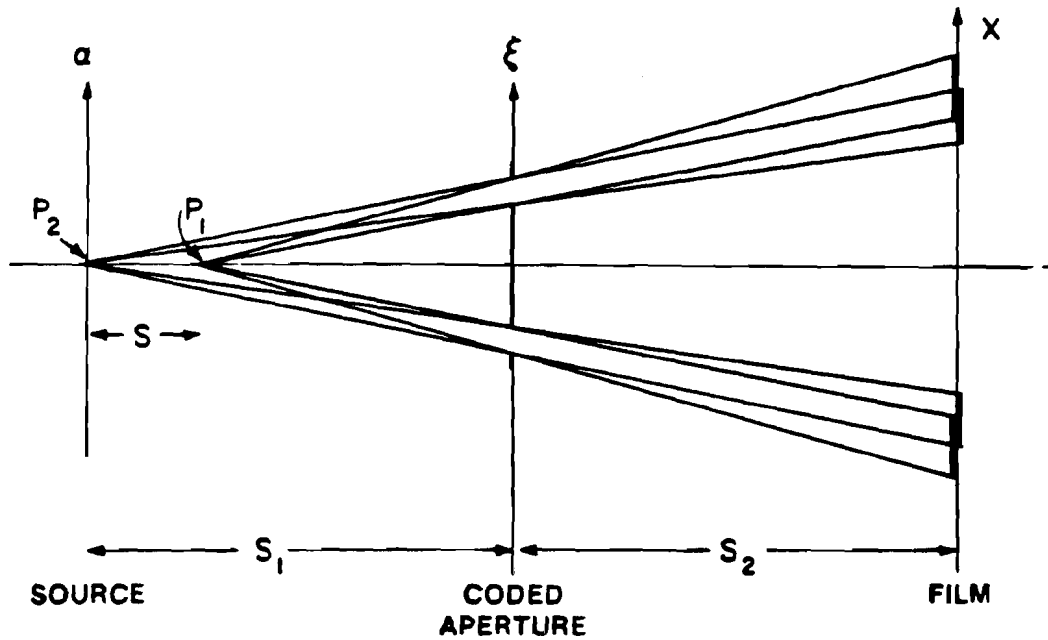


Fig. 2.2.6  
Illustration of recording depth information with a coded aperture.  
 $I(a, s)$  = intensity source distribution  
 $M(\xi)$  = mask function at  
 $I(x)$  = intensity distribution in the film plane in no. photons/area  
A point closer to the coded aperture ( $P_1$ ) forms a larger shadow than that from  $P_2$ .

tion in the pinhole camera. Furthermore, as will be discussed later, this net gain in pseudoholography decreases as the number of resolvable elements increases. There is a limited usefulness to the tomographic capability of pseudoholography. Finally, it is a two-step process. It thus seems that in view of the simplicity of the pinhole camera there is no point in using pseudoholography. However, we find that a strong justification for using this technique is the possibility of achieving a resolution in higher order reconstructions which is not achievable with other techniques such as the pinhole camera, zone plate imaging, or the x-ray microscope. To display this important advantage it is, therefore, necessary to rederive all the quantities previously given in Ref. [2.2.1] for first order reconstructions. This will enable us to calculate the efficiencies and the effects of noise at higher orders.

Consider the system in Fig. 2.2.6. In a real situation the problem of recording a pseudohologram is a three-dimensional problem since depth information is registered, too. To simplify the treatment, we assume a plane source. From Eq. (2.2.9) we have for the intensity at the recording film plane (here the coordinates  $\alpha, \xi$  and  $X$  are symbolically two-dimensional)

$$I(X) = c \int_{-\infty}^{\infty} I(\alpha) G(\alpha + dX) d\alpha \quad (2.2.25)$$

where

$$G(\alpha + dX) = \left| e^{-i\left(\frac{h}{\mu}\right)^2} \int \sqrt{M(\xi)} e^{iK\left(\xi + \frac{h}{\mu}\right)^2} d\xi \right|^2 \quad (2.2.26)$$

$$h = S_1 + \frac{S_1}{S_2} X \quad \text{and} \quad d = \frac{S_1}{S_2} .$$

In the case  $\lambda \rightarrow 0$ , (2.2.26) is given by:

$$G(\alpha + dX) = M(\alpha + dX) \quad (2.2.27)$$

$M(\xi)$  is the intensity transmittance of the zone plate mask. In the  $\xi^2$  domain it is a periodic function, and therefore  $G(\xi^2)$  is a periodic function. We can therefore use a Fourier series to express this function. Let  $\xi$  be a normalized coordinate (i.e.  $\xi = \xi'/\xi_1$  where  $\xi'$  is the unnormalized coordinate and  $\xi_1$  is the radius of the innermost zone); we can write:

$$M(\xi^2) = \sum_{p=-\infty}^{\infty} C_p e^{-ip\pi\xi^2} \cdot \text{Circ}[\xi; \xi_N] \quad (2.2.28)$$

Let  $\theta = \xi^2$ ; then

$$C_p = \int_0^{2\pi} G(\theta) e^{ip\pi\theta} d\theta \quad (2.2.29)$$

These are the same integrals we dealt with in section 2.1, and examples are given in Table 2.1.1, and Fig. 2.1.4. We now substitute (2.2.28) in (2.2.25) using (2.2.15a) to get (for two-dimensional coordinates)

$$I(X) = \int_{-\infty}^{\infty} I(\alpha) \sum_{p=-\infty}^{\infty} C_p e^{-i\pi p \left[ \frac{1}{\mu} \left( \frac{\alpha}{S_1} + \frac{X}{S_2} \right) \right]^2} d\alpha \quad (2.2.30)$$

$$\text{Circ} \left\{ \left[ \frac{1}{\mu} \left( \frac{\alpha}{S_1} + \frac{X}{S_2} \right) \right]; \xi_N \right\}$$

where  $\xi_1$  is the radius of the innermost zone,  $\mu = \frac{1}{S_1} + \frac{1}{S_2}$ ,

$\text{Circ} \left\{ \left[ \frac{1}{\mu} \left( \frac{\alpha}{S_1} + \frac{X}{S_2} \right) \right]; \xi_N \right\}$  is a circle of radius  $\xi_N$ , and the coordinate

is  $\xi = \frac{1}{\mu} \left( \frac{\alpha}{S_1} + \frac{X}{S_2} \right)$  and  $N$  is the number of zones.  $I(X)$  of (2.2.30) is

recorded on the film and processed with a certain  $\gamma$ . (The slope of H&D curve, see Ref. [2.2.9].) The amplitude transmittance of the pseudohologram is therefore

$$T = \tau_0 I(X)^{-\gamma/2} \quad (2.2.31)$$

The reconstructed field is given by the Fresnel integral where (2.2.31) is the input function. Let  $X_r$  be in the reconstruction plane; then:

$$E(X_r) = \frac{e^{iKZ}}{i\lambda Z} \int_{-\infty}^{\infty} \left\{ \sum_{p=-\infty}^{\infty} C_p \int_{-\infty}^{\infty} I(\alpha) e^{-i\pi p \left( \frac{\xi_0}{\xi} \right)^2} \text{Circ}[\xi_0; \xi_N] d\alpha \right\}^{-\gamma/2} e^{\frac{iK}{2Z} (X_r - X)^2} dX \quad (2.2.32)$$

Only the case  $\gamma = -2$  will be considered here. For all the other cases

$\gamma = -2 + d$  and the expression in the large brackets in (2.2.32) can be written as a product of

$$\left[ \sum_p c_p \int \dots d\alpha \right]^{-\gamma/2} \cdot \left[ \sum_p c_p \int \dots d\alpha \right]^{-d/2}$$

Since the Fresnel transformation of products is equal to the convolution of the transforms, Eq. (2.2.32) will be written in the general case as a convolution. Rearranging (2.2.32) we can see that the terms containing  $X^2$  will vanish if  $Z$  has the following form:

$$Z_p = \frac{1}{p} \frac{\xi_1^2}{\lambda} \left( \frac{S_1 + S_2}{S_1} \right)^2 \quad (2.2.33)$$

These are the locations of the  $p$ th order images. From (2.2.32) and (2.2.33) after algebraic manipulations we get

$$E(X_r) = \sum_{p=-\infty}^{\infty} c_p \frac{e^{iKZ}}{i\lambda Z_p} \int_{-\infty}^{\infty} d\alpha l(\alpha) e^{-\frac{i\pi}{\lambda Z_p} \left[ -X_r^2 + \left( \frac{S_2}{S_1} \alpha \right)^2 \right]}$$

$$\int_{-\infty}^{\infty} \text{circ} \left[ \frac{1}{\mu} \left( \frac{\alpha}{S_1} + \frac{X}{S_2} \right); \xi_N \right] \cdot e^{-\frac{2\pi i}{\lambda Z} \left( X_r + \frac{S_2}{S_1} \alpha \right) X} dx$$

(2.2.34)

changing-variables to  $t = \frac{1}{\mu} \left( \frac{\alpha}{S_1} + \frac{X}{S_2} \right)$  the integration over  $X$  is recognised

as the Bessel function of order 1. Denoting the integral over  $X$  by  $h(\alpha; X_r; p)$  we can thus write:

$$h(\alpha, X_r, p) = 2\pi e^{\frac{i\pi}{\lambda Z_p} \left( X_r + \frac{S_2}{S_1} \alpha \right)^2} \frac{\int_1 \left[ \frac{S_2^{\mu \cdot 2\pi} \epsilon_N}{\lambda Z_p} \left( X_r + \frac{S_2}{S_1} \alpha \right) \right]}{\frac{2\pi S_2^{\mu}}{\lambda Z_p} \left( X_r + \frac{S_2}{S_1} \alpha \right)} \quad (2.2.35)$$

(2.2.34) can then be written as:

$$E(X_r) = \sum_{p=-\infty}^{\infty} \frac{C_p e^{iKZ_p}}{\lambda Z_p} \int_{-\infty}^{\infty} d\alpha l(\alpha) \cdot h(\alpha, X_r, p) \quad (2.2.36)$$

But  $Z_p = Z_1/p$ ; therefore, from (2.2.35) we get the important result for the point spread function  $h(\alpha, X_r, p)$  that it becomes narrower at larger values of  $p$ . (i.e. at higher orders).

It is important to note that the present discussion is useful only if the contributions from other foci can be neglected when we deal with a specific focus. Because the field is an infinite sum as is seen in (2.2.34), the expression for the point spread function in Eq. (2.2.35) is only an approximation. In a different derivation (see Ref. [2.1.18]) an expression is derived from which it is clear that the point spread function is not a Bessel function. Only in the limit  $N \rightarrow \infty$  can we replace it by a Bessel function (or sinc function in case of a one-dimensional zone plate). In our experiment  $N \sim 40$  and so this approximation is quite good.

### 2.2.3 Transverse and Axial Widths of the Point Spread Function.

It is sometimes required to demagnify the pseudohologram before reconstruction to get a convenient focal length. Let  $\frac{1}{m}$  be the demagnification in Eq. (2.2.30).  $I(X)$  changes to  $I(mX)$ ; this will change  $Z_p$  to  $Z(p, m) = \frac{Z_p}{m}$ . The new expression for the point spread function including demagnification is therefore

$$h(\alpha, X_r, p, m) = \quad (2.2.37)$$

$$2\pi e \frac{i\pi \cdot pm^2}{Z_1} \left( X_r + \frac{S_2}{S_1} \alpha \right)^2 \frac{J_1 \left[ \frac{2\pi pm^2 \mu S_2}{\lambda Z_1} \left( \frac{X_r}{m} + \frac{S_2}{S_1} \alpha \right) \xi_N \right]}{\frac{2\pi pm^2 \mu S_2}{\lambda Z_1} \left( \frac{X_r}{m} + \frac{S_2}{S_1} \alpha \right)}$$

Using the fact that the first zero of the Bessel function is at an argument of 3.817 we get:

$$\Delta X_r = \frac{3.817}{2\pi} \frac{\lambda Z_1}{S_2} \frac{1}{pm} \frac{1}{\xi_N} \quad (2.2.37a)$$

for the transverse width when  $\alpha=0$ .

For the axial width we assume  $I(\alpha)=I_0\delta(\alpha)$  and  $X_r=0$  so that (2.2.32) can be rewritten as:

$$I = \left| I_0 \int e^{-ip\pi \left( \frac{x}{\mu \xi_1 s_2} \right)^2} \text{Circ} \left[ \left( \frac{x}{\mu s_2} \right)^2; \xi_N^2 \right] e^{\frac{iKx^2}{2Z}} dx \right|^2$$

$$= \left| I_0 \int \text{Circ}[t; \xi_N^2] e^{-2\pi i t u} dt \right|^2$$

(2.2.38)

where  $u = \frac{p}{(\xi_1 \mu s_2)^2} + \frac{1}{\lambda Z}$  and  $t = x^2 + y^2$ . In this expression  $\bar{x} = (x, y)$  is a two-dimensional quantity. From (2.2.38) we have:

$$|I| = \left| \frac{\sin(\pi u \xi_N^2)}{\pi u} \right|^2$$

(2.2.39)

The foci are again at  $u=0$  or  $Z=Z_p$ . Also  $u = \frac{1}{\lambda} \left( \frac{1}{Z_p} - \frac{1}{Z} \right)$  so that near the focus  $\frac{1}{Z_p} - \frac{1}{Z} = \frac{\Delta Z}{Z_p^2}$ . Hence  $u = \frac{\Delta Z}{\lambda Z_p^2}$  and (2.2.39) can be written as:

$$|I| = \left| \frac{\sin \left[ \frac{\pi}{\lambda} \left( \frac{\xi_N}{Z_p} \right)^2 \Delta Z \right]}{\frac{\pi}{\lambda} \frac{\Delta Z}{Z_p^2}} \right|^2$$

(2.2.40)

The depth of focus is found using the quarter wave criterion. From (2.2.40)  $\frac{\pi}{\lambda} \left( \frac{\xi_N}{Z_p} \right)^2 \Delta Z = \frac{\pi}{2}$  hence

$$\Delta Z_p = \frac{\lambda}{2} \left( \frac{Z_p}{\xi_N} \right)^2$$

(2.2.41)

If demagnification is introduced then (2.2.30) changes from  $I(X)$  to  $I(mX)$ . Eq. (2.2.38) will change also yielding a new expression for  $u$ :

$$u = \frac{1}{\lambda} \left[ \frac{pm^2\lambda}{(\xi_1\mu s_2)^2} - \frac{1}{Z} \right] \quad (2.2.42)$$

and finally:

$$\Delta Z(p,m) = \frac{\lambda}{2} \left[ \frac{Zp}{m} \frac{1}{\xi_N} \right]^2 = \frac{\Delta Z p}{m^2} = \frac{\Delta Z}{p^2 m^2} \quad (2.2.43)$$

Let  $\xi_N$  be the radius of the outermost zone;  $r$  the width of the outermost zone,  $N$  the number of zones,  $\xi_1$  the radius of the innermost zone, and  $Z_1$  the primary focal length. We know

$$\xi_N = \sqrt{N} \xi_1 = \sqrt{NZ_1\lambda}$$

$$\xi_N = 2Nr \quad \text{for } N > 10 \quad (2.2.44)$$

$$Z_1 = \frac{\xi_1^2}{\lambda}$$

Using (2.2.44), (2.2.33) and (2.2.43) we obtain the widths of the points spread function:

$$\Delta X_r = 1.22r \left( \frac{s_1 + s_2}{s_1} \right) \frac{1}{pm} \quad (2.2.45)$$

$$\Delta Z = 0.5 \xi_1^2 \left( \frac{s_1 + s_2}{s_1} \right)^2 \cdot \frac{1}{p^2 m^2 N \lambda} \quad (2.2.46)$$

#### 2.2.4 The Transverse Resolution in the Zone Plate Pseudoholographic Technique.

In the first step of the coded pseudoholography technique, which

is illustrated in Fig. 2.2.7, every luminous point in the source (i.e., in the plasma), casts a shadow of a Fresnel zone plate onto a piece of photographic film. In the second step, which is illustrated in Fig. 2.2.8, the exposure is processed, conveniently reduced, and illuminated by a coherent beam of light. A reconstructed image is produced at a series of foci,  $F_p$ .

In order to derive an expression for the definition of the two-step pseudoholographic process, consider the system described in Figs. 2.2.7 and 2.2.8. Let  $T = \overline{AB}$  be the finest resolved element in the object,  $S_1$  the distance from the object to the mask, which is a Fresnel zone plate, and  $S_2$  the distance from the mask to the film.

In the first step the shadow of the zone plate is cast on the film by each point source, and hence produces two zone plates separated by the distance  $T' = \overline{A'B'}$  on the pseudohologram. When the processed pseudohologram is reduced to yield a convenient focal length, the separation is  $T''$ , as shown in Fig. 2.2.9. In the second step each zone plate focuses the reconstruction beam to a series of foci. If we choose  $T''$  to be such as to cause the corresponding reconstructed point sources to be resolved according to the Sparrow criterion, we have from Ref. [2.2.10] that

$$T'' = 1.46\lambda(1/\Omega) \quad (2.2.47)$$

where  $\lambda$  is the wavelength of the reconstruction beam and  $\Omega$  is the cone angle of the focussed beam at the primary focus. Let us denote by  $\xi_N$  and  $r$  the radius and the width of the outermost zone, respectively, of the original zone plate. We will denote by  $\xi'_N$  and  $r'$  the corresponding

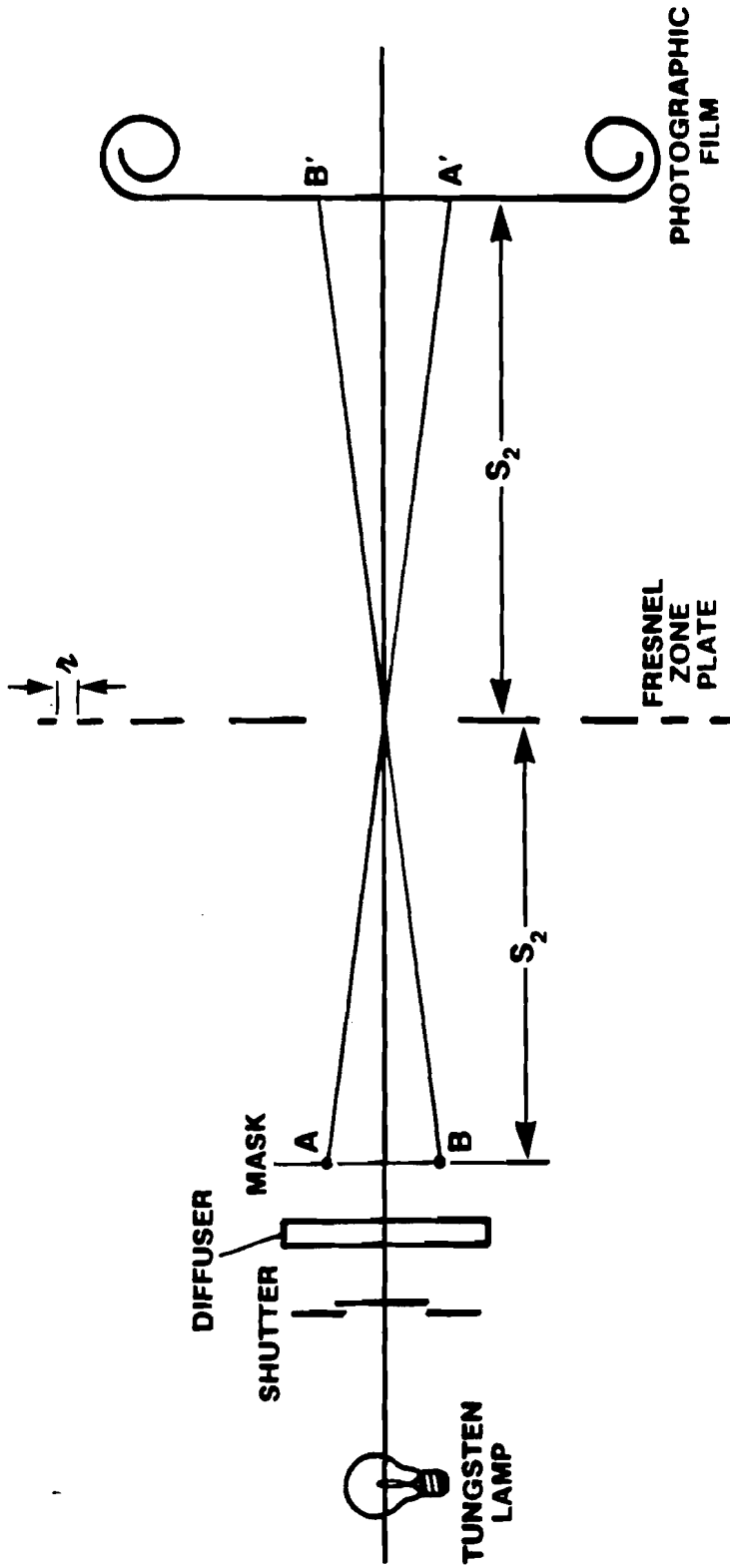


**Fig. 2.2.7**  
The recording step of the pseudoholographic technique.  $r$  is the outermost zone.  $A'$ ,  $B'$  are centers of two zone plate shadows.

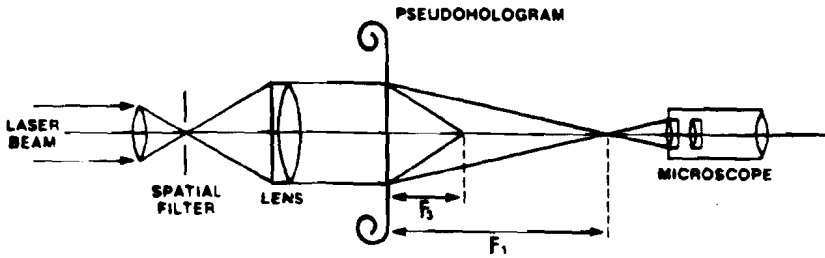


Figure 2.2.8  
The reconstruction of a pseudohologram.  $F_1$  and  $F_3$  are the first and third order foci respectively.

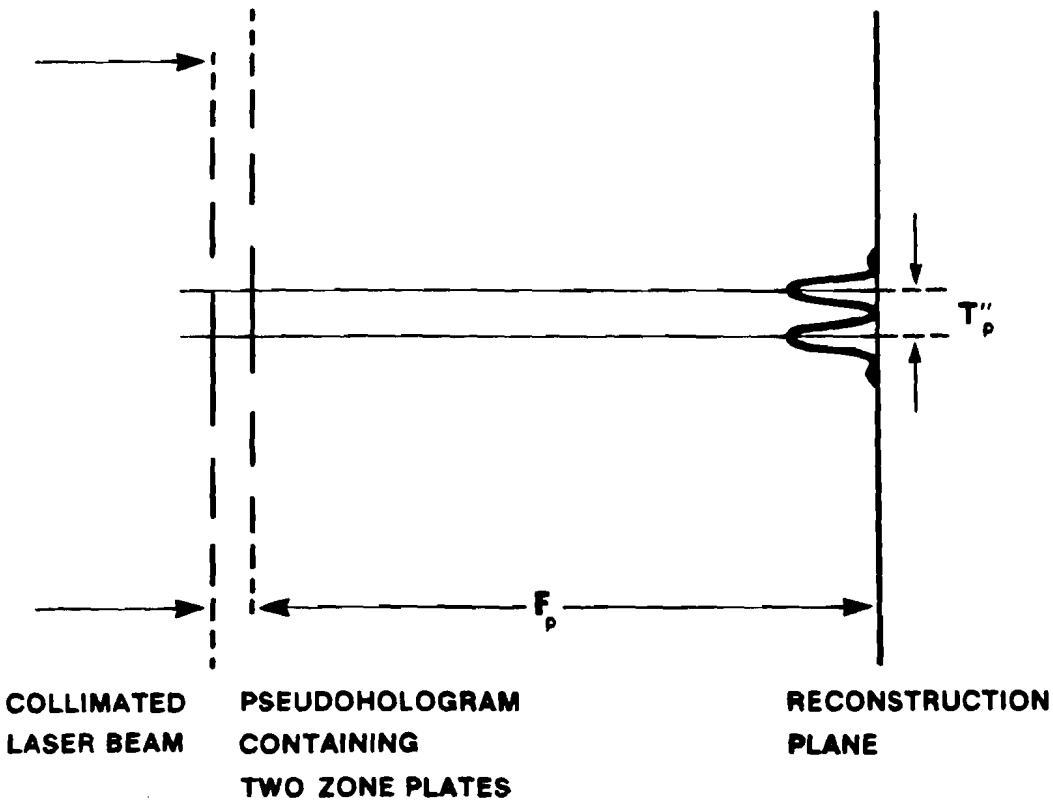


Figure 2.2.9  
Explanation of the reconstruction step. Each zone plate recorded on the pseudohologram focuses the light at its own focal point.

quantities on the recorded pseudohologram, and by  $\xi_N''$  and  $r''$  those on the reduced pseudohologram. From (2.2.44) we have:

$$\xi_N = 2rN \quad (2.2.48)$$

Also, from geometrical considerations it can be shown that

$$\xi_N' = \xi_N \frac{(S_2 + S_1)}{S_1} \quad (2.2.49)$$

Denoting the demagnification by  $1/m$ , then

$$\xi_N'' = \xi_N' / m \quad (2.2.50a)$$

$$T'' = T' / m \quad (2.2.50b)$$

From Figs. 2.2.7 and 2.2.9 and from Eq. (2.2.50) we get

$$T'' = T \left( \frac{S_1}{S_2} \right) \left( \frac{1}{m} \right) \quad (2.2.51)$$

Since for zone plates employed as a lens in the visible  $\xi_N'' = \sqrt{NF}$ , then  $F = \xi_N''^2 / N\lambda$  and, therefore,

$$1/\alpha = \frac{F}{2\xi_N''} = \xi_N'' / 2N\lambda \quad (2.2.52)$$

From Eqs. (2.2.47) - (2.2.52) we get

$$T = 1.46\lambda(1/\Omega) \cdot \frac{S_1}{S_2} m = 1.46r \left( \frac{S_1 + S_2}{S_2} \right) \quad (2.2.53)$$

From (2.2.53) we see that the demagnification,  $1/m$ , has no effect on the transverse resolution.

Now consider the reconstruction at higher order foci. At the  $p$ th order focus,

$$F_p = (\xi_N''^2 / N) \frac{1}{p} \quad (2.2.54)$$

Hence

$$(1/\Omega)_p = \xi_N'' / 2pN \quad (2.2.55)$$

But the distance between the reconstructed points  $T''$ , remains the same; only the cone angle of the reconstructed beam gets bigger. Therefore, the only quantity in (2.2.47) that changes is  $1/\Omega$ , Hence:

$$T_p = \frac{1.46r}{p} \cdot \frac{S_1 + S_2}{S_2} \quad (2.2.56)$$

This remarkable result means that by going to higher orders the definition improves significantly. The geometry can be arranged so that  $S_2 \gg S_1$ , and so with a practical value for  $r$  of about  $3\mu\text{m}$  we get:

$$T_1 = 1.46 \cdot 3 = 4.38\mu\text{m}$$

$$T_2 = \frac{1.46 \cdot 3}{3} = 1.46\mu\text{m}$$

$$T_3 = 1.46 \cdot \frac{3}{5} = 0.87\mu\text{m}$$

### 2.2.5 Tomographic Resolution in the Zone Plate Pseudoholographic Technique.

From Fig. 2.2.10 we obtain the following relationships:

$$\Delta\xi_N = \frac{S_1}{S_2} S \quad (2.2.57a)$$

$$S = L \operatorname{tg}\theta \quad (2.2.57b)$$

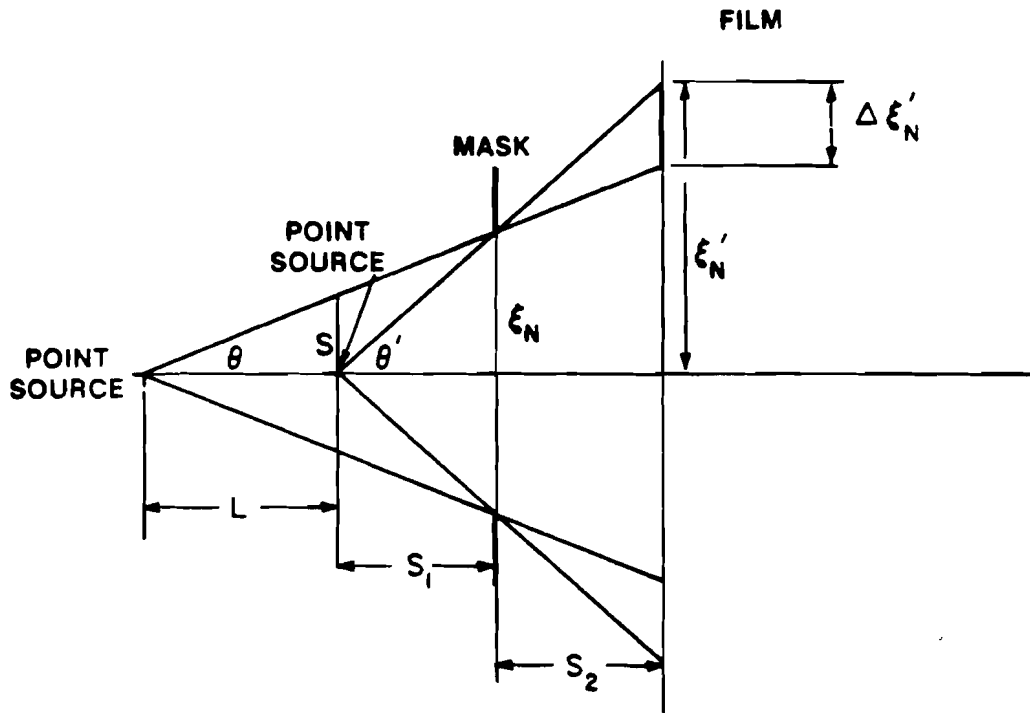


Fig. 2.2.10  
Derivation of the tomographic resolution of the pseudoholographic technique.

$$\operatorname{tg} \theta = \xi_N / (S_1 + L) \sim \xi_N / S_1 \quad (2.2.57c)$$

For zone plates:  $F_p = F/p = \xi_1'^2 / p\lambda = \xi_1'^2 / m^2 p\lambda \quad (2.2.57d)$

Therefore  $\Delta F_p = \frac{\Delta F}{p} = \frac{2\xi_1' \Delta\xi_1'}{m^2 p\lambda} \quad (2.2.57e)$

From Eq. (2.2.46)  $\Delta F_p = \frac{0.5}{p^2 m^2 N\lambda} \xi_1'^2 \left( \frac{S_1 + S_2}{S_1} \right)^2 \quad (2.2.57f)$

From Fig. 2.2.10  $\xi_1' = \frac{S_1 + S_2}{S_1} \xi_1 \quad (2.2.57g)$

By equating (2.2.57e) and (2.2.57f) and from (2.2.48) we get:

$$L = \frac{0.5}{Np} \frac{S_1}{S_2} (S_1 + S_2) \quad (2.2.58)$$

The tomographic resolution increases with the number of zones and with the order number.

### 2.2.6 Efficiency of Reconstructions at Higher Orders.

From Eq. (2.2.34) and (2.2.15a) the factor that determines the efficiency at the different orders is

$$\frac{C_p}{\lambda Z_p} = \frac{1}{(S_1 + S_2)^2 \lambda Z_p} \int_0^{2\pi} M(\theta) e^{i\pi p \theta} d\theta \quad (2.2.59)$$

We have already seen a few examples for  $M(\theta)$  in the previous section in Fig. 2.1.4. For the case of Fig. 2.1.4a  $C_p = \bar{B}_a(u) = \frac{\sin \pi u q}{\pi u}$ .

Substituting for  $\pi u q = \frac{\pi}{2} (2p + 1)$  we get

$$\frac{C_p}{\lambda Z_p} = \frac{1}{(s_1 + s_2)^2 \lambda Z_p} \frac{(-1)^{p+1}}{[(2p+1)/2q]}$$

But  $Z_p = \frac{z_1}{(2p+1)}$  so that

$$\frac{C_p}{\lambda Z_p} = \frac{1}{(s_1 + s_2)^2} \frac{2q}{z_1} \text{ independent of } p! \quad (2.2.60)$$

Hence the efficiencies are equal in all orders in this case. However, as has been shown in section 2.1.8, the flux at higher orders goes as  $1/p^2$ .

The efficiency in higher orders is very sensitive to changes in the zone shape. In Fig. 2.1.4 there are examples where the efficiency at various order is not given by Eq. (2.2.60).

### 2.2.7 The Effects of Zone Width on the Effective Dynamic Range.

In Fig. 2.2.11 the effect of narrowing the zones is demonstrated. In Fig. 2.2.11 A and B, cosinusoidal zones allow only for a small number of zone systems to be recorded before the film is completely darkened. In Fig. 2.2.11 C and D narrow zones allow for a much larger number of zone systems to be recorded. Hence by narrowing the zones the effective dynamic range (or the number of point sources which can be recorded) increases. In order to be more quantitative it is useful to define a quantity  $C$ , the contrast, which is the standard deviation of the intensity fluctuations on the recording divided by the average intensity. Also it is useful to compare  $C_{coh}$  for a usual hologram made with a reference beam

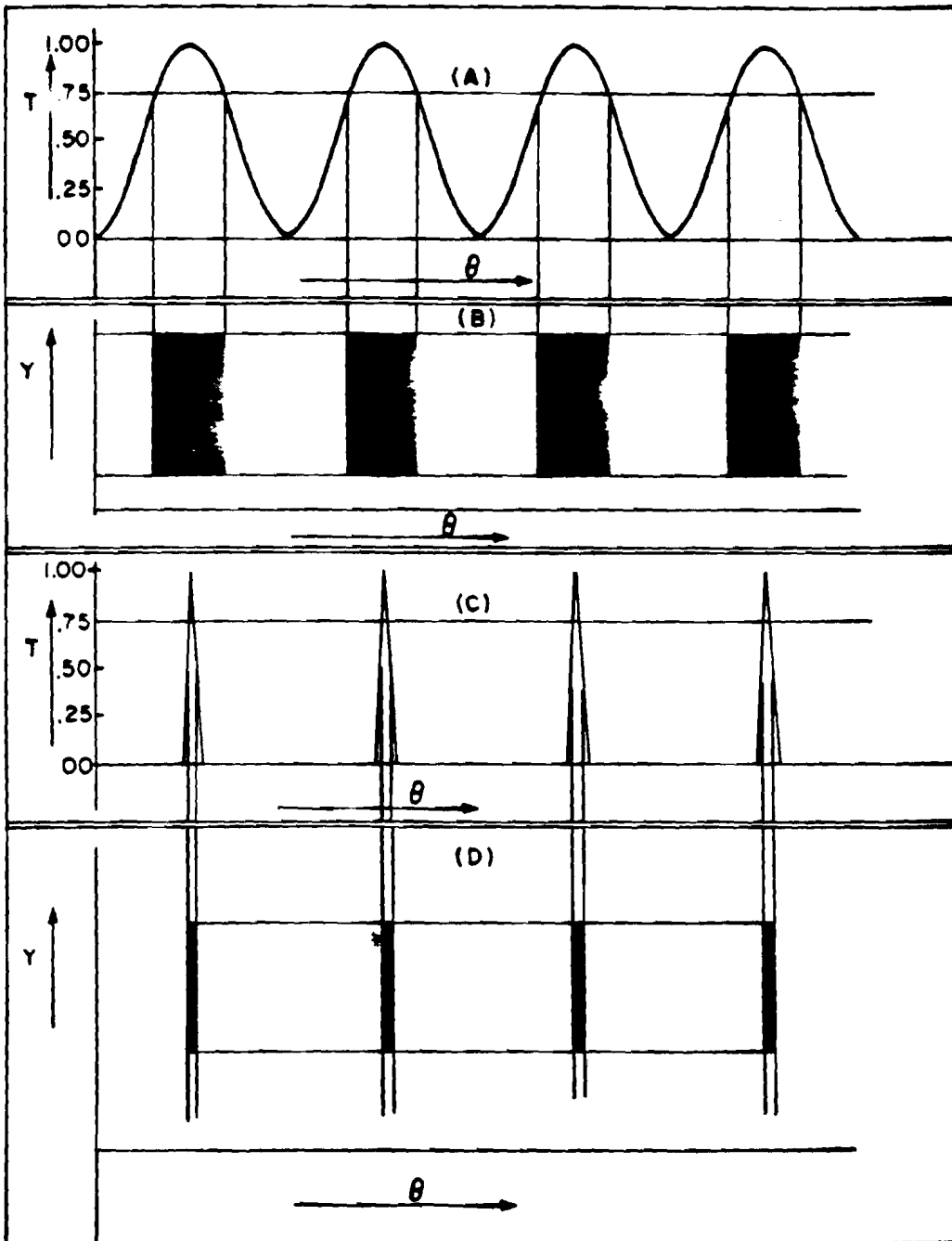


Fig. 2.2.11  
(A)  $\cos^2\theta$  fringes,  $\theta$  = quadratic distance coordinates,  $T$  = transmission, (B)  $Y$  = distance perpendicular to the 1-D zone plate; black stripes on a high contrast processed film, (C) narrow fringes, (D) narrow stripes on the processed film.

interfering with the light scattered from the object, and  $C_{inc}$  for the pseudohologram.

Let  $I_{inc}$  and  $I_{coh}$  be the intensity distributions on the pseudohologram and on the usual hologram respectively. Let  $a_i$  and  $\phi_i$  be the amplitude and the phase, respectively, of the field at the hologram due to the point  $i$ . It is reasonable to assume:

1.  $I_{inc}$  and  $I_{coh}$  are stationary and ergodic random processes as a function of space coordinates.
2.  $a_i$  and  $\phi_j$ ;  $a_i$  and  $a_j$ ;  $\phi_i$  and  $\phi_j$  are uncorrelated for all  $i \neq j$ .  
 $a_i$  are Gaussian distributed random variables with zero mean.

It is then possible to show that

$$C_{coh} = 1/\sqrt{2}$$

$$C_{inc} = 1/\sqrt{N}$$

where  $N$  is the number of points to be recorded. We thus see that in the usual holography the signal to noise ratio is independent of the number of object points. Therefore, holograms of continuous objects can successfully be recorded. The signal to noise ratio in pseudoholography on the other hand is limited very strongly by  $N$ , the limiting number being approximately 200 (see Ref. [2.2.12]). Therefore discrete objects will yield a better pseudohologram than continuous objects.

Suppose, instead of having cosine shadows, we have very sharp shadows of the form of Fabry-Perot fringes associated with each point. It is possible to show in this case (for a one-dimensional calculation) (Ref. [2.2.13]) that

$$C_{inc} = (1/\sqrt{N}) \cdot \sqrt{\frac{M}{2B} \frac{(w+1)^2}{(2w+1)}} \quad (2.2.61)$$

To get this result it was necessary to assume that the zones have the form:

$$I(x) = \left\{ \begin{array}{l} (x+x_w)^w; \quad -x_w/2 < x < 0 \\ (x-x_w)^w; \quad 0 > x > x_w/2 \end{array} \right\} \quad (2.2.62)$$

where  $w$  determines the sharpness of zone ( $w = 1$  means a triangular zone, etc.)  $x_w$  is the width of the zone,  $B$  accounts for the fact that the separation between the zones is not constant,  $R$  is the distance between two peaks; and  $\Delta R$  is the width of the peak at half maximum. On the average we can write:  $M/B = R/\Delta R$ .

Using practical numbers the increase in signal to noise ratio in Eq. (2.2.61) may reach one order of magnitude!

For a two-dimensional calculation  $C_{inc}$  is proportional to the square of (2.2.61) so that narrowing the zones increases the signal to noise ratio appreciably. Also, from Table 2.1.2 we can see that when the zones are narrow, efficiencies at higher orders increase. Of course by narrowing the zones we let less light through so that a reasonable compromise, that depends on the application, should be made in practice.

### 2.2.8 Noise.

In section 2.1.9 the axial distribution of the noise was discussed using Fourier transforms. Here the transverse distribution of the noise will be described at the various foci, using Fresnel transforms. The grain noise will be considered as a multiplicative noise and the mask serrations as an additive noise. Let  $x$  be a two-dimensional vector,  $Z(x)$  the zone plate function recorded on the film,  $F(x)$  the ideal zone plate function,  $N_g(x)$  the grain noise function, and  $S(x)$  the serration function. We thus can write:

$$Z(x) = [F(x) + S(x)] \cdot N_g(x) = F(x) \cdot N_g(x) + S(x) \cdot N_g(x) \quad (2.2.63)$$

From Eq. (2.2.32)

$$E(X_r) = C \int_{-\infty}^{\infty} F(x) \cdot N_g(x) e^{\frac{iK}{2Z} (X_r - x)^2} dx + \int_{-\infty}^{\infty} S(x) \cdot N_g(x) e^{\frac{iK}{2Z} (X_r - x)^2} dx \quad (2.2.64)$$

If we substitute for  $F(x)$  its Fourier series representation in the  $\xi^2$  domain and use  $I(\alpha) = I_0 \delta(\alpha)$  in (2.2.28), we get for the first term:

$$\sum_{p=-\infty}^{\infty} C_p \int_{-\infty}^{\infty} N_g(x) \text{Circ} \left[ \frac{x}{S_2 \mu}; \xi_N \right] e^{-ip\pi \left[ \frac{x^2}{S_2^2 \mu^2 \xi_1^2} + \frac{iK}{2Z} (X_r - x)^2 \right]} dx \quad (2.2.65)$$

At  $Z = Z_p$  this is reduced to:

$$\begin{aligned}
 & e^{i\phi(x_r^2)} \sum_{p=-\infty}^{\infty} C_p \int_{-\infty}^{\infty} N_g(x) \text{Circ} \left[ \frac{x}{S_{2\mu}}; \epsilon_N \right] e^{\frac{-2\pi i}{\lambda Z_p} x x_r} dx \\
 = & e^{i\phi(x_r^2)} \sum_{p=-\infty}^{\infty} C_p \cdot \tilde{N}_g \left( \frac{x_r}{S_{2\mu} \lambda Z_p} \right) * \frac{\int_0^1 \left[ \frac{2\pi}{\lambda Z_p} (S_{2\mu} x_r \epsilon_N) \right]}{\frac{2\pi S_{2\mu} x_r}{\lambda Z_p}} \quad (2.2.66)
 \end{aligned}$$

where  $\tilde{N}_g(u) = \text{F.T.} \{N_g(x)\}$ .

Hence, the grain noise convolves with the image at every focus.

If  $R_N(\tau)$  is the correlation function of the grain noise, the power spectrum is given (Ref. [2.1.14] p. 347 Eqs. 10-38) for a linear system by:

$$W(u) = S_N(u) \cdot |h(u, p, o)|^2 \quad (2.2.67)$$

where  $S_N(u) = \text{FT} \{R_N(\tau)\}$ ;  $h(u, p, o) = \text{FT} \{\text{Circ}[\epsilon_o; \epsilon_N]\}$  and  $h(x_r, p, o)$  was defined by Eq. (2.2.35) as the point spread function. Hence the power spectrum changes at higher orders, i.e. the speckles become smaller and smaller because the Bessel function gets narrower at high orders. If we assume that the grain noise is a white noise the power spectrum is in the same form as the intensity point spread function (as is seen from (2.2.67)). In imaging, at higher orders the image is demagnified; therefore the appearance of the speckle will not change. However, in pseudoholography since the reconstructed image is not demagnified at higher orders the appearance of the speckle pattern (i.e. with a narrower power spectrum) changes appreciably. Indeed, we observe

this experimentally. The second term in (2.2.64) represents an additive noise. It is in the form of the Fresnel transform of the product of two functions. According to a theorem (analogous to the Fourier Transform Convolution Theorem) the Fresnel transform of a product of two functions is equal to the convolution of their Fresnel transforms. We write the second term as:

$$\text{FRN}\{S(X)\} * \text{FRN}\{N_g(X)\}$$

where  $\text{FRN}\{\quad\}$  denotes the Fresnel transform. Both  $\text{FRN}\{S(X)\}$  and  $\text{FRN}\{N_g(x)\}$  are nonstationary random processes:  $\text{FRN}\{S(X)\}$  consists of contributions from discrete rings; and  $N_g(X)$  is signal dependent. Very little has been done in connection with serrated apertures and a complete discussion is beyond the scope of this work. Qualitatively speaking, the additive noise as seen through a microscope looking at the reconstruction of a pseudohologram will appear as a complicated speckle pattern consisting of circular structures modulated by random fluctuations.

The intensity and the contrast of the speckle pattern does not change appreciably when we move from distance  $Z$  from the zone plate to  $Z'$  (see Ref. [2.2.21]) and so if the efficiency at higher order decreases we experience a net decrease in the signal to noise ratio. Experimentally, as we observe closer to the zone plate than a certain distance we see only speckles; no further focusing effects are apparent.

#### 2.2.8.1 Quantum Noise Considerations.

It has been claimed (ref. [2.2.4] and references therein) that there is a considerable gain in using zone plate pseudoholography instead of a pinhole camera by a factor of the ratio between the corresponding collection solid angles. However, we see in Ref. [2.2.14] that the advantage in the signal to noise ratio for zone plates compared with the pinhole camera decreases as a function of the number of picture elements. In fact this calculation is only for two-dimensional objects while in reality there are contributions recorded from a three-dimensional volume. This will tend to decrease the advantage even further. Suppose a picture element is defined as the area (or volume in case of three-dimensional object) covered by one point spread function of the system. In the case of laser pellet compression experiments there are at least 1000 ( $100 = 10 \times 10$  in transverse plane and 10 in axial direction) picture elements in the volume. Therefore, there is no net gain over the pinhole camera in terms of signal to noise ratio. Furthermore, as will be seen later on, there are artifacts introduced in the pseudoholographic technique which tend to further decrease the signal to noise ratio.

#### 2.2.9 Method of Reconstruction.

We can distinguish between optical, digital and hybrid optical and digital reconstruction techniques.

##### 2.2.9.1 Optical Methods.

#### 2.2.9.1.1 The Direct Reconstruction.

This method is illustrated in Fig. 2.2.8. We can distinguish between two variants according to whether optical filtering is used or not.

- 1a. A collimated laser beam is incident on the pseudohologram as in Fig. 2.2.12a. Every recorded zone plate focuses the light to a series of foci, hence the image is multiply reconstructed. Positive or real foci are to the right of the zone plate in Fig. 2.2.12a and negative or virtual foci are to the left.

The direct reconstruction has the advantage of permitting easy investigation of the images at the various orders. By looking at different orders, artifacts which arise and which are introduced in only some orders, may be identified immediately. This method was used in this work and results are discussed in Chapter 3.

- 1b. Filtering the pseudohologram.

The pseudohologram is illuminated with a converging beam as in Fig. 2.2.12b. The background is focussed at the Fourier plane and a D.C. block is used. The size of the D.C. block is very critical because the objects may have low frequency components. In Ref. [2.2.15] the same technique is applied to off axis zone plates.

#### 2.2.9.1.2 Optical Correlations.

- 2a. In one method the pseudohologram is correlated with the coded aperture using an incoherent system as shown in Fig. 2.2.13.
- 2b. The second method may be performed using a coherent system as in

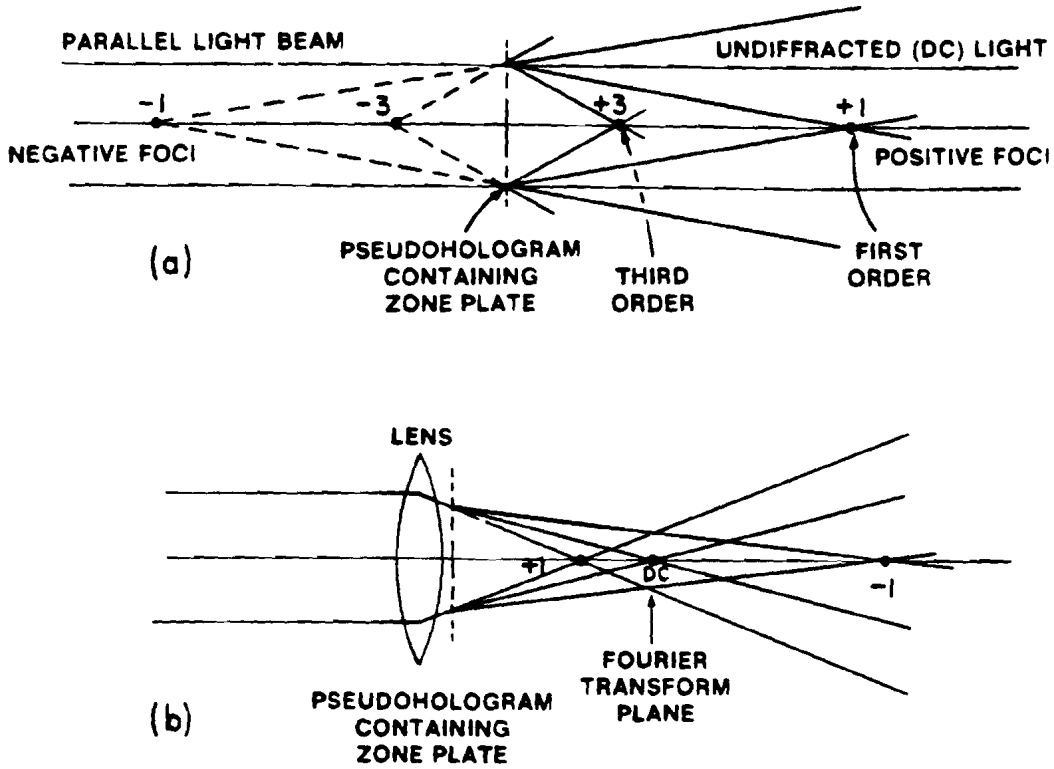


Fig. 2.2.12

Methods of optical reconstruction of pseudoholograms.

(a) Direct reconstruction using collimated light

(b) Direct reconstruction using converging light hence allowing the filtering out of DC. (The pseudohologram can be placed in front of the lens also.) (After [2.2.15])

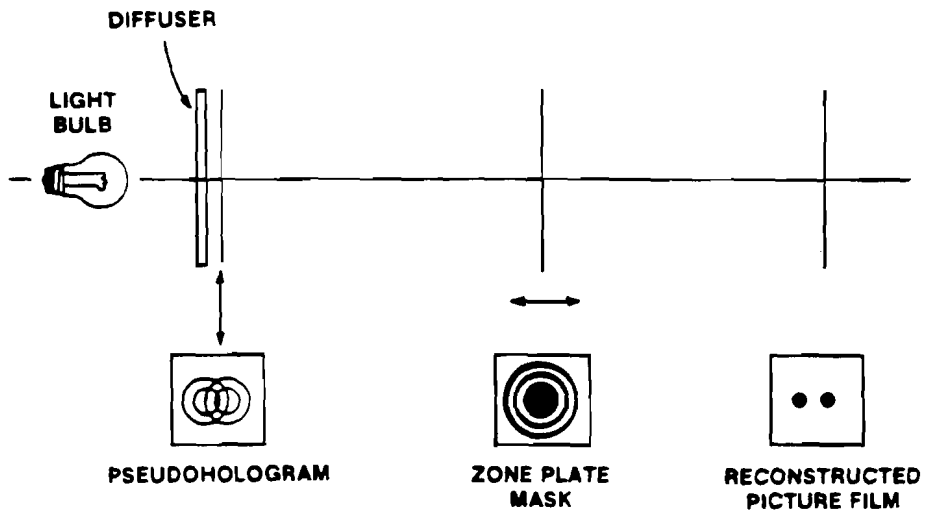


Fig. 2.2.13  
Optical correlation using incoherent light. By correlating the coded aperture with the pseudohologram, the object is reconstructed. (After [2.2.15])

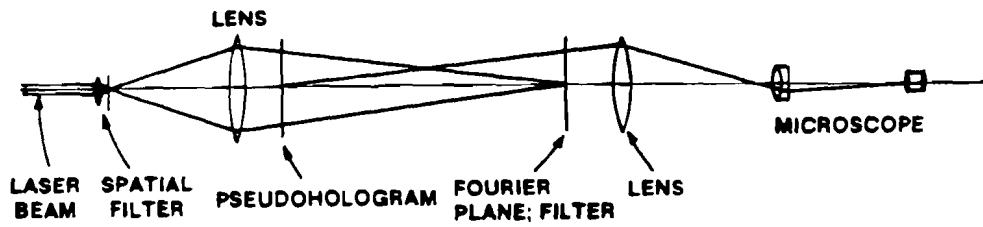


Fig. 2.2.14  
Coherent optical system for reconstructing pseudoholograms (After [2.2.15])

Fig. 2.2.14 and discussed in Ref. [2.2.16] Figs. 2 and 6. The basis of the correlation method is the fact that in cases where diffraction effects are truly negligible (such as in recordings with  $\gamma$  rays,  $\alpha$  particles, or very hard x-rays) the recorded intensity on the film is given by

$$I(x) = M(x) * O(x) \quad (2.2.68)$$

as it was derived in Eq. (2.2.15a). By correlating (2.2.68) with  $M(x)$  we get

$$I_R(x) = M(x) * [M(x) * O(x)] \quad (2.2.69)$$

which we write

$$I_R(x) = [M(x) * M(x)] * O(x) \quad (2.2.70)$$

Thus if  $M(x)$  is a mask such that its autocorrelation is a sharp function then (2.2.70) represents a reconstruction of the source  $O(x)$ . This correlation can be performed incoherently as in Fig. 2.2.13 or coherently as in Fig. 2.2.14. In the latter case we have in the Fourier plane the Fourier transform of (2.2.68) or

$$\tilde{I}(u) = \tilde{M}(u) \tilde{O}(u) \quad (2.2.71)$$

If we can fabricate a filter which is the Fourier transform of the mask we may put it in the Fourier plane and get:

$$\tilde{I}'(u) = \tilde{O}(u) \cdot \tilde{M}(u) \tilde{M}(u) \quad (2.2.72)$$

Going back to the image plane we get:

$$I'(X_r) = O(X_r) * [M(X_r) * M(X_r)] \quad (2.2.73)$$

This technique has inherently less resolution than the direct reconstruction, because the width of the point spread function is always larger than twice the width of the smallest detail in the coded aperture. (In an annular aperture, as an example, the point spread function is larger than twice the width of the annulus.) Hence this method is not useful for applications where high resolution is needed.

### 2.2.9.1.3 Optical Deconvolutions.

This method may be the most promising technique for achieving high resolution reconstructions of pseudoholograms. In fact, even pinhole camera pictures may be enhanced and improved with this technique, which is illustrated in Fig. 2.2.15 and discussed in Ref. [2.2.17]. Although it is a simple method conceptually it is very difficult to apply experimentally. As in (2.2.68) the intensity is given by a convolution. However, this time we do not need to assume that we have only very hard radiation and we can write the convolution in a more general form:

$$I(X) = O(X) * G(X) \quad (2.2.74)$$

where  $G(X)$  is given by:

$$G(X) = \left[ \int_{-\infty}^{\infty} \sqrt{M(\xi)} e^{iK \left[ \frac{1}{2} \left( \frac{1}{S_1} + \frac{1}{S_2} \right) \xi^2 - \left( \frac{a}{S_1} + \frac{X}{S_2} \right) \xi \right]} d\xi \right]^2 \quad (\text{see (2.2.9)})$$

(It was shown in (2.2.13) that  $G(X) = M(X)$  when  $\lambda \rightarrow 0$ .) Using a coherent optical system, in the Fourier plane, we get:

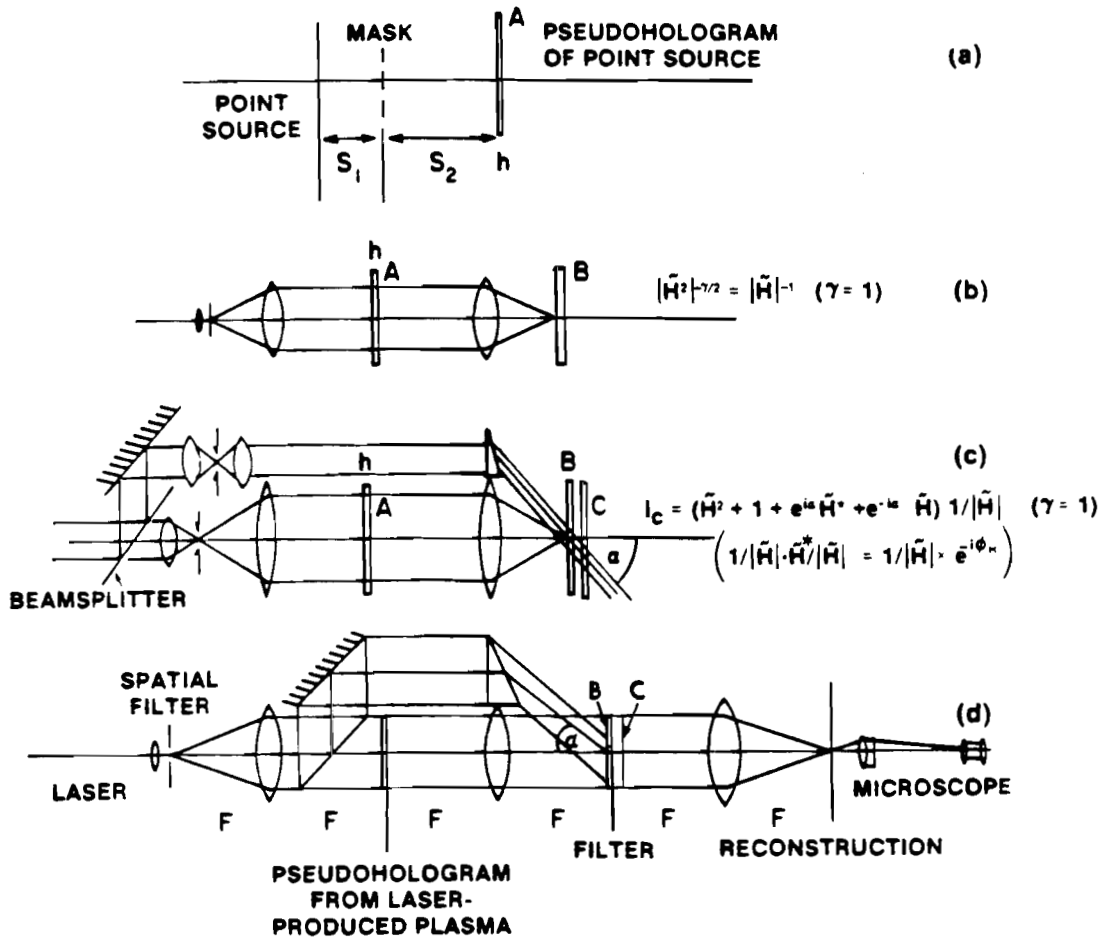


Fig. 2.2.15

Optical deconvolution of pseudoholograms.

- (a) recording pseudohologram of a point source with spectrum similar to the real experiment, (b) amplitude part of the filter, (c) phase part of the filter, and (d) reconstruction system (After [2.2.17])

$$\tilde{I}(u) = \tilde{O}(u) \cdot \tilde{G}(u) \quad (2.2.75)$$

We thus need to produce a filter in the form  $1/\tilde{G}(u)$ . Then clearly

$$\tilde{I}'(u) = [\tilde{O}(u) \cdot \tilde{G}(u)] 1/\tilde{G}(u) = \tilde{O}(u) \quad (2.2.76)$$

Which gives us the reconstructed object in the image plane. The main problem is producing the filter. This problem is discussed Ref. [2.2.17].

To apply this technique to our case we need an extremely small x-ray source. (These sources may become available soon as there is now a growing interest in this subject. See Ref. [2.2.18].) The resolution will depend on the source size.

Using the same configuration as in the laser pellet compression experiment we take a pseudohologram of the point source. We now produce  $1/\tilde{G}(u)$  optically, see Fig. 2.2.15a, b, c and d and put it in the Fourier plane. We can place the pseudohologram of the object in the input of a coherent system (see Fig. 2.2.15e) and observe the reconstructed image. The ultimate resolution will depend on the test source size.

To obtain tomographic resolution we need to produce several filters by slightly changing the source to zone plate distance with each filter (see Fig. 2.2.15a).

For sources with very hard radiation this method should resolve details on the order of the point source which was used to produce the filter. For softer radiation where diffraction effects are present the limitation will be the fact that the spectrum of the point source is significantly different from that of the plasma and so the characteristic

diffraction effects will not match exactly when performing the deconvolution. However this effect can be shown not to limit the usefulness of the technique, and we may still get higher resolution than in any other method.

#### 2.2.9.2 Digital Reconstructions.

Except for simulation with one-dimensional pseudoholograms this method was not used in this work. Direct digital reconstruction may be performed by digitizing the recorded pseudohologram and performing a Fresnel transformation on it. This can be done by multiplying each data element by the appropriate quadratic phase factor and then performing an FFT to each of the foci. A correlation may be performed by digitally correlating the sampled data with the coded aperture. Another way would be to perform a Fast Fourier Transform (FFT) on the digitized data. The filter function may be computed either by performing an FFT on the coded aperture function itself or on one of its derivatives (see Ref. [2.2.16]). After multiplying the filter function by the computed Fourier Transform of the object function, an inverse FFT is performed and the reconstructed image is obtained.

While in the direct method the coded aperture has to be a zone plate, in the correlation method a zone plate is not necessary and annular apertures have been used [2.2.15]. It seems that annular apertures are suitable for this method but it remains to be shown that these are indeed the most effective forms.

Deconvolution is also feasible with any type of coded aperture. Here we digitize the pseudohologram of a point source, perform an FFT

to get  $\tilde{H}(u)$  and form  $1/\tilde{H}(u)$  digitally. We take the FFT of the real data and multiply by the calculated  $1/\tilde{H}(u)$  and finally take the inverse FFT to get the reconstructed image. Also, one might envision recording the data digitally with an array of x-ray detectors rather than with x-ray film; then reconstructions may be obtained on line.

### 2.2.9.3 Hybrid Digital Optical Reconstruction.

For both the correlation and the deconvolution methods the filter may be produced digitally and then used in the Fourier plane of the optical system.

### 2.2.10 A Comparison of the Resolution at Higher Orders Between Imaging with a Zone Plate and the Zone Plate Pseudoholographic Technique.

In Fig. 2.2.16 there is a comparison between the two methods. In at least two papers published recently [2.2.19], [2.2.20] it is claimed that the resolution increases in higher order images formed with zone plates. That this cannot be true is seen in Fig. 2.2.16a. At higher orders the Airy disc becomes smaller but the image does also by the same factor; therefore the resolution in object space cannot increase. On the other hand in pseudoholography, illustrated in Fig. 2.2.16b, at higher orders the Airy disc is smaller but the image has exactly the same size (using collimated light) so there is a net increase of resolution. Looking at higher orders simply allows one to observe the reconstructed image with a higher numerical aperture.

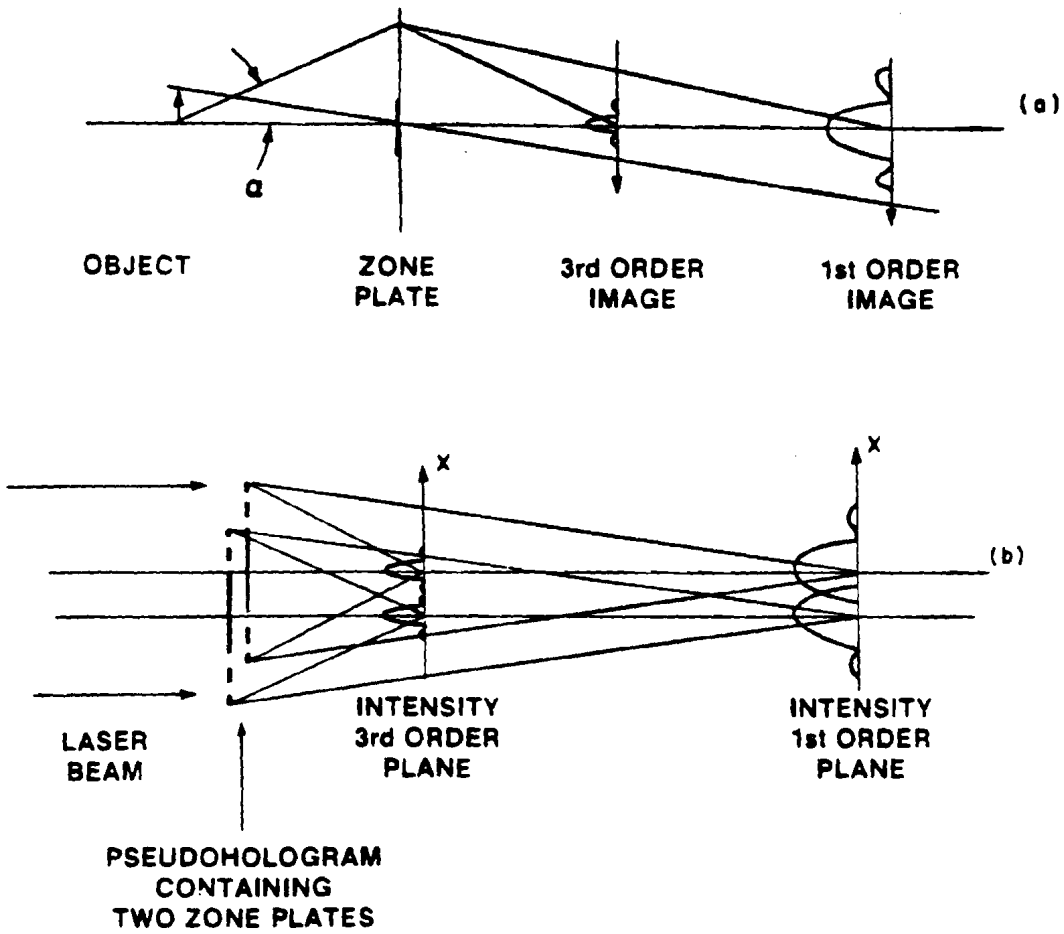


Fig. 2.2.16  
Comparison between imaging with zone plate at higher orders and reconstruction of a pseudohologram.

- (a) The Airy disc scales with the image
- (b) The image stays the same, the Airy disc becomes smaller

2.2.11 Comments on One-Dimensional Zone Plates.

2.2.11.1 Axial Distribution.

Starting with Eq. (2.1.1), using one-dimensional coordinates we can derive an equation which corresponds to the previous two-dimensional case Eq. (2.1.9) (see discussion in section 2.1 for notation).

$$G'(u) = \int_0^1 \frac{A(t)}{\sqrt{t}} e^{2\pi i u t} dt \quad (2.2.77)$$

or

$$G'(u) = \tilde{A}(u) * \text{FT} \left[ \frac{1}{\sqrt{t}} \right] = \tilde{A}(u) * \left[ \frac{2}{\pi\sqrt{u}} \right] \quad (2.2.78)$$

But

$$\tilde{A}(u) = \tilde{B}_a(u) \sum_n \delta(u - \frac{2q}{n}) * \frac{\sin(\pi q N u)}{\pi u} \quad (2.2.79)$$

So that 
$$G'(u) = \tilde{B}_a(u) \sum_n \delta(u - \frac{2n}{q}) * \left[ \frac{\sin(\pi q N u)}{\pi u} * \left[ \frac{2}{\pi\sqrt{u}} \right] \right]$$

So the new point spread function in the axial direction is

$$\frac{\sin(\pi q N u)}{\pi u} * \left[ \frac{2}{\pi\sqrt{u}} \right] \quad (2.2.80)$$

This causes a broadening of axial intensity distribution (see Fig. 2.2.17, a comparison between the sinc and  $1/\sqrt{u}$  functions between two foci) and therefore increases the background and noise. To improve this we can apodize with the function  $AP(X) = |X|$  (see Fig. 2.2.18). This will cause Eq. (2.1.1) to reduce to:

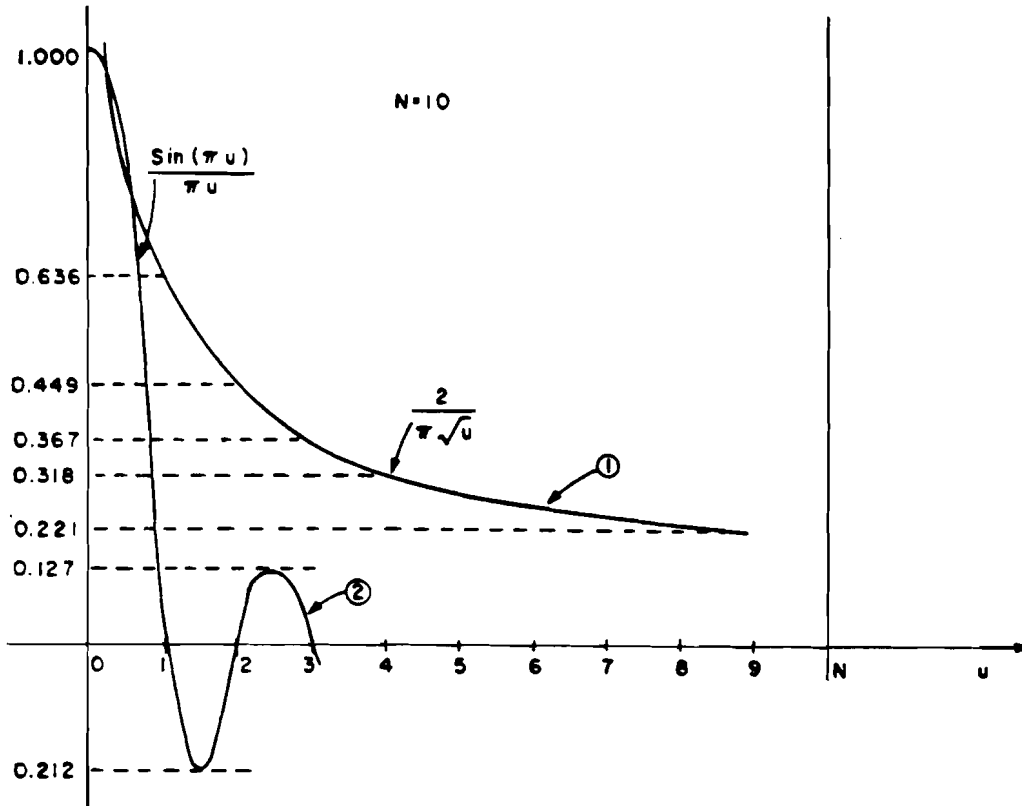


Fig. 2.2.17  
Comparison between the sinc function and the  $1/\sqrt{u}$  function in the case of one-dimensional zone plate.  
(1) is the  $2/\pi\sqrt{u}$  function. (2) is the  $\sin(\pi u)/\pi u$  function.

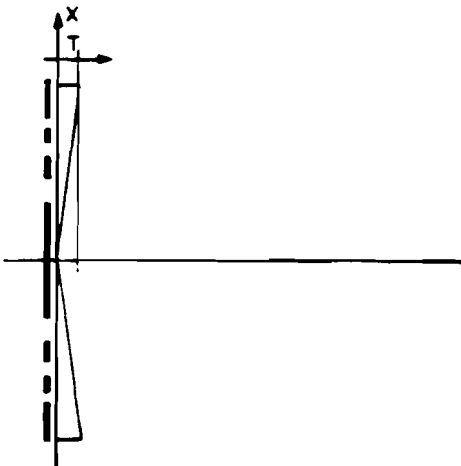


Fig. 2.2.18  
Apodization of a one-dimensional zone plate in order to achieve on axis intensity distribution like the two-dimensional zone plate.

$$G'(u) = \int_0^1 A(t) e^{2\pi i u t} dt \quad (2.2.81)$$

exactly as Eq. 2.1.9.

### 2.2.11.2 Transverse Distribution.

It is possible to apply all the derivation in section 2.2.2. The only difference is in Eq. (2.2.35). We get a sinc function and not a Bessel function. Nothing in this derivation was special to two dimensions. We can then write from Eq. (2.2.36)

$$E(X_r) = \sum_{p=-\infty}^{\infty} \frac{c_p e^{iKZp}}{\lambda Z p} \int_{-\infty}^{\infty} d\alpha l(\alpha) \cdot h'(\alpha, X_r, p) , \quad (2.2.82)$$

where  $h'(\alpha, X_r, p)$  is defined in (2.2.35) with sinc instead of  $J_1$ . Hence the transverse distribution resembles the two-dimensional curve.

We will see in the next chapter that pseudoholography with one-dimensional zone plates may be useful in some investigations of laser produced plasmas.

### 2.2.12 Computer Simulations.

A computer program was written and is listed in Appendix 3, where the recording of a pseudohologram was simulated. The source function and the

mask function are represented by vectors. The number of a vector element is proportional to its location. The value of a vector element is the intensity function in the case of the source function, and the transmittance intensity in case of the mask. Given the source size, the distance between the source and the zone plate, the distance between the mask and the film plane, the outermost zone width, and the number of zones, the film size is determined in such a way as to allow all the rays from the source through the zone plate mask to fall on the film (see Fig. 2.2.19). A ray is traced from each point in the source to all the mask points. The location of point of incidence with the film is calculated only for those rays which hit a clear area and the location is stored in a vector in the following way. Assume, for example, that a ray hits the film at a distance  $3\text{mm}$  above the optical axis. This is normalized with respect to the calculated film size to  $0.1015$  say. This number is multiplied by the number of points we chose for the film vector. This is now to the nearest integer the element number. The value of this element will be used to represent one photon absorbed in this location. The intensity increases by the value of 1 for each ray hitting the same cell. The rays are traced from every object point through every point in the mask. If at a certain point, the mask is opaque, the ray is not traced further and another ray is traced through another point in the mask. After the pseudohologram is recorded on the disc we use the propagation program (see Ref. [2.2.22] and listing in Appendix 2) which was modified to suit our needs. We read the pseudohologram from the disc and calculate the Fresnel integrals for several distances along the axis. We then plot the transverse intensity distribution at

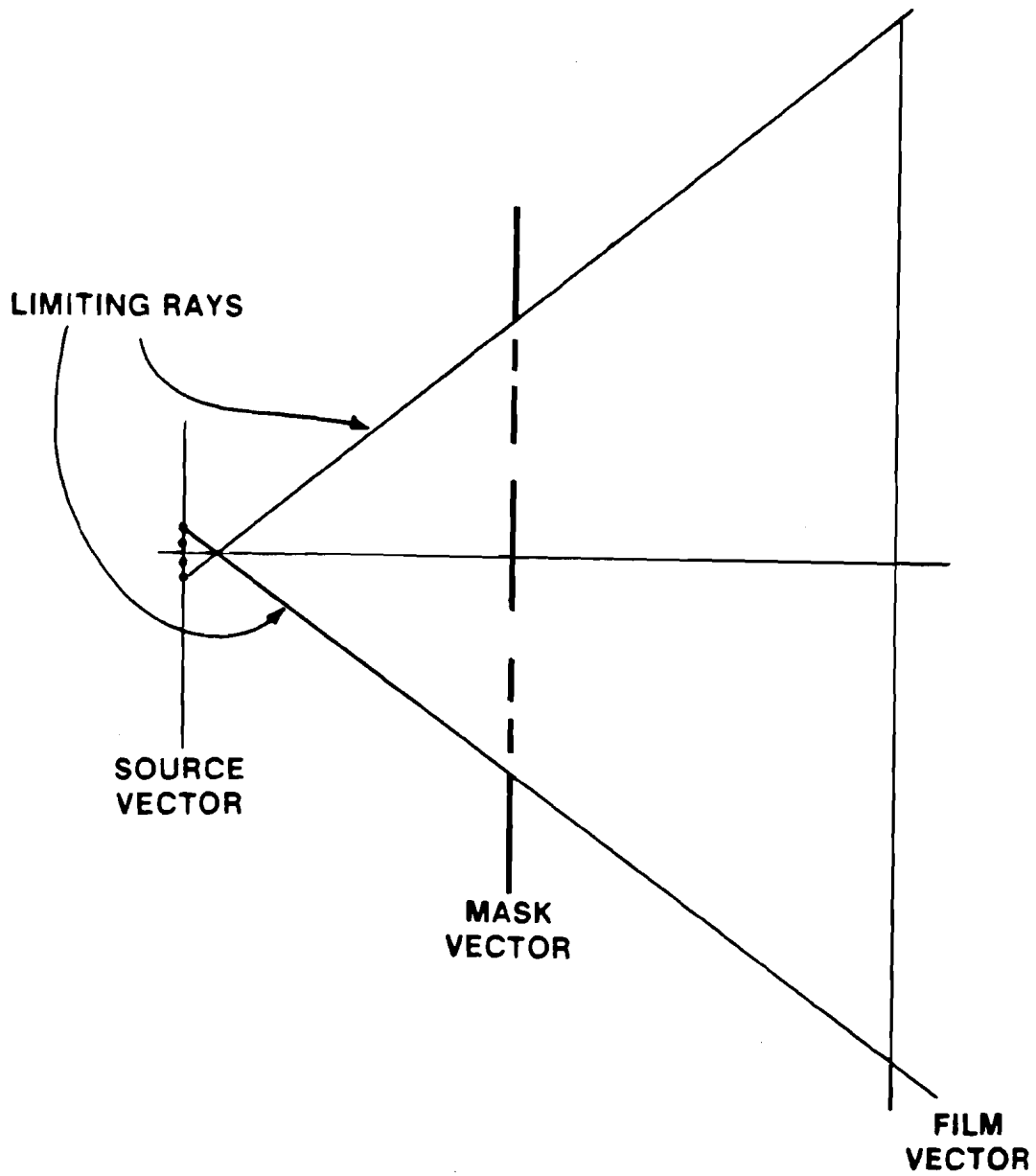


**Fig. 2.2.19**  
Determination of the film size for the computer simulation. The limiting rays are traced from the edge of the source to the edge of the mask to determine the film size.

the various foci. The different cases are summarized in Table 2.2.1. The notations are explained in Fig. 2.2.20.  $r$  denotes the width of the outermost zone.

2.2.12.1 Comments on using the propagation program for the investigation of diffraction effects in the recording step of a pseudohologram.

From section 2.1.11.2 we have that:

$$TBDM = N\lambda z / TOTD \quad (2.2.83)$$

where TOTD is the width of the input space. TBDM is the width of the output space,  $N$  is the number of sample points,  $\lambda$  is the wavelength,  $z$  is the propagation distance. For an x-ray experiment TOTD is of the order of 3mm,  $\lambda$  is about  $10\text{\AA}$ ,  $z$  is about 10 cm. If we require that TBDM is of the order of 1 cm we get from (2.2.83) that  $N \gg 3 \cdot 10^4$  points. This number is too large for use on the computer. An alternative approach would be to calculate the diffraction effects from the expressions derived in section 2.2.1, e.g. (2.2.20) and (2.2.22) using the stationary phase method. By Fourier transforming the pattern we get the efficiencies at higher orders.

2.2.12.2 Conclusions from the Computer Simulations.

In Fig. 2.2.21 the reconstructions of a simulated pseudohologram of two point sources are shown. We note that both first and third order reconstructions are not sensitive to change in  $\gamma$  (the slope of H&D curve). The second order however is extremely sensitive to change in  $\gamma$ . In theory the even order reconstructions should be identically zero, since

Table 2.2.1: Parameters of Different Computer Runs  
Calculating the Reconstruction of a Simulated Pseudohologram

<u>Object</u>	<u>S</u>	<u>Width</u>	<u>Zone Plate</u>			<u>Y</u>	<u>N</u>	<u>Fig. #</u>
			<u>F</u>	<u>NZONE</u>	<u>POS/NEG</u>			
2 PNTS	r		150	37	POS	1	2048	2.2.19
2 PNTS	r		150	37	POS	2	2048	2.2.19
2 PNTS	r		150	37	POS	4	2048	2.2.19
2 FIN SRCS	r	r/2	150	37	POS	1	4096	2.2.20a
2 FIN SRCS	r	r/2	150	37	POS	2	4096	2.2.20a
2 FIN SRCS	r	r/2	150	37	POS	4	4096	2.2.20a
2 FIN SRCS	r	0.8r	150	100	POS	1	4096	2.2.20b
2 FIN SRCS	r	0.8r	150	100	POS	2	4096	2.2.20b
2 FIN SRCS	r	0.8r	150	100	POS	4	4096	2.2.20b

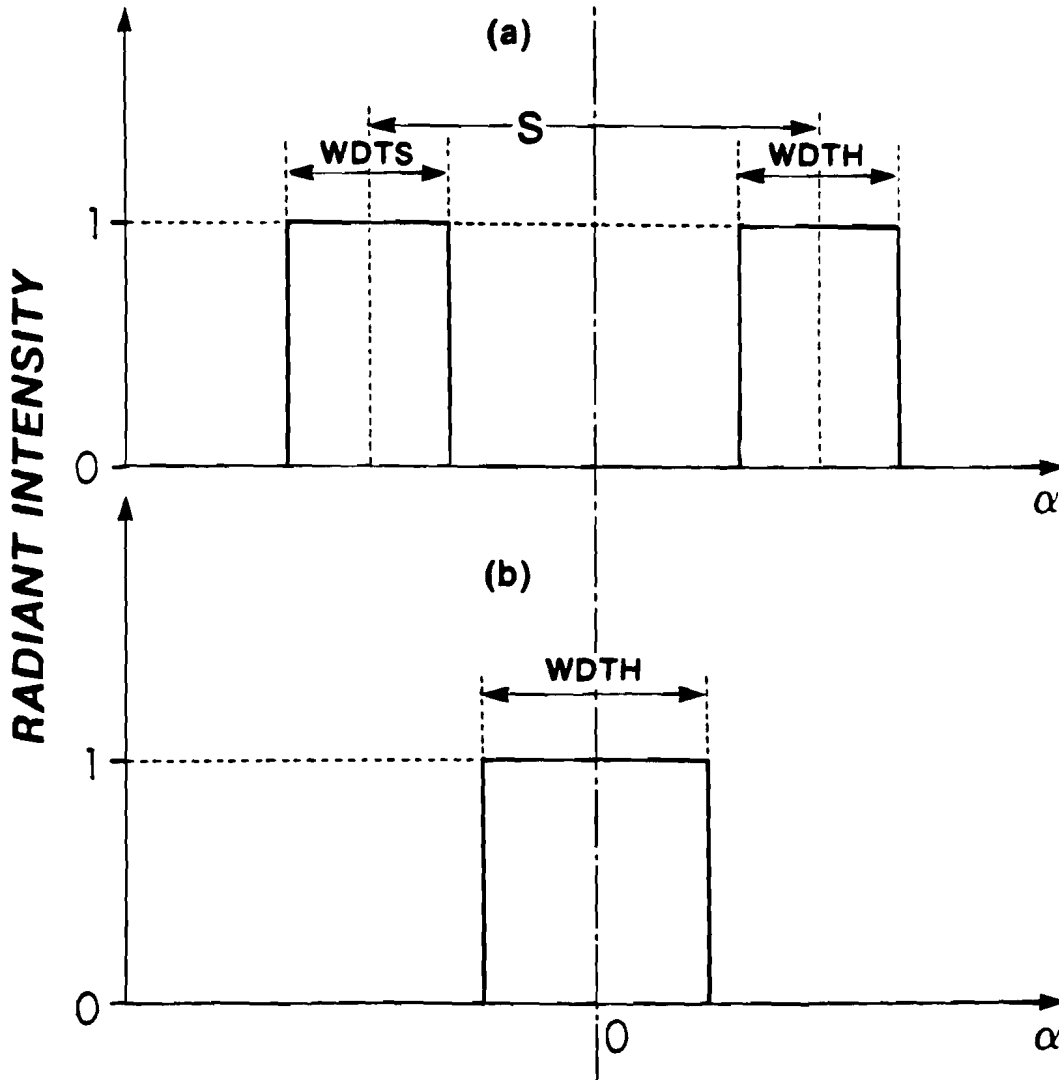


**Fig. 2.2.20**  
Notation for the source function used in the computer simulations. (a) Two finite point sources, (b) one finite point source.

we use a Fresnel zone plate as a coded aperture. However, when we record a pseudohologram of more than one point source we no longer have an ideal Fresnel zone plate. The interaction between the two ideal zone plates produces an even order reconstruction. Since the origin of the even order reconstruction is an interaction between two patterns, it will depend on the  $\gamma$  with which the film is processed. In Fig. 2.2.21 we see that for  $\gamma = 1$  the second order reconstruction is negligible but at  $\gamma = 4$  is of the order of the third order reconstruction. The object is not resolved in the second order for  $\gamma = 4$  but we observe some modulation at the top of the pattern. The intensity at the third order reconstruction is much lower than at the first order reconstruction, but the object is clearly resolved in the third order and not in the first order. The high intensity of secondary lobes in the third order reconstruction represent a disturbing effect. A way to avoid this problem is to use a zone plate with larger number of zones. The reconstructions of a pseudohologram of two finite sources using 37 and 100 zones zone plates for 3 different  $\gamma$  are plotted in Fig. 2.2.22a and 2.2.22b. While in Fig. 2.2.21 the third order reconstructions were insensitive to  $\gamma$  here, for finite source, the third order is very sensitive. While in 2.2.22a the resolution seems to decrease at high  $\gamma$ , in 2.2.22b the resolution seems to increase at high  $\gamma$ . We thus see that the process is object dependent and it may be possible to find the optimum  $\gamma$  for certain types of objects. Also we see that by using a zone plate with large number of zones the secondary lobes decrease appreciably.

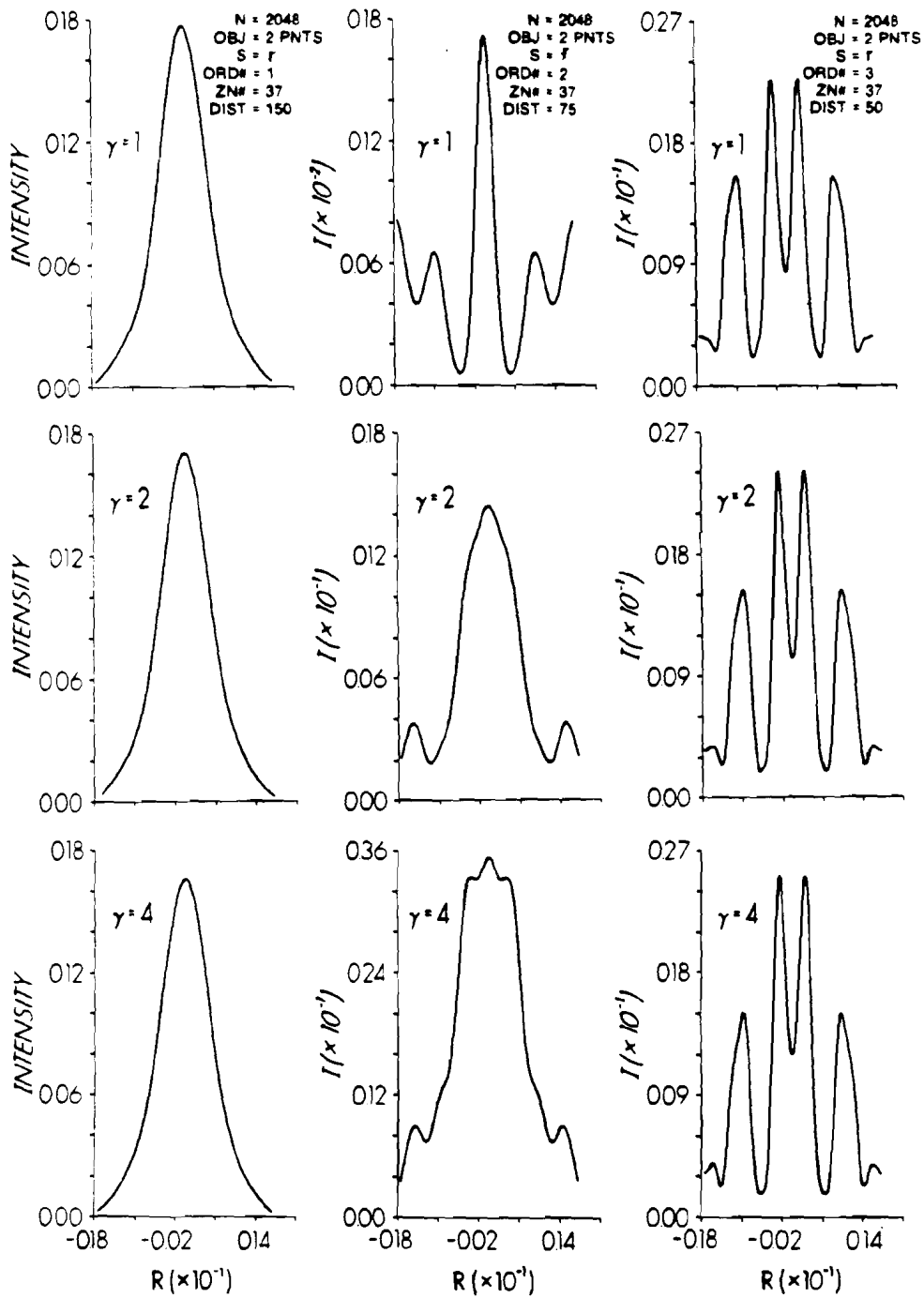


**Fig. 2.2.21**  
Reconstructions of simulated pseudoholograms of two point sources.  $r$  is the width of the outermost zone. (See Fig. 2.2.20 for notation.)

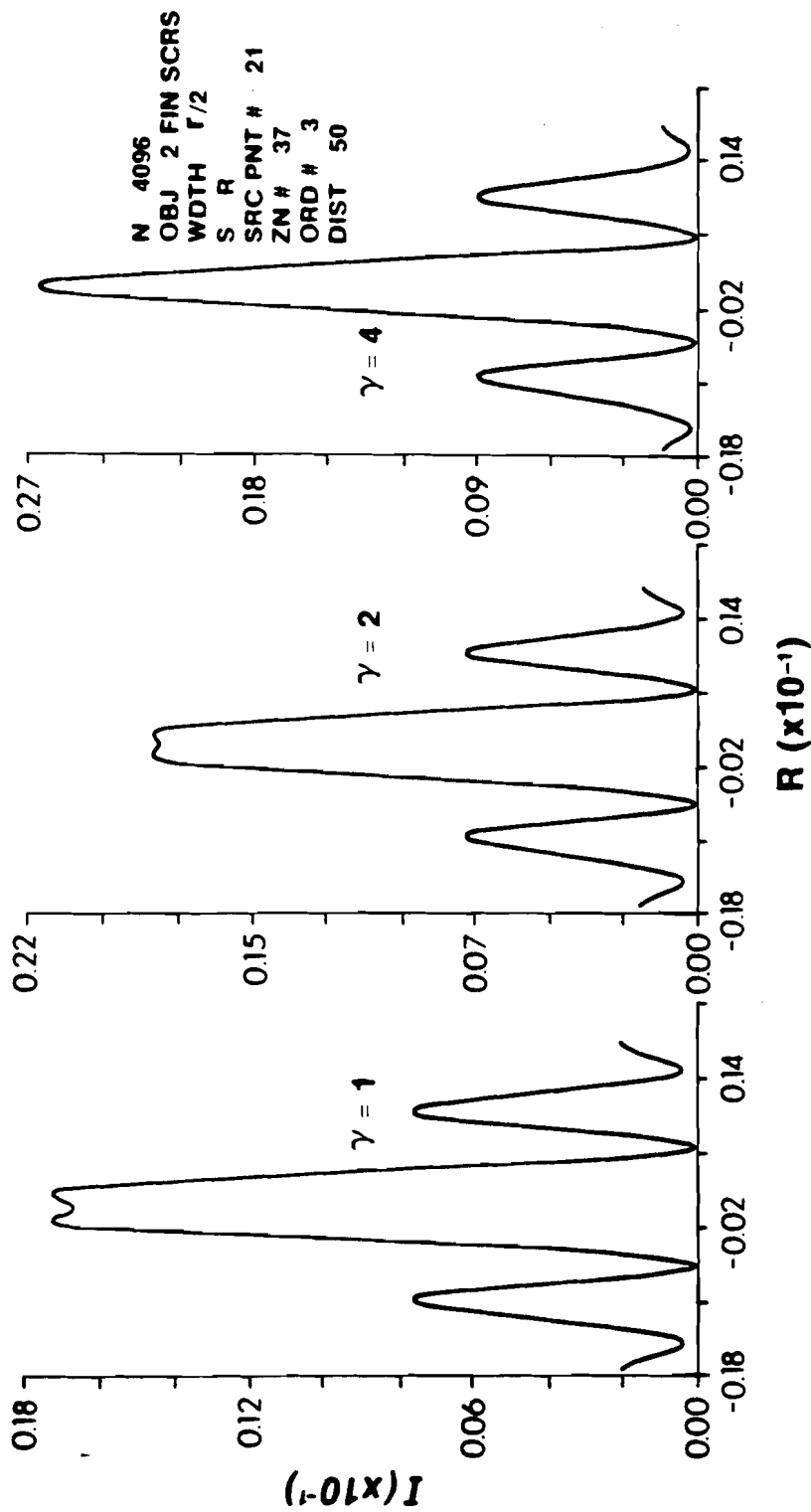


Fig. 2.2.22a  
Reconstructions of a simulated pseudohologram of two finite sources. Zone plate has 37 zones.

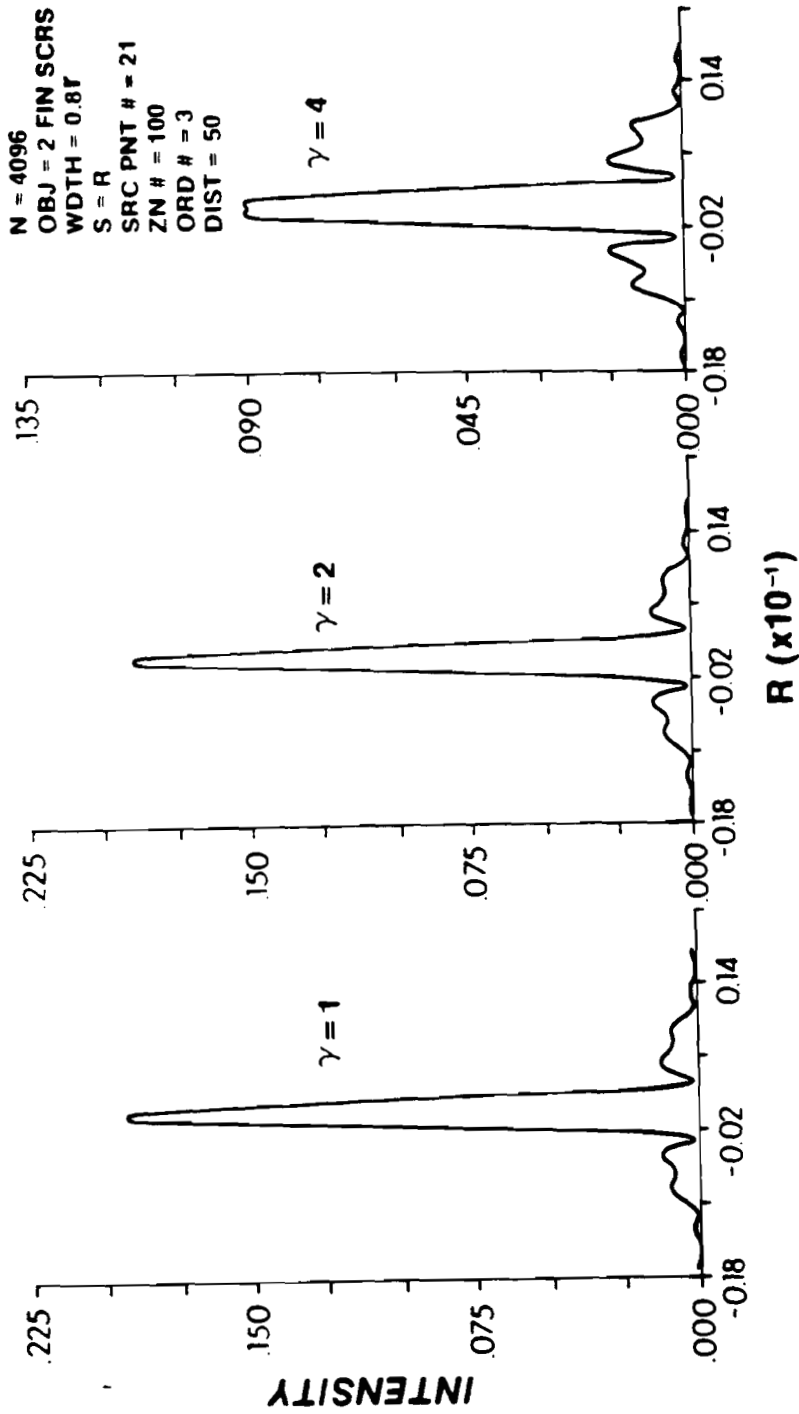


Fig. 2.2.22b  
Reconstructions of a simulated pseudohologram of two finite sources. Zone plate has 100 zones.

2.2.13 REFERENCES

- 2.2.1 N. M. Ceglio, "Zone Plate Imaging of Laser Produced Plasmas",  
PhD. Thesis, M.I.T., Aug., 1976.
- 2.2.2 L. Mertz and N. O. Young, "Fresnel Transformations of Images",  
Proc. Int. Conf. on Opt. Instrum., London 305 (1961).
- 2.2.3 H. H. Barrett, J. Nuc. Med., 13, 382 (1972).
- 2.2.4 N. M. Ceglio, "X-Ray Microscopy of Laser Fusion Plasmas using  
Coded Imaging Techniques", SPIE 106, X-ray Imaging 55 (1977).
- 2.2.5 H. Born and E. Wolf, "Principles of Optics", Pergamon Press 5th  
edition, (1975), p. 752.
- 2.2.6 A. Erdelyi, "Asymptotic Expansions", Dover 1956, §2.9.
- 2.2.7 J. M. Stone, "Radiation and Optics", McGraw Hill Book Co.,  
1963, p. 194.
- 2.2.8 Standard Mathematical Tables, S. M. Selby , Ed., C.R.C. 19th  
edition, 1971, p. 464.
- 2.2.9 J. W. Goodman, "Introduction to Fourier Optics", McGraw Hill,  
1968, p. 150.
- 2.2.10 G. B. Parrent and B. J. Thompson, Physical Optics Notebook.  
(Society of Photo-Optical Instrumentation Engineers, 216  
Avenida del Norte, Redondo Beach, California 90277, 1969),  
p. 51.
- 2.2.11 J. Gur and J. M. Forsyth, "Optical Simulation of a Technique  
for Obtaining Submicron Resolution X-Ray Images in Laser Pellet  
Compression Experiments", Appl. Opt. 17, 1 (1978).
- 2.2.12 (a) M. Marchant and D. Knight, "Multiple Recording of Holograms",  
Optica Acta 14, 199 (1967).

(b) E. Spitz, A. Werts, "Reconstitution dans l'Espace d'une Courbe Enregistree par Deplacement d'un Point Luminoux", Comptes Rendues 262, B758 (1966).

2.2.13 J. Gur " Pseudoholography with Incoherent Illumination", Industrial Associates Meeting Institute of Optics, University of Rochester, Dec. 1976, p. 26.

2.2.14 H. H. Barrett and G. D. DeMeester, "Quantum Noise in Fresnel Zone Plate Imaging", Appl. Opt. 13, 1100 (1974).

2.2.15 R. G. Simpson and H. H. Barrett, "Coded Aperture Imaging" in "Imaging in Diagnostic Medicine". S. Nudelman, Ed. Plenum Publishing Corp., N.Y.

2.2.16 H. H. Barrett, W. W. Stoner, D. T. Wilson, G. D. DeMeester, "Coded Apertures Derived from the Fresnel Zone Plate", Opt. Eng. 13, 539 (1974).

2.2.17 (a) G. W. Stroke, M. Halioua, F. Thon, D. M. Willasch, "Image Improvement in High Resolution Electron Microscopy Using Holographic Image Deconvolution", Optik 41, 314 (1974).

(b) G. W. Stroke, M. Halioua, "Attainment of Diffraction Limited in High-Resolution Electron Microscopy by 'a posteriori' Holographic Image Sharpening", Optik 35, 50 (1972).

(c) G. W. Stroke, M. Halioua, "Image Improvement in High Resolution Electron Microscopy with Coherent Illumination" (Low Contrast Objects using Holographic Image Deblurring Deconvolution 111B) Optik 37, 244 (1973).

2.2.18 R. H. Prince, M. J. Boyle and S. S. Glaros, "A Miniature X-Ray Point Source for Alignment and Calibration of X-Ray Optics.

APS Plasma Physics Meeting, Nov. 5-11, 1977.

- 2.2.19 G. Schmahl, D. Rudolph and B. Niemann, "X-Ray Microanalysis of Biological Specimens with Zone Plates and Synchrotron Radiation", 8th International Conference on X-Ray Optics and Microanalysis and the 12th Annual Conference of the Microbeam Analysis, Boston, Mass. 1977, p. 601.
- 2.2.20 Germain Boivin "Use of a Fresnel Zone Plate for Optical Image Formation with Short Wavelength Radiations", Appl. Opt. 16, 1071 (1977).
- 2.2.21 (a) J. C. Dainty, Ed., "Laser Speckle and Related Phenomena", Springer-Verlag (1975).  
(b) J. C. Dainty, "The Statistics of Speckle Patterns", Progress in Optics, E. Wolf, Ed., North Holland (1976).
- 2.2.22 E. Krisl, PhD. Thesis, "Apodization of Coherent Optical Systems" University of Rochester, (1978).

CHAPTER III

EXPERIMENTAL INVESTIGATION

### 3. Experimental Investigation.

#### 3.1 Demonstration of Resolution Improvement at High Order Reconstructions.

We have already seen that at high order reconstructions, the resolution improves according to Eq. (2.2.56).

To verify the usefulness of the predicted improvement in resolution in the higher order foci, an optical simulation experiment was performed. The recording system is shown in Fig. 3.1. A tungsten light source illuminated the diffuser through a shutter. A mask with a pair of 1mm holes separated by 3.1mm between centers was (see Fig. 3.2a) placed in contact with the diffuser. A Fresnel zone plate with 40 zones and a film cassette were free to move on the rail along the optical axis.

The desired ratio  $S_2/S_1$  was obtained by moving both the zone plate and film to the appropriate positions. Using the same mask, by changing  $S_2/S_1$  we could simulate different separations between the two holes. Two films were tried: Tri-X developed in D-76 for 6 min., and Contrast Processing Ortho developed in D-11 for 4.5 min.

The recorded shadowgram was reduced approximately 20 times with a 35mm camera fitted with a 50mm focal length lens set at  $f/5.6$ . The finest detail was not less than  $50\mu\text{m}$  and so the pseudohologram was completely resolved by the camera lens. Kodak S0253 high resolution film, developed for 4.5 min. in D-165 at a concentration of 1:4 was used. The shadowgram is shown in Fig. 3.3a.

The complete reconstruction system is shown in Fig. 3.4. The laser beam was focussed through a spatial filter. Then it was colli-

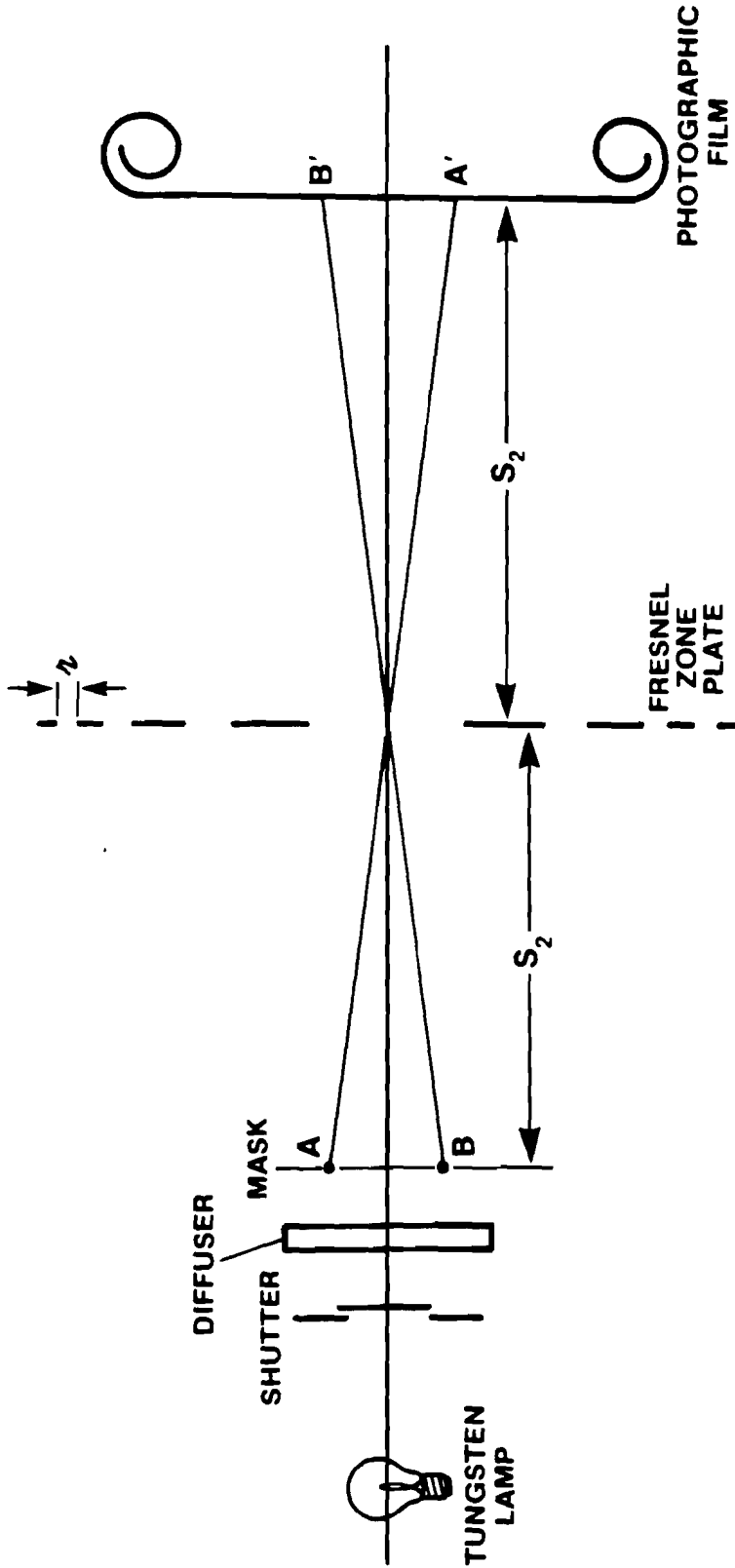
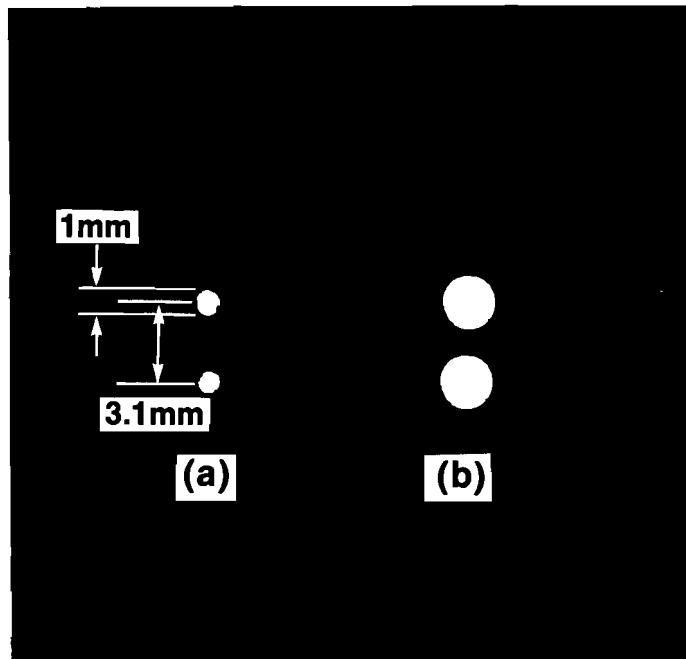
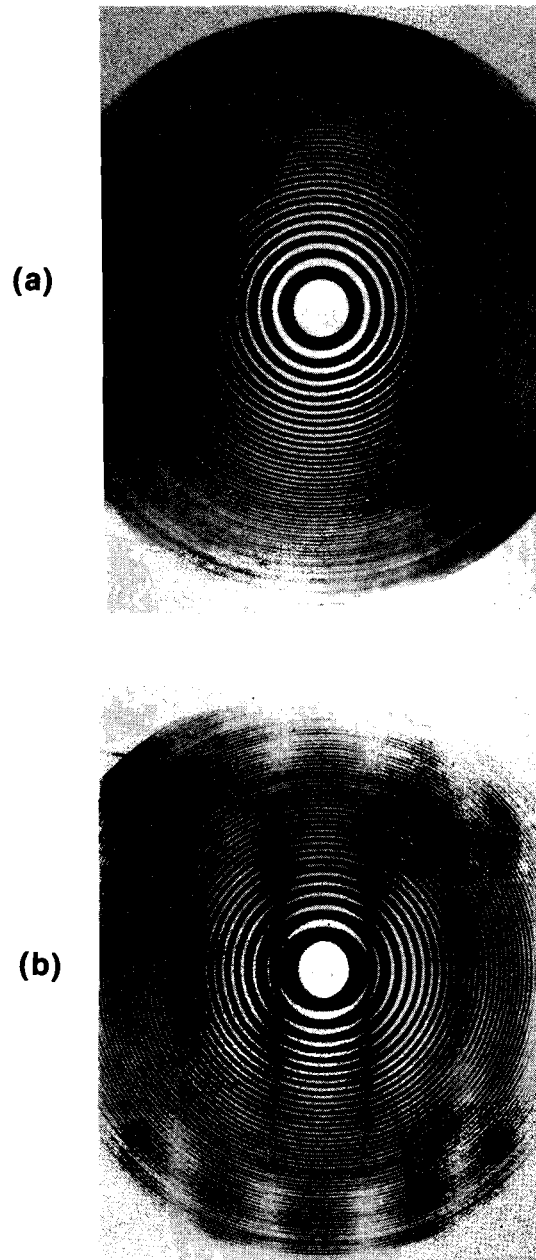


Figure 3.1  
The recording step of the pseudophotographic technique. A and B are two holes in the mask. The hole diameter is 1 mm, the separation between the centers in 3.1 mm;  $r$  is the width of the outermost zone.



**Figure 3.2**  
**Two masks used in the optical simulation experiment.**



**Figure 3.3**  
**Shadowgram of the two point sources in Figure 3.2.**  
**(a) very small separation, (b) Large separation,**  
**(photographs a & b reduced three times).**

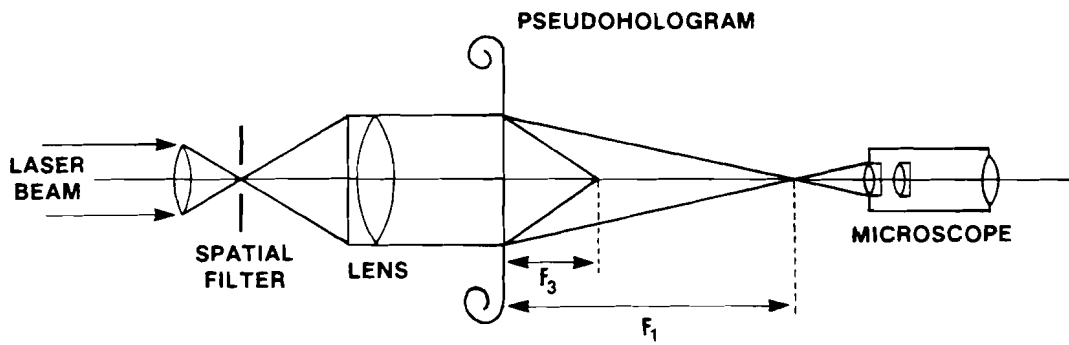


Figure 3.4  
The reconstruction step.  $F_1$ ,  $F_3$ , etc. are the first, third, etc. order foci.

mated by a lens and used to illuminate the demagnified pseudohologram. A microscope was used to look at the reconstructed image. (The distance from the zone plate to the 1st order reconstructed image was typically 30 cm). The microscope could move along the rail, allowing us to observe the different foci. The results were photographed with a Polaroid camera situated behind the eyepiece.

The improvement in resolution obtained in higher order reconstructions is demonstrated in Fig. 3.5. For the photographs the recording geometry ( $S_1 = 63.4$  cm,  $S_2 = 18.9$  cm) was chosen so that the reconstructed sources were barely resolved in the first-order reconstruction Fig. 3.5a. In Fig. 3.5c the fifth-order reconstruction shows the sources clearly resolved. The ratio of the hole diameter to the separation between the two holes in the mask is equal to that in the reconstruction in Fig. 3.5c. While fifth-order reconstruction is clearly feasible, the background light from scattering and other order reconstructions will ultimately limit the highest order reconstruction that yields a useful signal to noise ratio.

For an ideal Fresnel zone plate only odd numbered foci exist. However, for a practical zone plate there are always even numbered foci due to imperfections in the zone plate, the development process, and the shrinkage of the emulsion after development. In Fig. 3.5b the second order image is shown, in which the two point sources are resolved.

### 3.2 Limitation on the Object Size.

The moiré fringes produced by two overlapping zone plates are

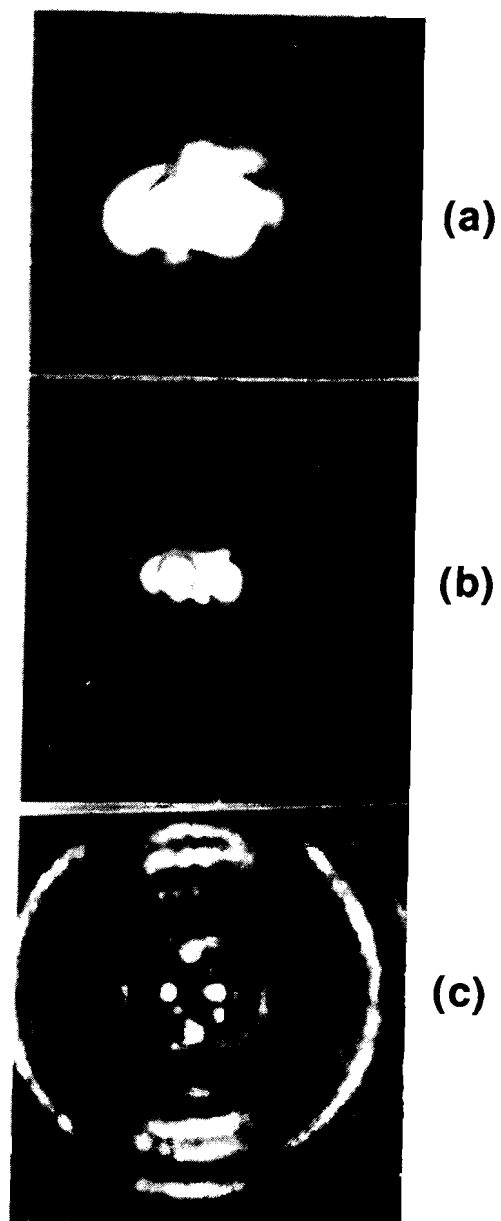


**Figure 3.5**  
Experimental results of the optical simulation experiment. Figures a, b, and c are reconstructions at the first, second and fifth order foci respectively.

shown in Fig. 3.6. When the separation exceeds the diameter of innermost zone the moiré fringes are in the form of a zone plate. The focal length of this zone plate can be calculated using the derivation in Ref. [3.2]. It is shown that for  $T > 2\xi_1$ , where  $T$  is the separation between the centers of the two zone plates and  $2\xi_1$  is the diameter of the innermost zone, we get moiré formed zone plate whose focal length is given by:  $F_M = \frac{F_{ozp}}{2}$ . In the reconstruction step light cannot distinguish between real and moiré formed zone plates and we get an additional reconstructed point in the middle. Since  $F_M = \frac{F_{ozp}}{2}$  the additional point will reconstruct only in even order reconstructions. This effect tends to decrease the signal to noise ratio in even order reconstructions. It is therefore preferable to choose a zone plate with an innermost zone that is larger than the object. In the case of pellet compression experiments the microballoon is of the order of  $70\mu\text{m}$ . In our x-ray experiments, to be described we used a zone plate with  $200\mu\text{m}$  innermost zone diameter. At higher orders the individual zones are narrower, i.e. each actual opening in the zone plate contains several zones (recall Fig. 2.1.10). The effective diameter of the innermost zone is now  $2\xi_1/\sqrt{p}$  where  $2\xi_1$  is the diameter of the actual innermost zone and  $p$  is the order number. Therefore in order to avoid spurious points at the  $2p$ th order the size of the innermost zone must be  $\sqrt{p}$  times the size of the object. In our case then the second order reconstruction will still be in the range where no artifacts should be noticeable.

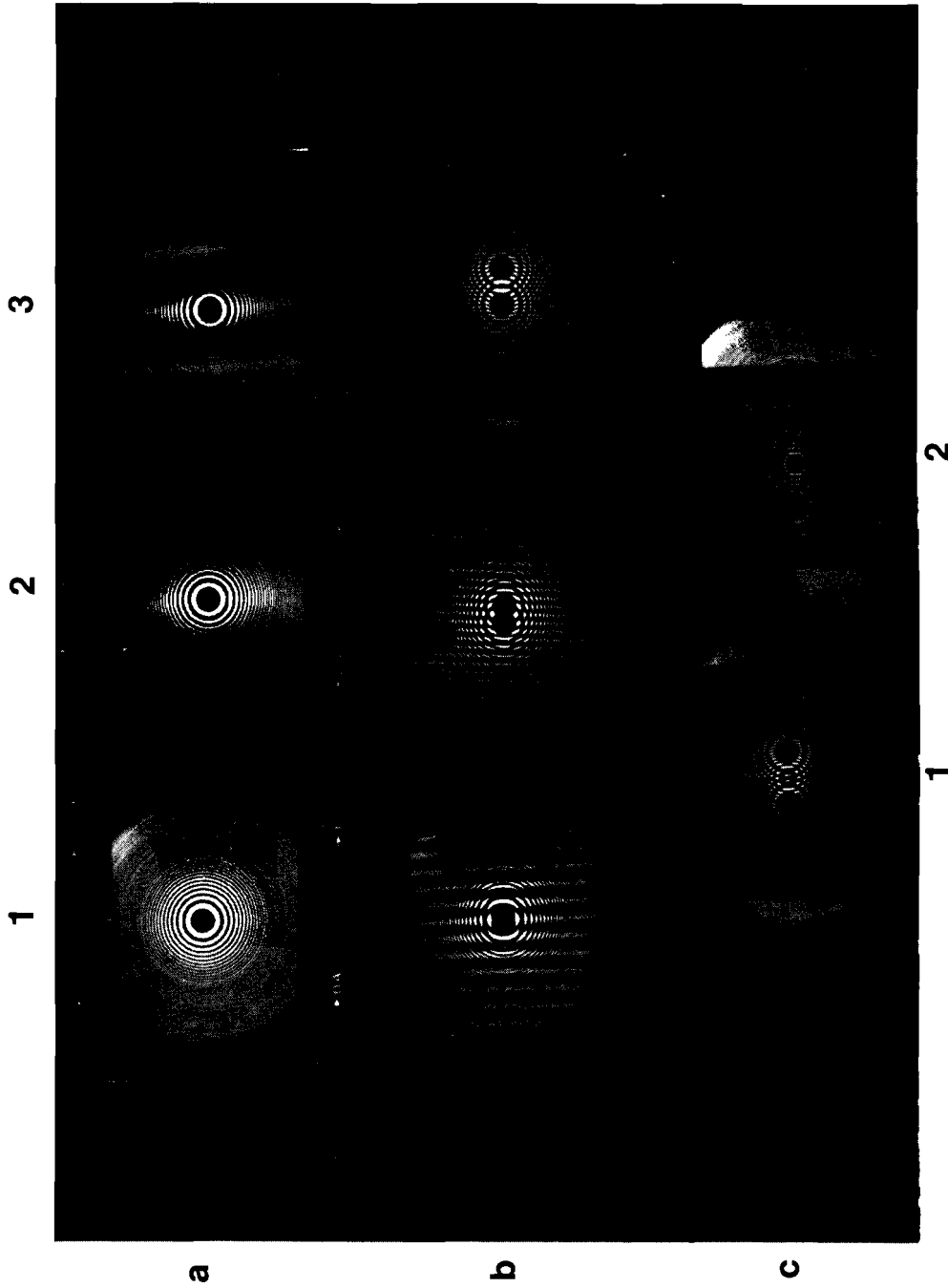


**Figure 3.6**  
**Moiré fringes produced by two overlapping zone plates: a-1 is a single zone plate. In c-1 the distance between the centers is of the order of the innermost zone diameter.**

### 3.3 Studies of the High Order Reconstructions.

Although in principle, the pseudoholographic process is a two-step process, in practice, the pseudoholographic technique used in our optical simulations was a three-step process, as described in Fig. 3.7. For the purpose of a detailed investigation of high order reconstructions we used the mask of Fig. 3.2b in step 1 of Fig. 3.7. The pseudohologram was recorded on an 8x10" tri-x piece of film in step 1 of Fig. 3.7. The pseudohologram was then reduced in step 2 in Fig. 3.7. This reduced pseudohologram was recorded on 35 mm type Kodak SO-253 film and developed using four different methods:

- (1) The film was developed in D-165 at a concentration of 1:4 for 4 min. The  $\gamma$  was in this case about 2 approximately.
- (2) The film was developed in D-19 for 6 min. The  $\gamma$  in this case was 4-5 approximately.
- (3) The center of the pseudohologram obtained in step 1 of Fig. 3.7 was blocked with a circular disc. The diameter of this disc was 1.2 times the diameter of the innermost zone recorded on the pseudohologram. The pseudohologram with the central block was then reduced in step 2 of Fig. 3.7 and developed in D-19 for 6 min. This center block has a similar effect of a DC block, as described in Ref. [3.3].
- (4) In the reduction step (step 2 in Fig. 3.7) the 35 mm film was underexposed but was developed for 6 min. in D-19. This is equivalent to developing with very low  $\gamma$ . The reduced pseudohologram thus obtained had a very low contrast.

In the reconstruction step (step 3 in Fig. 3.7) we illuminated the

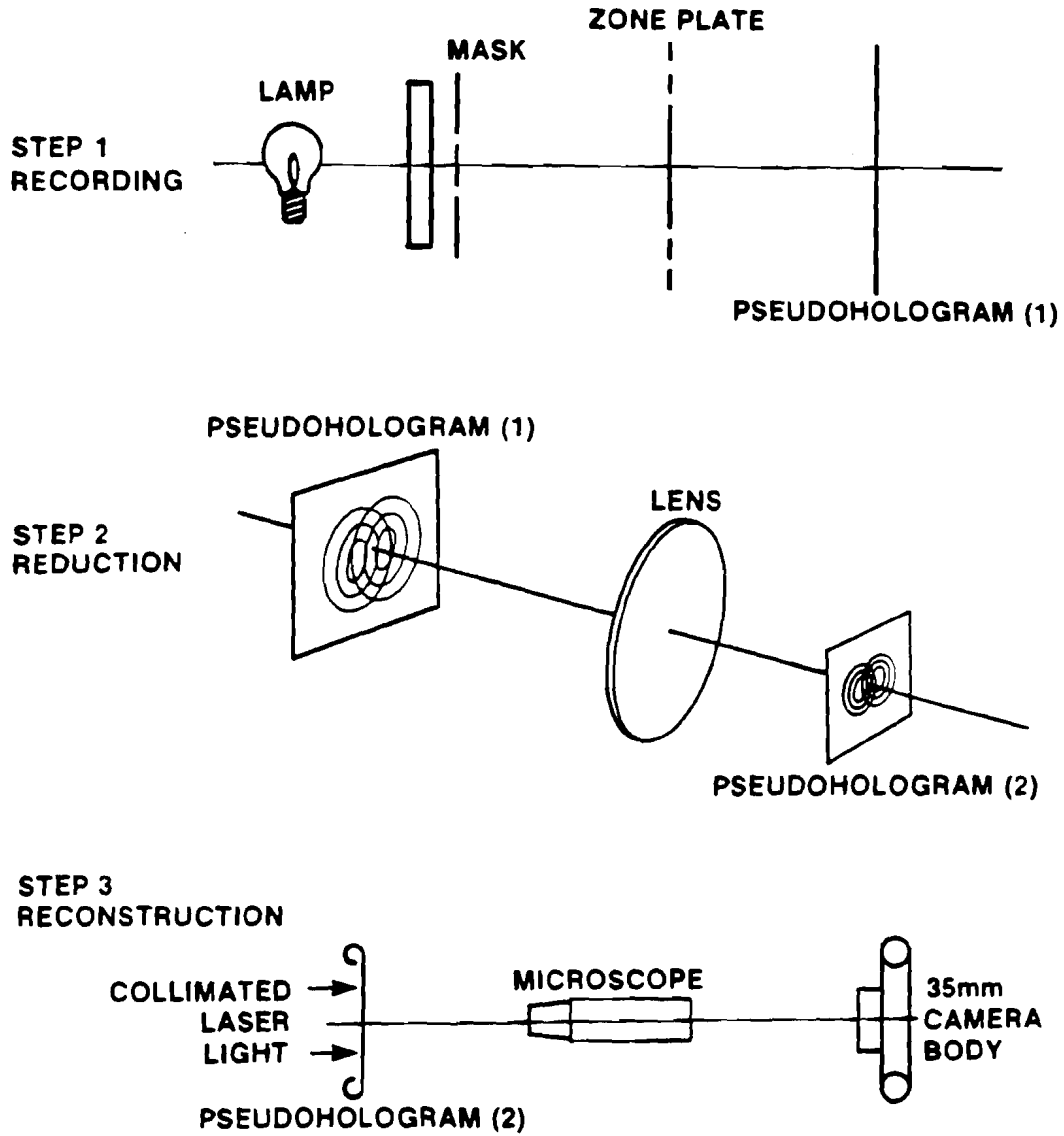


**Figure 3.7**  
Pseudoholography as a three stage process.  
1) Recording, 2) reduction of the pseudohologram, 3)  
reconstruction of the reduced pseudohologram.

reduced pseudohologram with collimated laser light. Pictures of the different order reconstructions were taken using a 35 mm camera body placed at a predetermined distance from the microscope to allow for the desired magnification.

It is worth noting that for the investigation of the effects of  $\gamma$  on high order reconstructions we should in principle take a few exposures in step 1 of Fig. 3.7. Each of these shadowgrams thus obtained should be now developed in different conditions. However, it was easier experimentally to record just one pseudohologram in step 1 of Fig. 3.7, and to do a series of different exposures in step 2 of Fig. 3.7.

### 3.3.1 Analysis of Fig. 3.8.

#### 3.3.1.1 Effects of Imperfections in the Zone Plate Mask.

Let us compare the first order reconstruction in Fig. 3.8 with the object mask, of which the pseudoholograms were made, in Fig. 3.2b. We notice that although the object is symmetric about a vertical axis the reconstructions are asymmetric. This may be attributed to imperfections in the zone plate mask itself. In Fig. 3.3b we see that the shadowgram is not symmetric about a vertical axis. The righthand side of the pseudohologram has a lower contrast than the lefthand side. We thus expect that the reconstruction will show some asymmetric features. If the contrast is reduced as in case 4 in section 3.3, there is not a real difference between the righthand and lefthand sides and therefore the first order reconstruction is symmetric in Fig. 3.8d. The asym-



metry shows up mainly in the secondary lobes in the first and second order reconstructions. At higher orders these secondary lobes are weaker and so the reconstruction of the source looks symmetric as is shown in the 6th and 7th order.

### 3.3.1.2 Artifacts.

Probably the most disturbing feature in the reconstructions in Fig. 3.8 is the existence of artifacts, which appear in all the reconstructions. We even can say that the success of the whole method depends on whether it is possible to extract information from the reconstructions without being misled by the artifacts. One way to avoid false interpretation is to notice that there is no consistency between artifacts of adjacent orders. This is clearly shown in Fig. 3.8. For example, in case b there is only one outer ring in the first order reconstruction, while three outer rings are present in the second order. Also, the third order has a different appearance than the second order. We may then argue that consistent appearance of a feature from order to order is evidence of true object content. The appearance of new feature in higher orders which could occur due to improved resolution, should be present in successive orders and should only represent subdivision of features present in lower orders.

#### 3.3.1.2.1 Comparison between the Odd and Even Order Reconstructions.

We have seen in section 3.1.1 that spurious points may be produced in the even foci when we reconstruct a pseudohologram where the separation between the centers of two zone plate shadows exceeds the diameter

of the innermost zone. This effect is not seen in the reconstructions in Fig. 3.8. The separation in the case of Fig. 3.8 was of the order of  $2\xi_1/10$  where  $2\xi_1$  is the diameter of the innermost zone and so moiré formed zone plates were not formed. Here, however, the odd foci show a strange artifact (see F/3 and F/5 in Fig. 3.8). While in F/2 the two disc source is reconstructed at F/3 there is an inner structure within each disc. This effect disappears at higher orders.

### 3.3.1.3 Effect of $\gamma$ .

Consider cases a and b in Fig. 3.8. The signal to noise ratio at high order reconstructions (8th order and up) is appreciably better in b. Hence the important conclusion that by developing the shadowgrams with high  $\gamma$  high orders are enhanced. From comparing cases a and b (10th order and up) we may conclude that high  $\gamma$  developed pseudoholograms have less speckle noise.

### 3.3.1.4 Central Block

The first order reconstruction in case c is better than in cases a and b because it is more symmetric than these two cases. However, higher order reconstructions are weaker and therefore the usefulness of this technique is limited.

### 3.3.1.5 Reconstruction at Very High Orders.

Using the high contrast pseudohologram we find that the original object is not faithfully reconstructed above 9th order, although the two points seem well resolved. Instead of reconstructing two discs

we observe two points. It is not clear why at these high orders the pseudohologram fails to reconstruct the area of the disc.

In case a at F/12 we clearly see that the speckle noise is the real limitation on the observability of the reconstruction.

### 3.3.1.6 Effects of Underexposure.

We have already noticed the enhanced symmetry in case d in the first order. Now consider the second order. Instead of two points we get one central point. In Fig. 3.9 two rings overlap each other. These overlapped rings produce a third ring with twice the density as the original ones. Therefore if the development is nonlinear, the overlapped region may be enhanced too much in comparison with the non-overlapped region. And so one set of rings will give rise to one point in the middle instead of two.

### 3.4 Requirements on the Zone Plate Camera.

We will now summarize the relevant equations and requirements from previous sections.

1. The transverse resolution,  $T_p$ , is given by:

$$T_p = \frac{1.46r}{P} \left( \frac{S_1 + S_2}{S_2} \right) \quad (3.1)$$

See Ref. [2.2.11] or Eq. (2.2.56) and related discussion in section 2.2.4. To achieve an appreciable efficiency at high orders the zone edges have to be very sharp. Also in the recording step of shadowgram

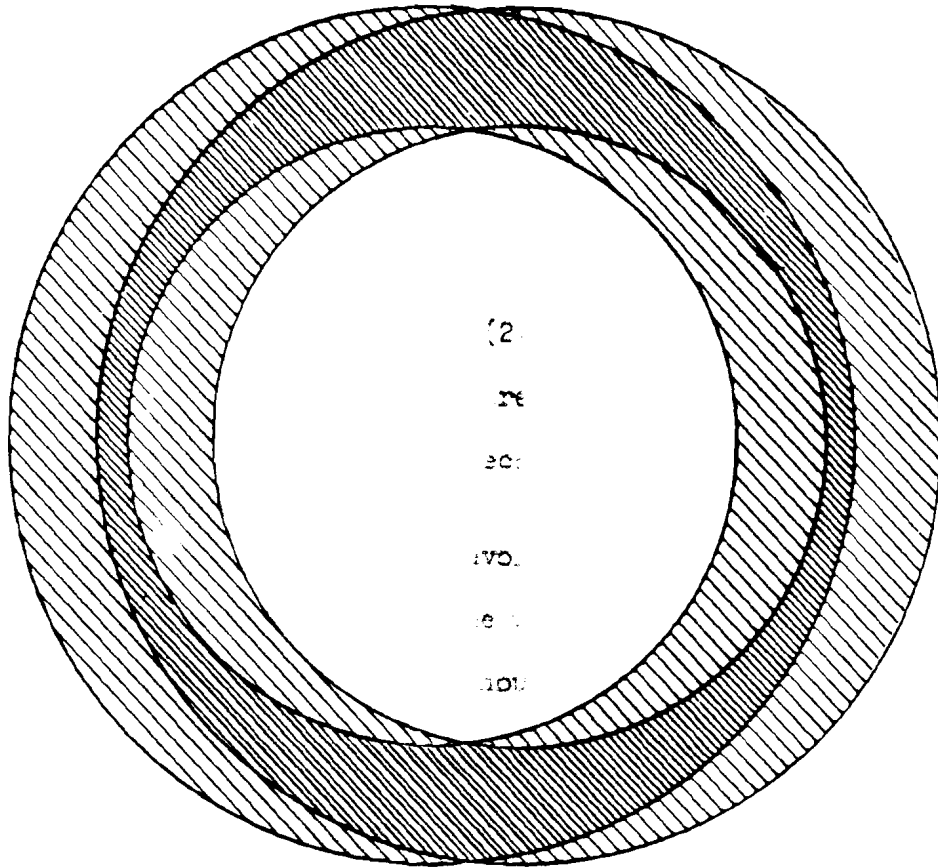


**Figure 3.9**  
**The overlap of two rings may produce a third ring.**

low

the 1, 1

dia

to

the

diffraction effects should be kept to a minimum.

2. The photographic resolution,  $L_p$ , is given by:

$$L_p = \frac{0.5}{NP} \frac{S_1}{S_2} (S_1 + S_2) \quad (3.2)$$

See Eq. (2.58) and the relating discussion in section 2.2.5. It is thus preferable to use zone plates with large number of zones and to reconstruct at higher orders.

3. The diffraction effects in the recording step of a shadowgram impose an upper limit on the wavelength which is emitted from the plasma and should be:

$$\lambda [\text{\AA}] \leq \frac{2 \cdot r^2 [\mu\text{m}^2] \cdot \mu [1/\text{cm}]}{(\Delta v)^2} \quad (3.3)$$

See Eq. (2.23) and relating discussion in section 2.2.1.

4. The lower limit for the innermost zone radius is given by:

$$r_1 \geq d \sqrt{p} \quad (3.4)$$

where  $r_1$  is the innermost zone radius,  $2d$  is the object size or the diameter of the plasma and  $2p$  is the highest order at which we will reconstruct (see discussion in section 3.2).

5. Remember that the signal to noise ratio will not decrease by more

than the amount that is predicted by Eq. (3.6) (see Ref. [3.4] page 140). The lower limit on the thickness of the gold material in which the zone plate is manufactured should be:

$$t \geq -\frac{\ln f}{\alpha(\lambda)} \quad (3.5)$$

The notation here is as follows:  $t$  is the thickness of the gold material,  $\alpha(\lambda)$  is the absorption coefficient of gold at a wavelength  $\lambda$ ,  $f$  is the transmission of the parts of the mask that should be completely opaque. Let us denote the signal to noise ratio on the pseudohologram in the case where the zone plate is made of truly opaque zones by 1. If the zones have transmission  $f$  then the signal to noise ratio decreases according to the formula:

$$\frac{1-f}{(1+f)^{\frac{1}{2}}} \quad (3.6)$$

(see Ref. [3.4]).

6. In order to avoid spherical aberration (see Ref. [2.1.15]) the upper limit on the number of zones in the zone plate mask is given by:

$$N \leq \sqrt{\frac{2F}{\lambda}} \quad (3.7)$$

$F$  is the focal length of the zone plate,  $N$  is the number of zones and  $\lambda$  is the wavelength of the coherent beam used in the reconstruction step. For  $F = 1\text{m}$  and  $\lambda = 6300\text{\AA}$  we need  $N < 1781$ . Hence in the first order

reconstruction  $N$  is not a limiting factor. However, in the 10th order reconstruction  $F_{10} = 10 \text{ cm}$  and now  $N < 563$ . Therefore  $N$  may be limiting factor only at high order reconstructions.

7. Let us denote the aspect ratio of a zone by  $\Gamma$  and define it by

$$\Gamma = \frac{\text{thickness of zone}}{\text{width of zone}}$$

In Fig. 3.10 we illustrate a few of the problems that may be introduced by high aspect ratio zones in an x-ray zone plate fabricated in gold:

- (1) Rays may pass through the gold material partially attenuated and give rise to false information.
- (2) Ray may be reflected and scattered from the channel walls in the open zones.
- (3) The effective beam width changes and this may cause diffraction effects.

Let us define the  $F/\#$  of a zone plate by

$$F/\# = S_1/2\xi_N$$

where  $S_1$  is the distance of the zone plate from the source, and  $2\xi_N$  is the diameter of the zone plate. To minimize the effects that are mentioned above we should have

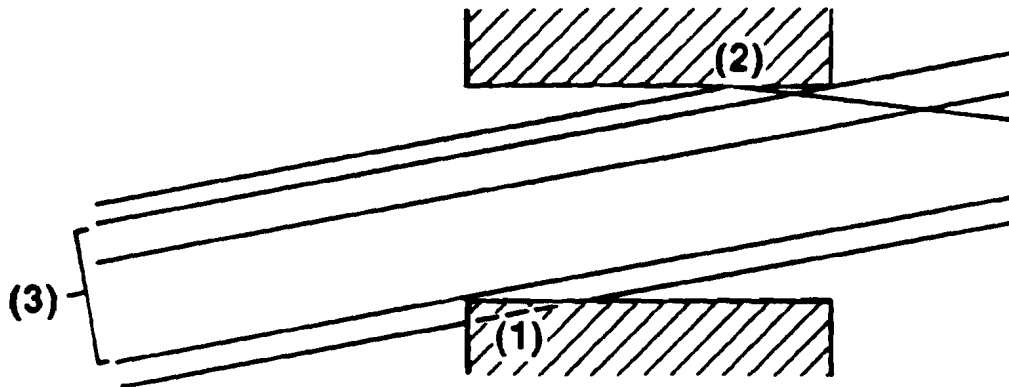


**Figure 3.10**

**Effects of high aspect ratios.**

**(1) A ray passes through the wall, (2) rays reflect and scatter from the walls, (3) effective beam width gets smaller.**

$$\Gamma < \frac{f/\#}{5} \quad (3.8)$$

or

$$\frac{t}{r} \leq \frac{1}{10} \frac{S_1}{\xi_N} \quad (3.9)$$

where  $t$  is the thickness of the gold material and  $r$  is the width of the outermost zone (see Ref. [3.4]).

8. The magnification must be such that the grain size of the x-ray film will be smaller than the smallest magnified detail. If the smallest detail we are interested in is of the order of  $1\mu\text{m}$ , and the grain size is of the order of  $10\mu\text{m}$  we thus need at least a 10x magnification.

### 3.5 Calculation of the Zone Plate Parameters for X-Ray Pseudoholography of Pellet Compression Experiments.

Some typical spectra which are emitted from compressed microballoons are shown in Ref. [3.5] and [3.6]. From these figures we can conclude that most of the radiation is in a region  $8 - 3.5\text{\AA}$  with a weaker continuum extending to well below  $1\text{\AA}$ . When more powerful lasers will be used the spectrum will change and will contain larger amount of hard x-rays. In our case however a  $5\mu\text{m}$  thickness was chosen, which corresponds to a decrease of 15% in signal to noise ratio according to Eq. (3.5) for a wavelength of  $1.4\text{\AA}$  (see Table 3.1). Since the aspect ratio should not exceed 1 (from (3.9) using  $S_1 = 10 \text{ mm}$ ;  $\xi_N = 1 \text{ mm}$ ) then

Table 3.1: Attenuation of X-Rays in Different Thicknesses of Gold Foils

$\lambda$ [Å]	$\lambda$ [KEV]	$\sigma = \frac{\alpha}{\rho}$ [cm <sup>2</sup> ]	$\rho$ [gr/cc]	$\alpha = \sigma \rho$ [1/cm]
1.4	8.6	208	19.3	4014.4
0.7	17.4	111	19.3	2142.3

$\lambda$ [Å]	$I_0/I$	$\ln I_0/I$	$\alpha$ [1/cm]	$x = \ln(I_0/I)/\alpha$ [μm]
1.4	100	4.6	4014.4	11.4
1.4	10	2.3	4014.4	5.7
1.4	5	1.6	4014.4	4
0.7	100	4.6	2142.3	21.4
0.7	10	2.3	2142.3	10.7
0.7	5	1.6	2142.3	7

$$r = 5\mu\text{m by (3.9)}$$

According to Eq. (3.3) and Ref [2.2.7] diffraction effects will not be severe if  $\lambda \leq 5\text{\AA}$  and  $r \sim 5\mu\text{m}$ .

The size of the microballoon is typically  $80\mu\text{m}$  and so according to Eq. (3.4) we need for 4th order reconstructions  $\xi_1 > 112\mu\text{m}$  or  $225\mu\text{m}$  diameter innermost zone. From Eq. (2.2.14) we find:

$$\xi_1 = 2r\sqrt{N} \Rightarrow N = (\xi_1/2r)^2 = (112/10)^2 = 125 . \text{ According to Eq. (3.7)}$$

this is acceptable for 1st, 2nd, 3rd, 4th and 5th order reconstructions.

In our case we use a Buckbee Mears\* zone plate which has 37 zones. The innermost zone diameter is  $200\mu\text{m}$ . The outermost zone is calculated to be  $8\mu\text{m}$ . However, the actual width is about  $1-2\mu\text{m}$ . The openings are thus much narrower than the expected values calculated according to  $\sqrt{N_{\text{ZONE}}}$  formula for the zone plate. Finally the magnification was chosen to be  $S_2/S_1 = 16$  and therefore according to Eq. (3.1)  $\frac{S_1+S_2}{S_2} = 1$  and the resolution is given by  $T_p = \frac{1.46r}{p}$ .

### 3.6 The Construction of the Zone Plate Camera.

A description of the zone plate camera is shown in Fig. 3.11a and in Table 3.2. The carousel housing (1) is a light tight box which contains a six-sided carousel (7). A piece of x-ray film can be mounted on each side of the carousel (9). The carousel can be rotated by a stepper motor. The stepper motor is situated inside the carousel. A

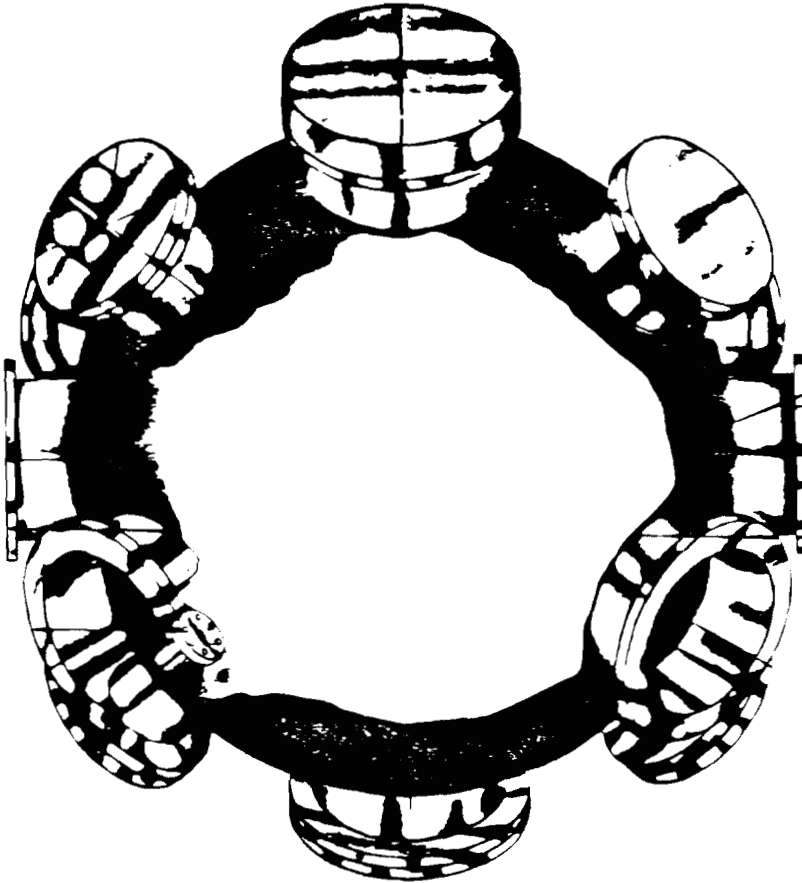
\*Buckbee Mears, Inc., St. Paul, MN.



Table 3.2: Explanations to Fig. 3.11a

PART #	EXPLANATION	PART #	EXPLANATION
①	Carousel Housing	⑫	Cover Plate
②	Bushing Guide	⑬	Right Gusset
③	Cone Aperture	⑭	Left Gusset
④	Guiding Arm	⑮	"X" Slide
⑤	Vacuum Flange	⑯	Worm Mount PIC#Q8-1 64P Worm
⑥	Guiding Arm	⑰	Worm Mount PIC#Q8-1 64P Worm
⑦	Flexible Cable	⑱	"Y" Slide, Gear PIC#Q7-14
⑧	Plate A-apter	⑲	"Z" Slide, Velmex #A25046
⑨	Flange Feedthru	⑳	Plate Mount "Z" Slide
⑩	Carousel	㉑	Flange, Seal "Z" Slide
⑪	Shutter Release Clamp	㉒	Feedthru -- Electrical
⑫	Film Plane	㉓	Block Spacer "Y" Slide
⑬	Bearing		
⑭	Filter (Vent)		

cone aperture (2) is mounted on the carousel housing. The carousel housing is mounted on a plate adapter (5). The plate adapter is connected to three turning knobs on a vacuum flange (3) by two telescopic joints and a slide (23). Such a configuration permits a three axis motion of the camera head (carousel housing). The vacuum flange is mounted on a vacuum tank (see a diagram of the tank in Fig. 3.11b). The vacuum tank has several ports. Four of these contain f/1.4 lenses that focus the laser beams on the microballoon target. The other ports contain various diagnostics instruments. The microballoon targets are mounted on a special fixture which places the microballoon at the center of the tank. To prevent interfering with the target illuminating beams, the target mounting fixture and the various diagnostics instruments, the camera aperture size is set to be 8 mm. The outer diameter of the carousel housing is set to be 140 mm which is a bit smaller than the 6" tank port diameter (142 mm). The zone plate used in the experiment was manufactured by Buckbee Mears, St. Paul, MN. It is a free standing zone plate (see Fig. 3.12(5) and 3.13) made in 5 $\mu$ m thick gold foil. The zone plate was centered on a 6 mm in diameter Be disc 25 $\mu$ m thick. The Be foil was placed on the cone's tip, and aligned in such a way that the center of the zone plate would coincide with the optical axis. A shutter release is used for aligning the zone plate camera. The shutter release clamp (8) is mounted on the carousel housing (1). A 40 $\mu$ m diameter needle is glued to the tip of the pin of the shutter release. The flexible cable (4) is connected to a knob on the vacuum flange. To align the camera the knob is turned all the way and the cable moves forward until the tip of the needle reaches the optical axis 8 mm from the zone plate.



**Figure 3.11b**  
**Diagram of the DELTA tank including the various ports.**

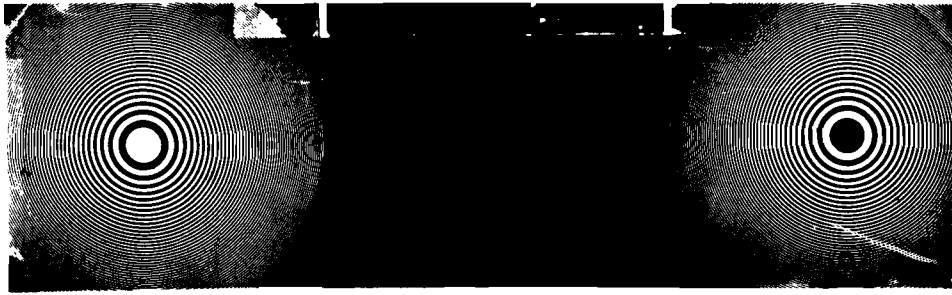
The camera can now be moved with the appropriate knobs until the tip of the needle coincides with the center of the microballoon.

### 3.6.1 The Zone Plate Used in the X-Ray Experiments.

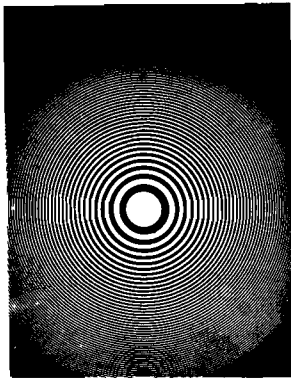
In Fig. 3.12 we show five zone plate masters. The parameters of these zone plates are listed in Table 3.3. The experiments reported here were done using zone plate #5 in Fig. 3.12. The actual zone plate is shown in Fig. 3.13. It is a free standing zone plate made in  $5\mu\text{m}$  thick gold foil. Unfortunately, the zone plate was damaged, as can be seen in Fig. 3.13. Another deficiency of this zone plate is shown in Fig. 3.13b. The outer zones are extremely narrow. They are on the order of  $1\text{-}2\mu\text{m}$  instead of being  $5.3\mu\text{m}$  wide, as designed by the manufacturer. This is due to manufacturing problems. Such narrow zones as in Fig. 3.3c will cause diffraction and hence limit the usefulness of the zone plate. Also the defects in the zone plate will cause artifacts and lower the signal to noise ratio of the reconstructions. In spite of all these difficulties, it is remarkable that we were able to get reconstructions even at third order.

We note that the innermost zone is opaque. This will cause the pseudohologram to have a clear center. When we reconstruct, the reconstructed object will be superimposed on this bright background. We thus have to copy the pseudohologram on to another piece of film. We can save this step either by using a zone plate with clear center (such as #2 in Fig. 3.12) or by bleaching the pseudohologram.

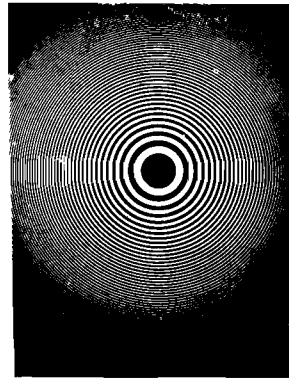
In Fig. 3.14 the actual camera is shown. (a) is a general view of the camera. In (b) the six-sided carousel is shown as well as the



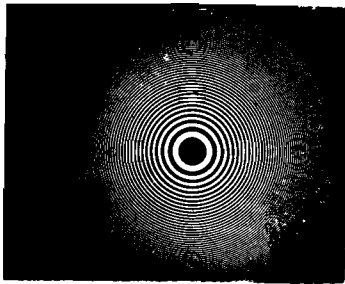
(1)



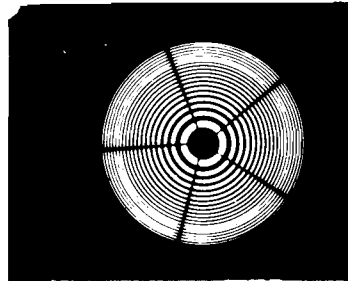
(2)



(3)



(4)

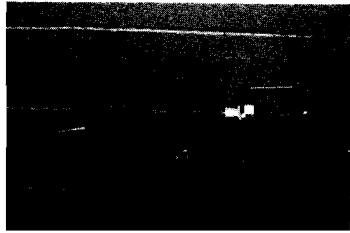


(5)

**Figure 3.12**  
**Zone plate masters (the parameters are given in table 3.3).**  
**Magnification about 20x.**

Table 3.3: Parameters of the Zone Plate Masters, shown in Fig. 3.12

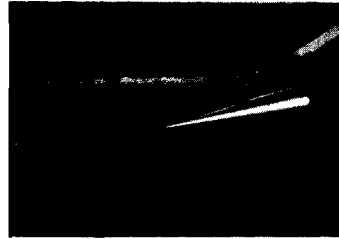
<u>Number</u>	<u># of Zone Plates on Master</u>	<u>Outer Diameter of Zone Plates (mm)</u>	<u>Innermost Zone Diameter (<math>\mu\text{m}</math>)</u>	<u>Outermost Zone Width (<math>\mu\text{m}</math>)</u>	<u># of Zones</u>	<u>Clear or Opaque Center</u>	<u>Source</u>
1	2	2.25	215	5.3	100	1 black, 1 clear	RCA and Photographic Sciences
2	1	2.25	215	5.3	100	clear	"
3	1	2.25	215	5.3	100	black	"
4	1	1.75	175	4.3	100	black	"
5	1	1.25	200	8.1 (theory) 5.3 (practice)	3	black	Buckbee Mears



(a)



(b)



(c)

**Figure 3.14**  
**The zone plate camera. (a) General view, (b) the six-sided carousel, (c) the alignment pin**

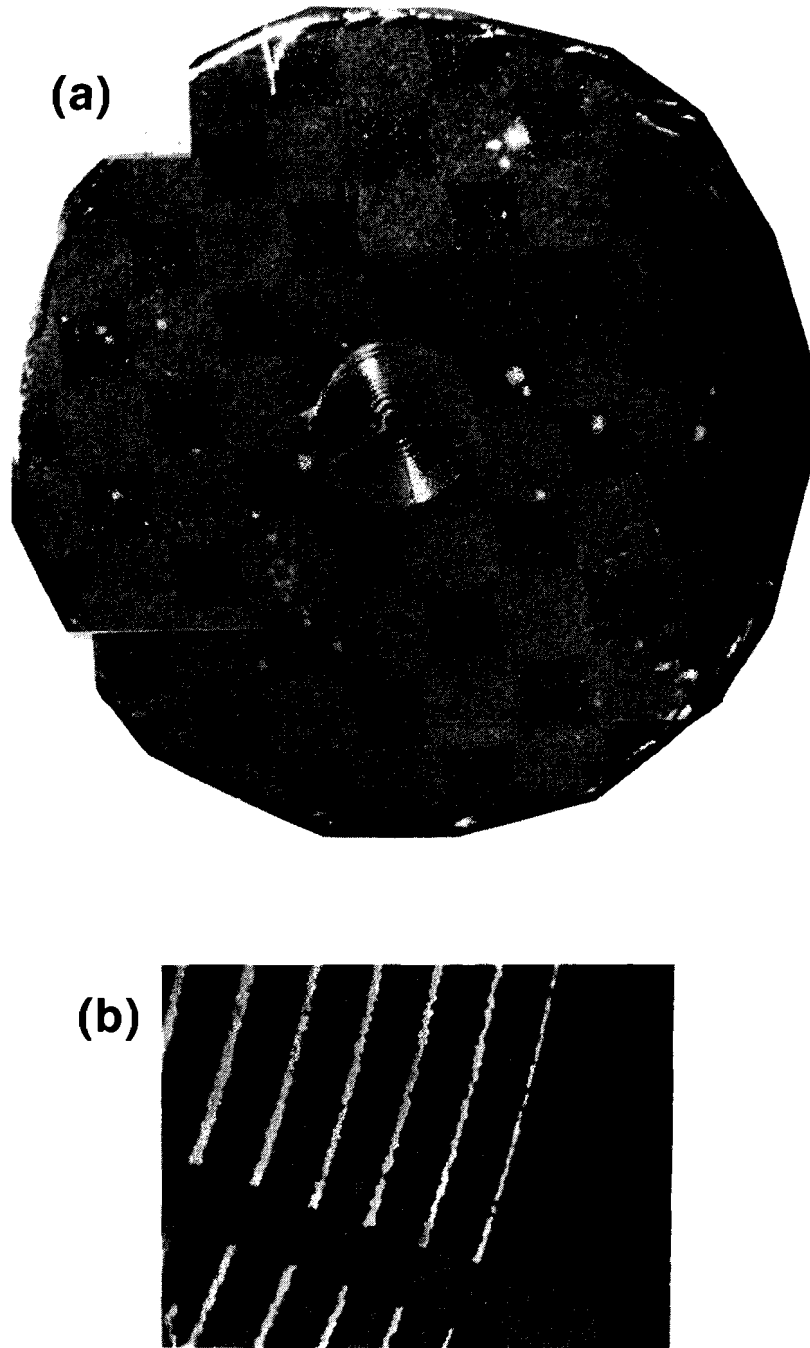


**Figure 3.13**

(a) The Buckbee Mears zone plate is glued to a Be foil, to be mounted on the zone plate camera. (Magnification is about 100x.) (b) Combined reflection and transmission picture of the outer region of the Buckbee Mears free standing zone plate. The narrow opening is a result of fabrication problems. (Magnification is about 500x.)

conical aperture. The aligning pin is shown in (c).

### 3.6.2 Sensitivity of the Zone Plate Camera to Misalignment.

Fig. 3.15 is used to illustrate the sensitivity of the instrument to misalignment. If the microballoon is shifted a distance  $\delta$ , then the shadowgram will shift a distance  $\delta' = \delta \frac{S_2}{S_1}$ .  $\delta$  is typically not larger than 100 $\mu$ m and  $S_2/S_1 = 16$ . Therefore  $\delta' \leq 1.6$ mm. The size of the pseudohologram is given by:  $2A' = (2A+D) \frac{S_2}{S_1} + 2A$  for a mask of 1.25mm and  $S_2/S_1 = 16$ ;  $2A' \sim 20$ mm. Each side of the carousel in Fig. 3.11 is about 5 cm long, therefore the zone plate camera is not sensitive to movement of the microballoon.

### 3.7 The Problem of the Destruction of the Zone Plate by Extremely High Intensities in Laser Fusion Research.

The experiments to be reported in this work were done on the Delta system in the University of Rochester. The energy delivered by this laser was typically 7 - 10 joules in about 30 - 100 psec. With this system there is no problem placing the zone plate 1 cm from the target. However, the proposed Omega system, which will have 24 beams, will deliver  $10^4$  joules in about 1 nsec. If a zone plate 2 mm in diameter will be placed 1 cm from the target, the amount of energy incident on it will probably be  $500\text{J}/\text{cm}^2$  which is an enormous amount of energy considering most of it will be absorbed by a 25 - 75 $\mu$ m thick foil of Beryllium on which the zone plate is deposited. An obvious way to overcome this problem is to work on a single shot basis, namely, to replace the zone plate after every shot. The fabrication procedure of a zone

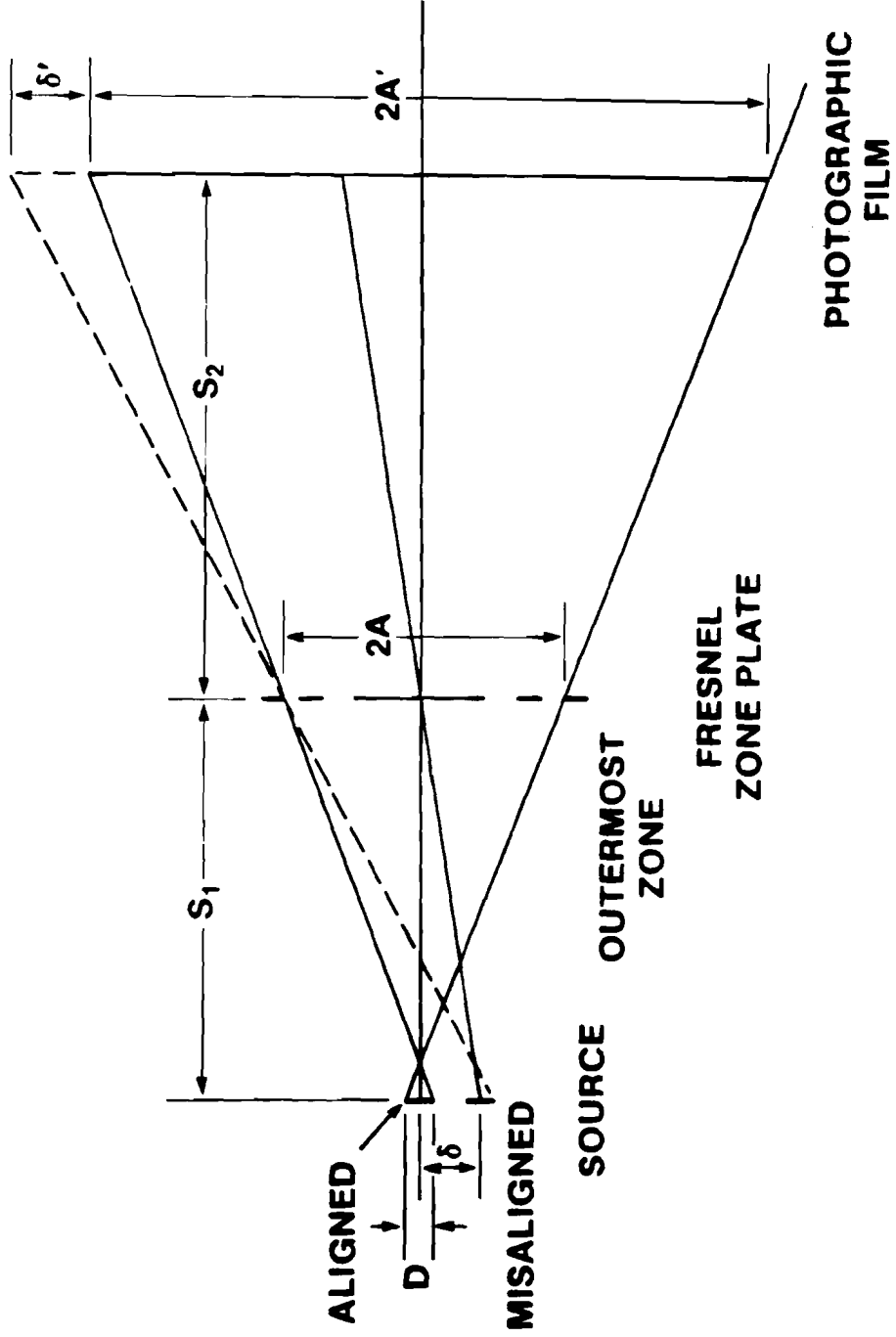


Figure 3.15  
Illustration for computing the sensitivity of the zone plate camera to motion of the microballoon.

plate can be made efficient and relatively inexpensive so that this mode of operation seems feasible. Another solution is to place the zone plate further away, say 10 cm, from the target. This will force us to use under outermost zones (of the order of  $10\mu\text{m}$ ) and decrease the resolution. With hard x-ray radiation 5th order reconstructions may still be feasible so that  $2\text{-}3\mu\text{m}$  resolution can be achieved.

Furthermore, if optical deconvolution or hybrid optical digital deconvolution procedures are developed, we should still get high resolution even with the zone plate placed at distances larger than 1cm from the target.

### 3.8 The Resolution of the System.

To determine the resolution of the instrument we used a mesh\* of  $5\mu\text{m}$  square holes separated by  $20\mu\text{m}$  (see Fig. 3.16d). Instead of a diffuse source we placed the mesh as close as possible to an x-ray source. In Fig. 3.17a we see the configuration used in this experiment and how a broad source can be used, as long as the mesh is placed close enough to the source. We used an x-ray machine which emits Iron  $K\alpha$  line radiation and produces a line source 15 mm by 1 mm. The resultant pseudohologram is shown in Fig. 3.16a. In spite of the fact that the source was too narrow in one direction and that the radiation was too hard for the thickness of the gold material, we were able to reconstruct the mesh. In Fig. 3.16b the first order reconstruction is shown. The distance between the holes is  $20\mu\text{m}$  and the reconstructed

\*The mesh was supplied by Perforated Products, Inc., Newton, Mass.

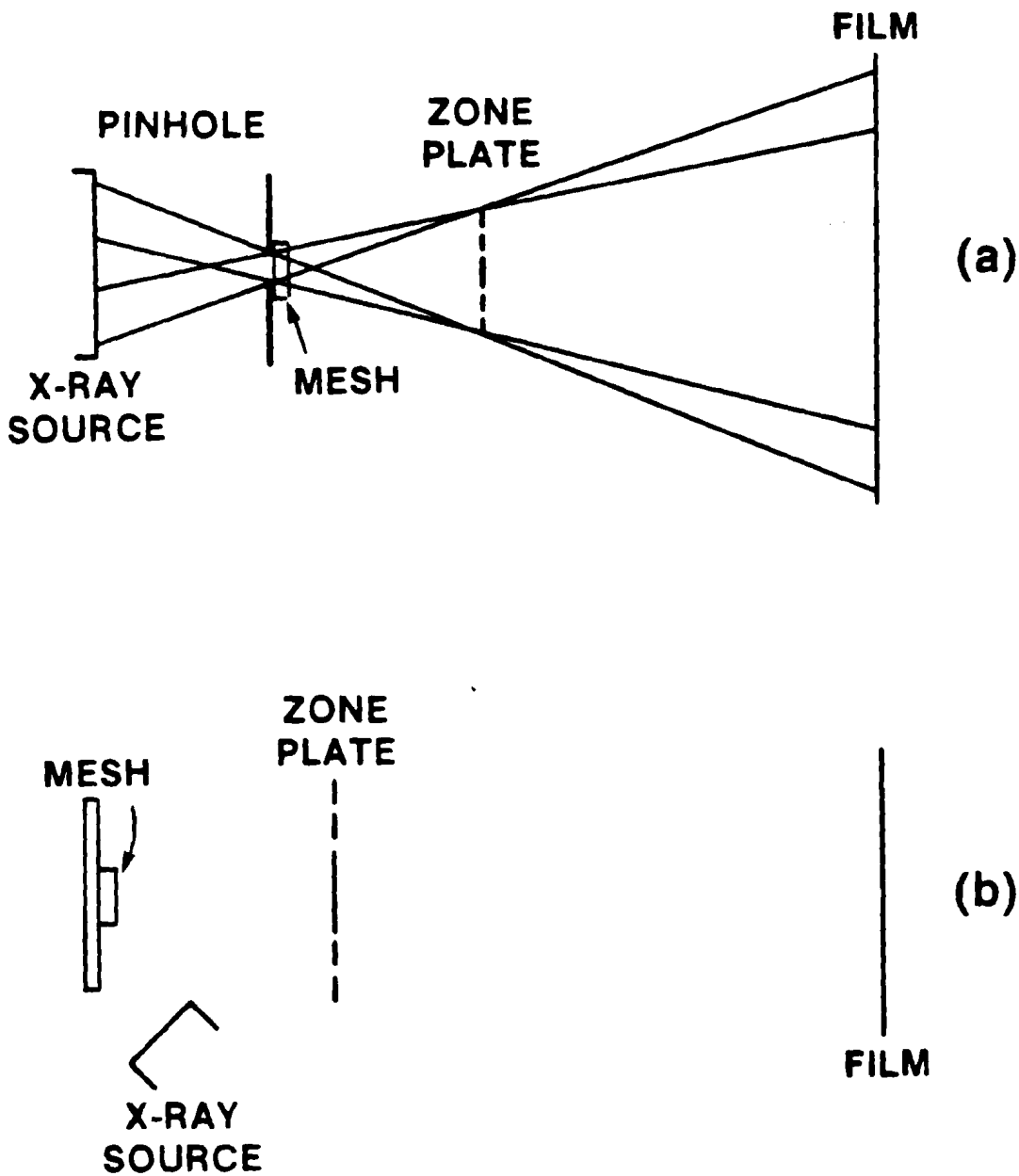


Figure 3.17

Configurations for performing the resolution test.

(a)-Transmission method, (b) fluorescence method:  
the nickel in mesh fluoresces when x-rays are incident  
on it.

hole width seems to be about  $10\mu\text{m}$ , as shown in Fig. 3.16b. Taking into account that the holes are  $5\mu\text{m}$  wide, we may conclude that the resolution is about  $8\mu\text{m}$  in the first order. In Fig. 3.13c we see the reconstruction at the second order. The signal to noise ratio is too low and most of the holes are not reconstructed. However, 2 lines seem to be reconstructed.

### 3.9 Experimental Results from Laser Pellet Compression Experiments.

#### 3.9.1 Experimental Determination of the Magnification of the Camera.

In Table 3.4 we list the parameters of seven shots which were done on Delta. The reconstructions are shown in Fig. 3.19 to Fig. 3.23. In order to determine the magnification the diameter of the zone plate and the diameter of the shadowgram were measured. In Fig. 3.18 we show the relationship between the zone plate diameter, the pseudohologram diameter, and the magnification. Let  $D_z$  and  $D_{ps}$  be the diameters of the zone plate and the pseudohologram respectively. Let's assume that we have a two point source and the two points are separated by the distance  $T$ . The distance between the centers of the corresponding zone plate shadows on the film is  $T'$ . By measuring  $D_{ps}$  and  $D_z$  we get the ratio  $T'/T$ .

From Fig. 3.18 we have the following relationships.

$$\frac{\overline{BF}}{\overline{GH}} = \frac{\overline{AE}}{\overline{GH}} = \frac{S_2 + S_1}{S_1} \quad (3.10)$$

$$\overline{AB} = \overline{CD} = \overline{EF} \quad (3.11)$$

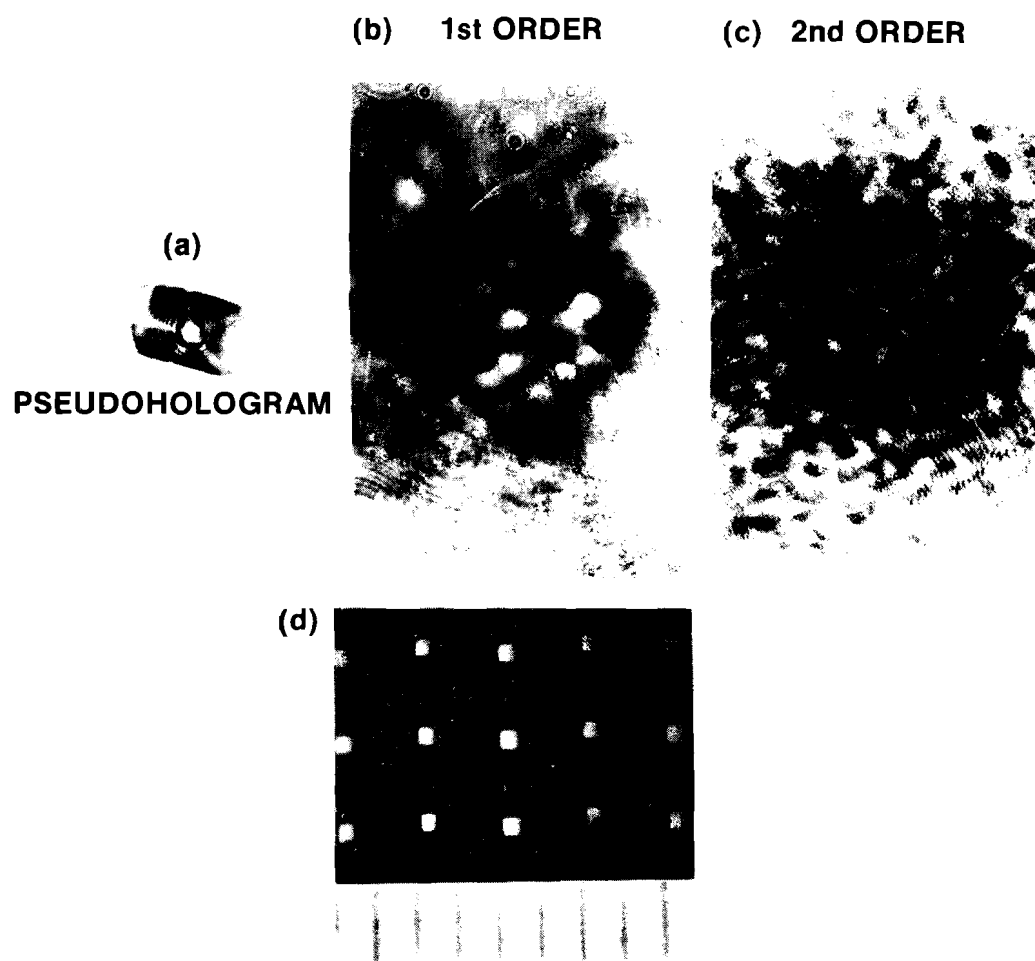


**Figure 3.16**  
**Resolution test for the zone plate camera.**  
(a) Pseudohologram of the mesh, (b) first order reconstruction,  
(c) 2nd order reconstruction, (d) the mesh. Scale 10  $\mu\text{m}/\text{div}$ .

Table 3.4: Parameters of the Shots Taken on Delta

Shot #	Target #	Gas or Material (for CD <sub>2</sub> )	Pressure (At.) or Density (gr/cc)	Wall Thickness (μm)	Micro Balloon Diameter (μm)	Energy on Target (joules)	# of Be Foils <sup>†</sup>	# of Beams	Notes	Fig. #
1	17691	2419	unknown	.728	67	2.135	1	4	---	3.19
2	17692	2406	Ne	.746	64.7	9.77	1	4	(1)	3.20
3	17735	stalk	---	---	70.	6.96	2	4	---	3.20
4	17737	2310	Ne	.69	67	6.38	2	4	---	3.21
5	17758	2516	CD <sub>2</sub>	---	96.	4.4	4	4	---	3.22
6	17759	2525	CD <sub>2</sub>	---	87.	5.3	4	4	(2)	3.23
7	17760	2499	CD <sub>2</sub>	---	60.	5.2	4	4	(2)	3.23

Notes: (1) 500 Å Au coat (bleached)

(2) exposed on the same pseudo-hologram

<sup>†</sup>Footnote: each 25 μm thick

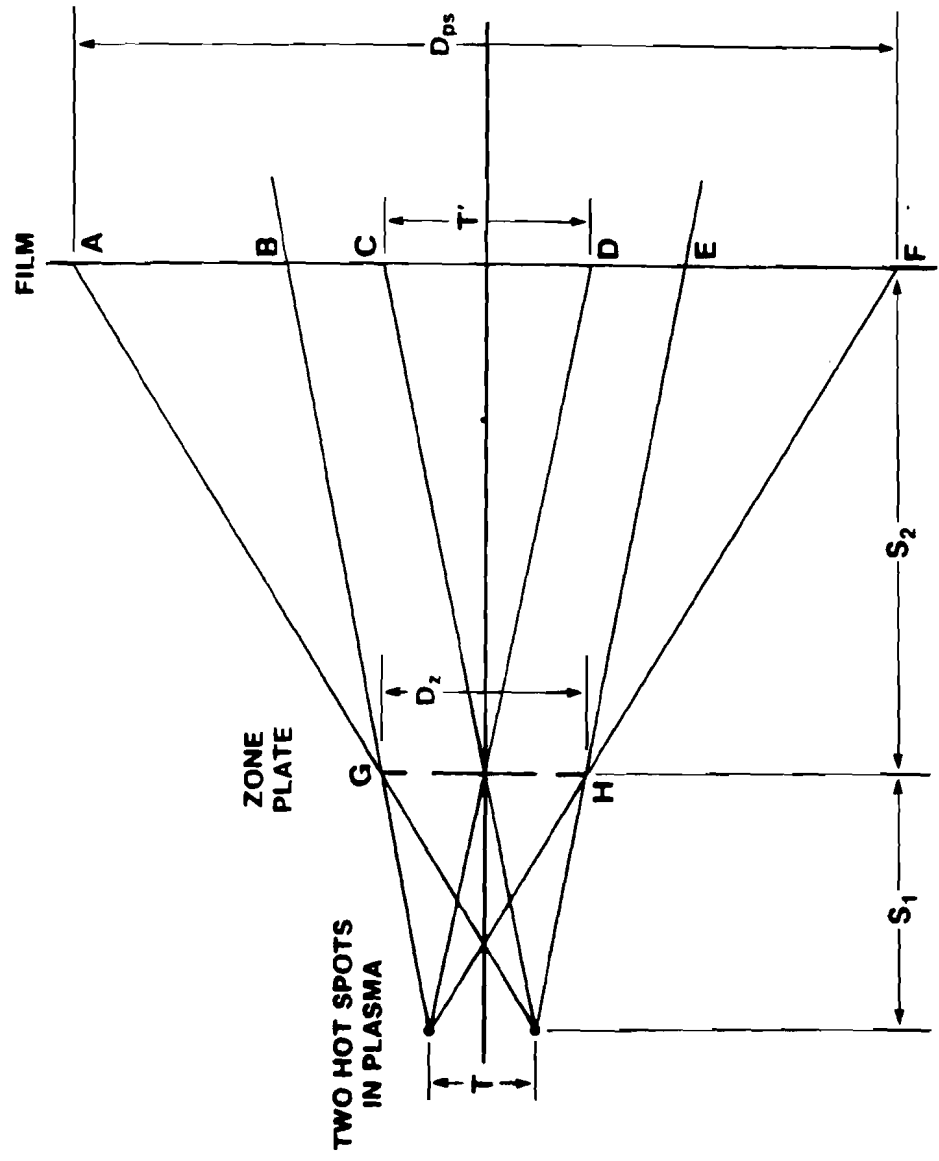


Figure 3.18  
Illustration for computing the magnification of the zone plate camera. The shadowgram in this case is the two overlapped zone plates.

$$D_{ps} = \overline{AE} + \overline{EF} \quad (3.12)$$

from (3.10)

$$D_{ps} = \overline{GH} \left( \frac{S_2 + S_1}{S_1} \right) + \overline{EF} \quad (3.13)$$

$$\text{CZ} \quad D_{ps} = D_z \left( \frac{S_2 + S_1}{S_1} \right) + \overline{EF} \quad (3.14)$$

$$\text{now} \quad T'/T = S_2/S_1 \quad (3.15)$$

$$\text{from (3.15)} \quad D_{ps} = D_z \left( \frac{S_2}{S_1} + 1 \right) + \overline{EF} \quad (3.16)$$

$$\text{hence} \quad \frac{S_2}{S_1} = \frac{D_{ps} - \overline{EF}}{D_z} - 1 \quad (3.17)$$

By measuring  $D_{ps}$ ,  $\overline{EF}$  and  $D_z$  we thus find  $S_2/S_1$ .

The microballoon is mounted on a glass stalk which is typically 70 $\mu$ m diameter. (See Fig. 3.24b). When the laser beams hit the microballoon we expect the emission to occur from the shell as well as from the compressed core in the center. On the other hand if the laser beams hit the stalk from opposite sides we expect emission to occur only from the surface of the stalk. The density of the stalk is so high that compression cannot occur. The stalk case is therefore suitable for measuring the exact magnification since we have two hot spots in the plasma as is required in Fig. 3.18. We thus use the results from

the stalk shot shown in Fig. 3.20 (shot #17735). Measuring  $D_{ps}$  and  $\overline{EF}$  we get:

$$D_{ps} = 2.05 \text{ cm}, \quad \overline{EF} = 0.1 \text{ cm}, \quad Dz = 0.12 \text{ cm}$$

$$\text{Therefore, } \eta = T'/T = S_1/S_2 = \frac{2.05 - 0.1}{0.12} - 1 = 15.25 \quad (3.9)$$

In most cases we demagnify the pseudohologram; in our case  $1/m = 1/2$ . We used a Niromat camera fitted with a Nikon 55mm f/5.3 Macro lens.

$$\eta = T'/T = \frac{15.25}{2} = 7.625$$

The error in  $\eta$

$$\frac{\Delta\eta}{\eta} = \frac{\Delta(D_{ps} - \overline{EF})}{D_{ps} - \overline{EF}} + \frac{\Delta Dz}{Dz} + \frac{\Delta m}{m}$$

We estimate the errors as follows:

$$\frac{\Delta m}{m} = 7\% \quad (\text{due to error in setting up the camera})$$

$$\frac{\Delta Dz}{Dz} = 0.5\%$$

$$\frac{\Delta(D_{ps} - \overline{EF})}{D_{ps} - \overline{EF}} = 2.5\%$$

Therefore  $\frac{\Delta\eta}{\eta} = 10\%$  when reduction with the camera has taken place,  
 $\frac{\Delta\eta}{\eta} = 3\%$  without reduction.

The reconstructions were done using the same system described in section 3.1.

### 3.9.2 Discussion of the results.

The increase of resolution in higher orders is demonstrated in Fig. 3.19. In the first order we distinguish between the shell on the outside and the core. This is consistent with experimental configuration shown in Fig. 3.24a. The camera is in the plane of the four beams and is situated at  $45^\circ$  to two of the beams. Therefore, the shell will consist of two regions where the right and left beams hit the pellet. The width of the shell at the first order is about  $8\mu\text{m}$ . In the second order it is only  $4\mu\text{m}$  and in the third, it is  $2-3\mu\text{m}$ . The fine structure shown in the second order is consistent with that in the 3rd order. This suggests according to previous discussion, that this fine structure is real. This means that as the material compresses inward, it is heated and it emits radiation.

The actual size of the core is about  $3\mu\text{m}$  according to the third order and not about  $10\mu\text{m}$  as it might seem from the first order. The gas in this microballoon and its pressure were unknown in this case.

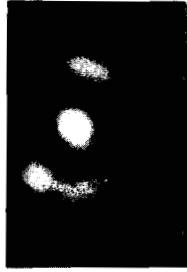
In Fig. 3.20 (shot #17692), the case of gold coated microballoon is shown. In this case the energy on target was high and the pseudohologram was overexposed. It was not possible to reconstruct with this hologram. This pseudohologram was then bleached. The x-ray film is very thick so that by bleaching we got a white patch due to the scattering in the bleached silver halide. It was not possible to reconstruct this pseudohologram either. The bleached hologram was then

**PSEUDO**

**HOLOGRAM**

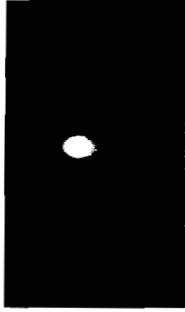


**1st ORDER**



50  $\mu\text{m}$

**2nd ORDER**



50  $\mu\text{m}$

**3rd ORDER**



50  $\mu\text{m}$

**SHOT #**  
**17691**

**Figure 3.19**  
**Reconstruction of a microballoon. Unknown gas fill and pressure. Compression is shown.**  
**First, second and third order reconstructions shown.**

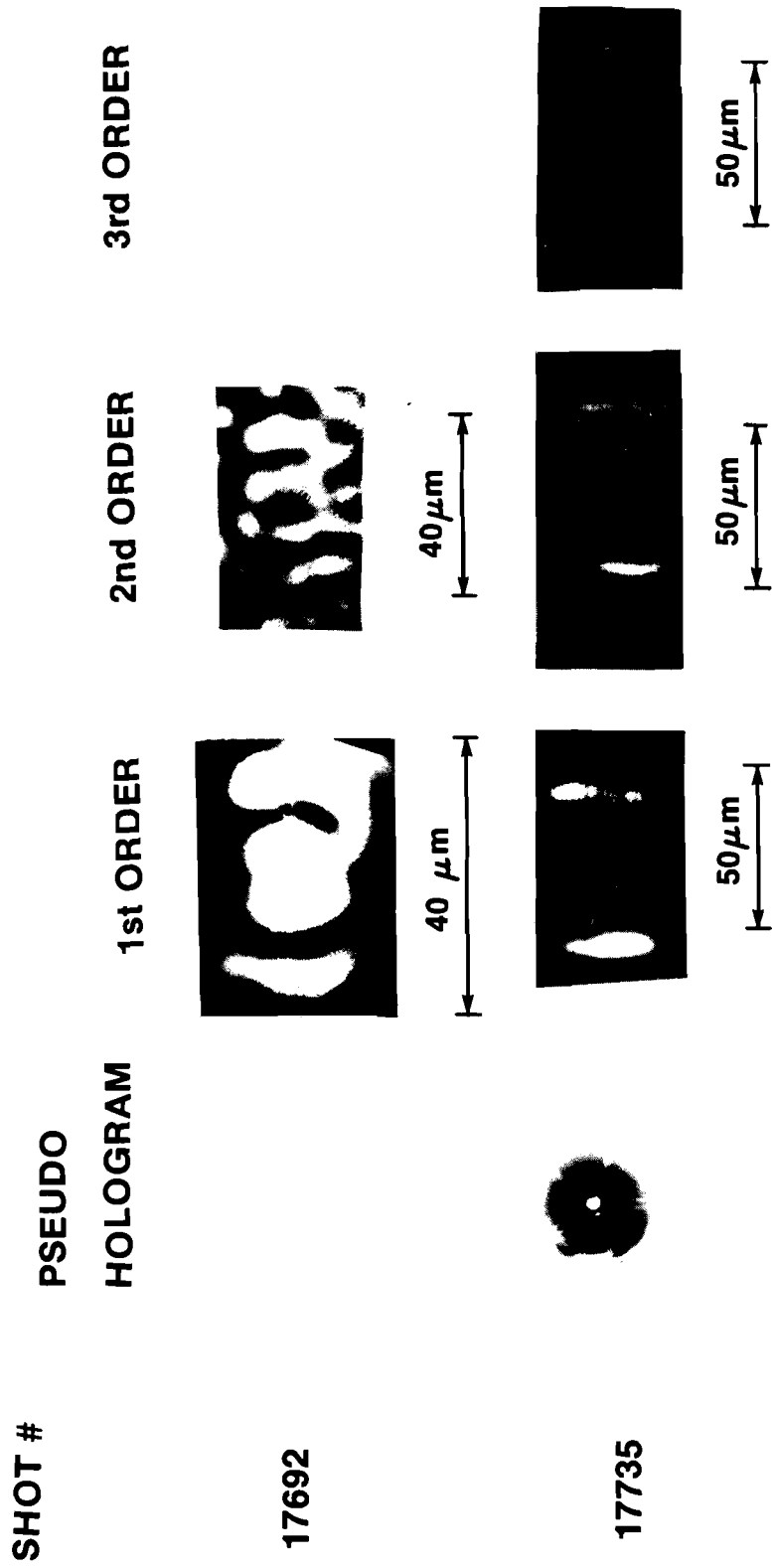


Figure 3.20  
 Shot # 17692: Reconstruction of Au coated microballoon. The hologram was bleached and fixed.  
 Shot # 17735: Reconstruction of a stalk. Compression is not achieved.

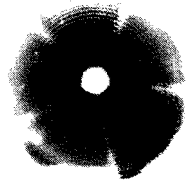
fixed. All the silver halides were dissolved and we were left with the surface relief image on the emulsion. The reconstruction at first order shows the typical shell and core structure. But, at the second order we see the inner structure. Also, the actual dimension of the shell is considerably smaller than what it might appear to be in the first order. The appearance of the inner ring in the second order reconstruction in Fig. 3.20 (shot #17692) is unusual for this kind of experiment. In a typical x-ray pinhole camera photograph of an imploded gas filled glass microballoon, only shell and core structure is observed. Since in this shot we used only 1 mill of Be foil, it is reasonable to suggest that the emitted soft x-rays may have been the origin for this structure. In x-ray pinhole camera the filters used are usually thicker and so the photograph represents effects due to harder radiation. Fig. 3.20 (shot #17735) shows the reconstructions of a stalk irradiated by 4 laser beams. The pseudohologram was previously used to determine the magnification of the system. From Fig. 3.20 (shot #17735) we can determine the thickness of the hot material at the surface of the glass with a resolution of about  $3\mu\text{m}$ . At the third order it is about  $3.5\mu\text{m}$ . In Fig. 3.21 the case of an 8.6 At Ne filled microballoon is shown. The shell is very faint and the core is very large. At the third order some indication of split core is shown.

The last three shots were done on  $\text{CD}_2$  foam. This is a solid microballoon specially prepared to have low density. Since there is no glass shell we do not expect to see the usual shell-core structure which is typical of microballoons.

In Fig. 3.22 we see the reconstruction of  $0.195 \text{ gr/cc } \text{CD}_2$  micro-

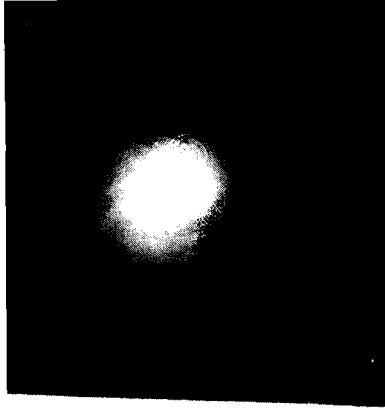
SHOT #

PSEUDO  
HOLOGRAM



17737

1st ORDER



40  $\mu\text{m}$



2nd ORDER

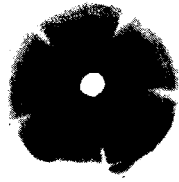


25  $\mu\text{m}$

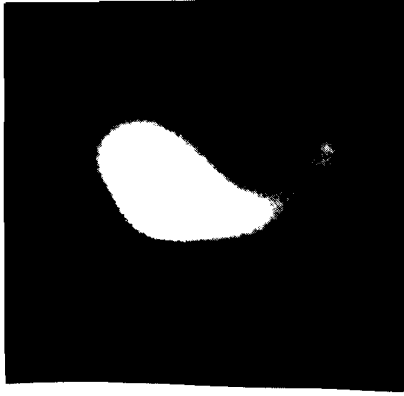


Figure 3.21  
Reconstruction of 8.6 atm. Ne filled microballoon. Compression is achieved. Fine structure  
in the core is shown.

**PSEUDOHOLOGRAM**



**1st ORDER**



**SHOT #  
17758**

**2nd ORDER**



**20  $\mu$ m**

**20  $\mu$ m**

**Figure 3.22**  
**0.195 gm.cc CD<sub>2</sub> microballoon. There is no shell; only compressed core.**

balloon. Indeed there is no shell; only the core is seen. The second order is consistent in its shape with the first order. The width of the core is about 7  $\mu\text{m}$ . In Fig. 3.23 the reconstruction of 2 foam targets is shown. The same film was used for both shots. Although good reconstruction at first order is obtained, at the second order we have artifacts and interaction between the two holograms.

### 3.10 Using 1.D. Zone Plates for Spatially Resolved Spectra of X-Ray Self-Luminous Sources.

The basic idea of high spatial resolution spatially resolved spectra is described in Fig. 3.25. It is essentially an extension to spatially resolved spectra using a slit (see Ref. [3.7]). The radiation from the pellet passes through a linear zone plate and it is diffracted by the crystal. At each wavelength a shadowgram of the region in the source emitting this wavelength is recorded. Our pseudohologram is therefore a collection of linear pseudoholograms, each of which is at a different wavelength. It is now possible to reconstruct each hologram separately to get spatially resolved spectra of the source. If higher orders are used, it is possible to get high spatial resolution.

An optical simulation of this technique is illustrated in Fig. 3.26. Here we work in transmission rather than in reflection. For an object we prepared a mask with holes; each hole was covered with a color filter. This mask was illuminated through a diffuser. The light from the mask is diffracted by the grating after passing through the zone plate and we get a shadowgram, as shown in Fig. 3.27b. In the middle the zero order is recorded. At the + and - orders, the colors are separated and we can

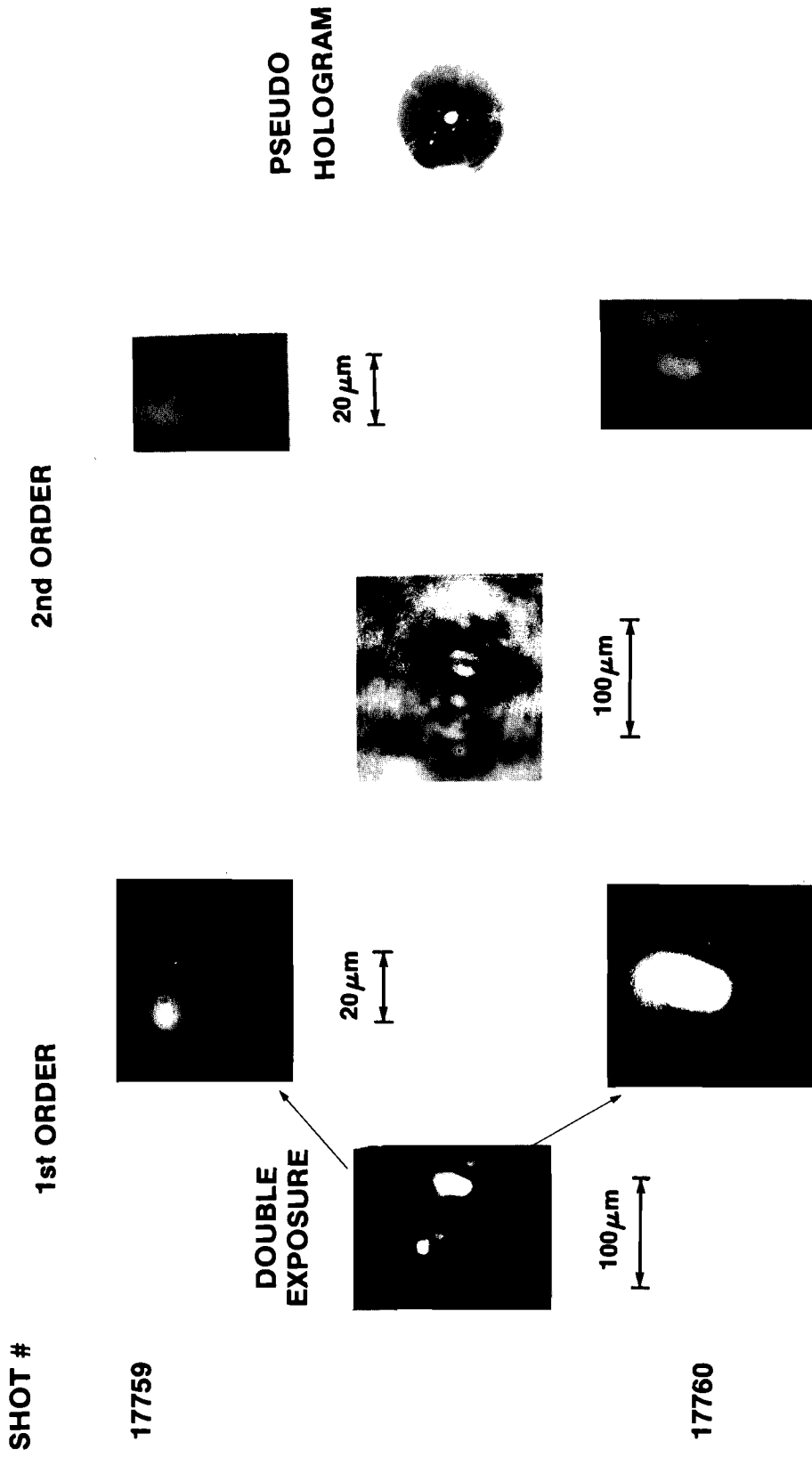


**Figure 3.23 Double exposure of 2 CD<sub>2</sub>'s.**

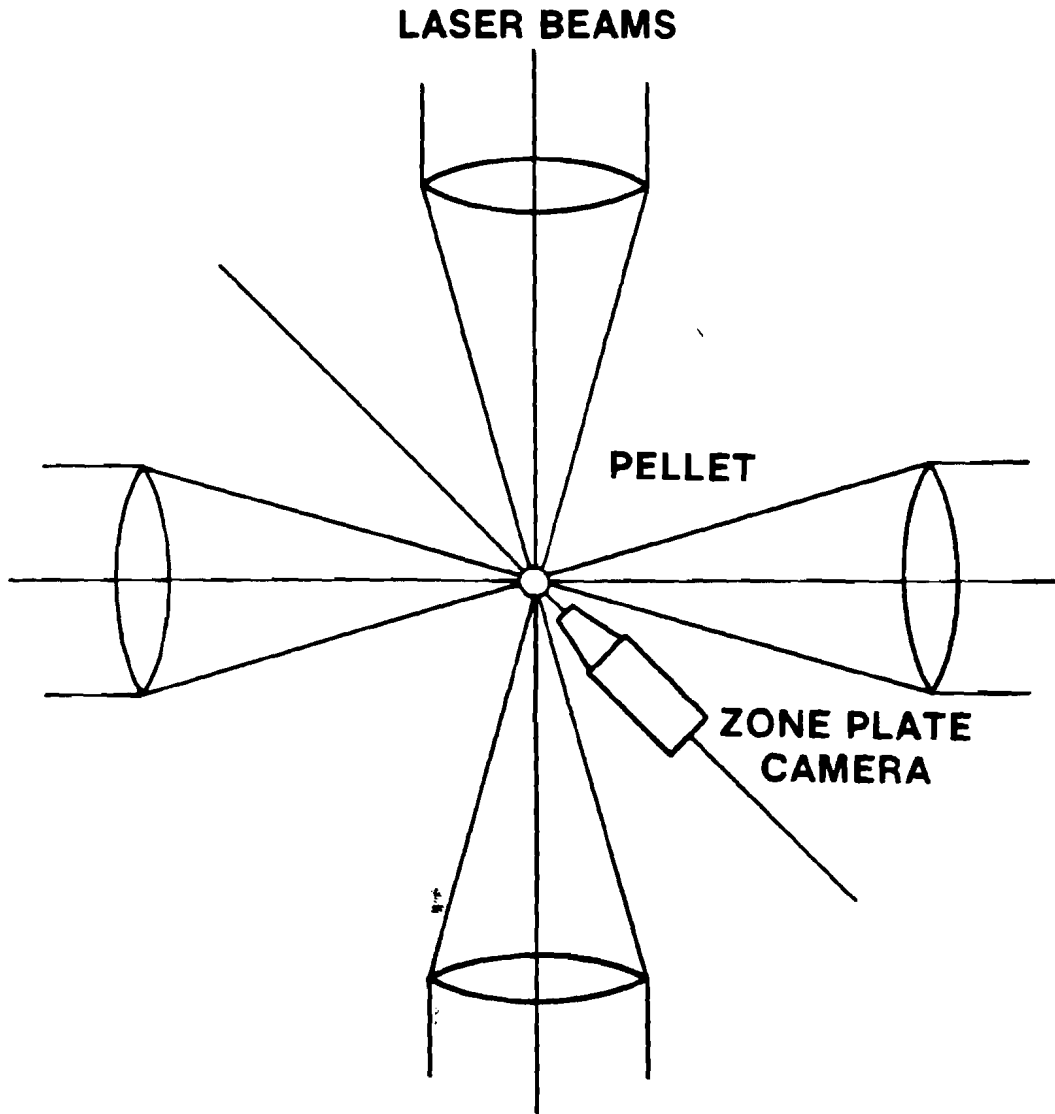


**Figure 3.24 a**  
The zone plate camera is in the plane of the four illuminating beams.

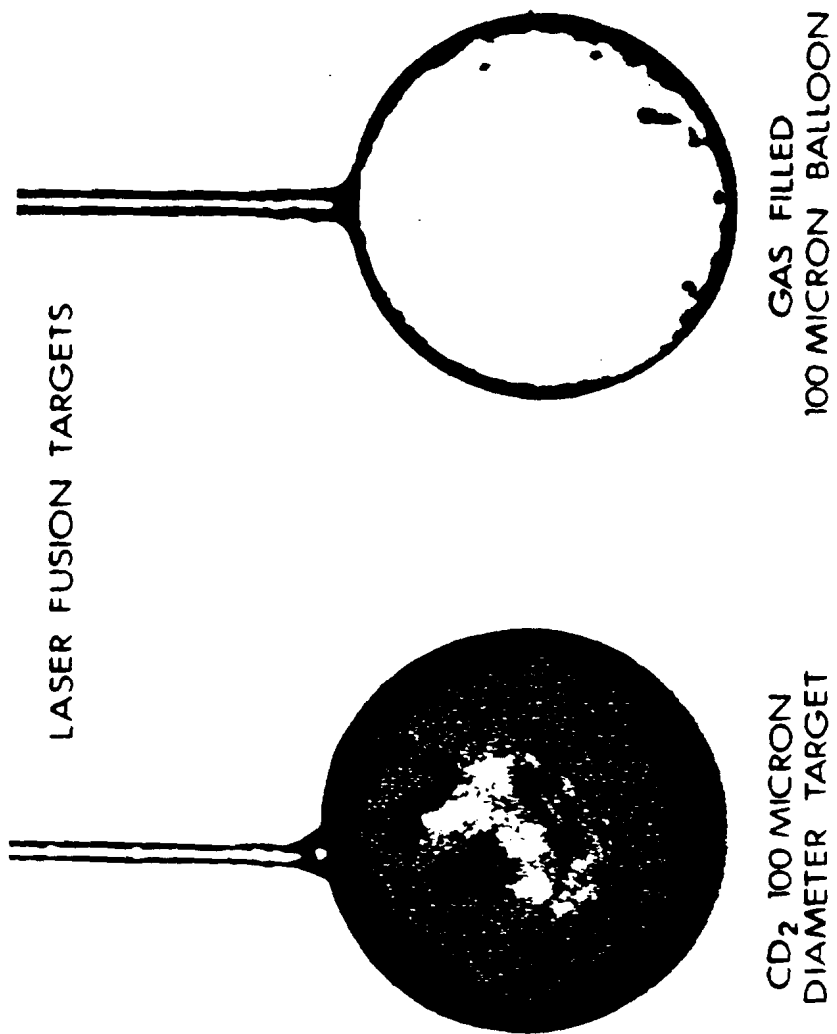


**Figure 3.24b**  
Laser fusion targets attached to glass stalks.

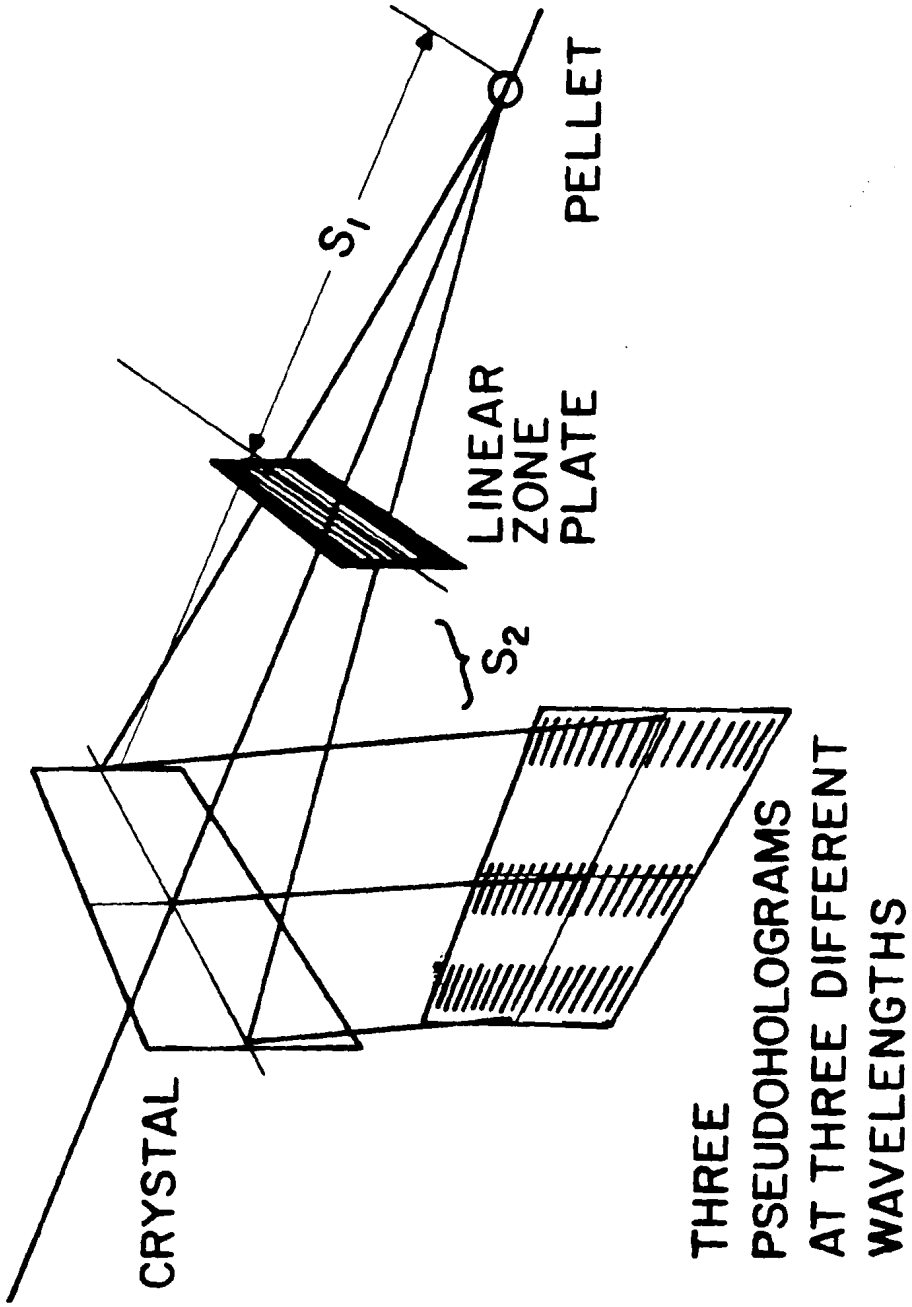


**Figure 3.25**  
Experimental configuration for recording pseudoholograms of spatially resolved spectra.

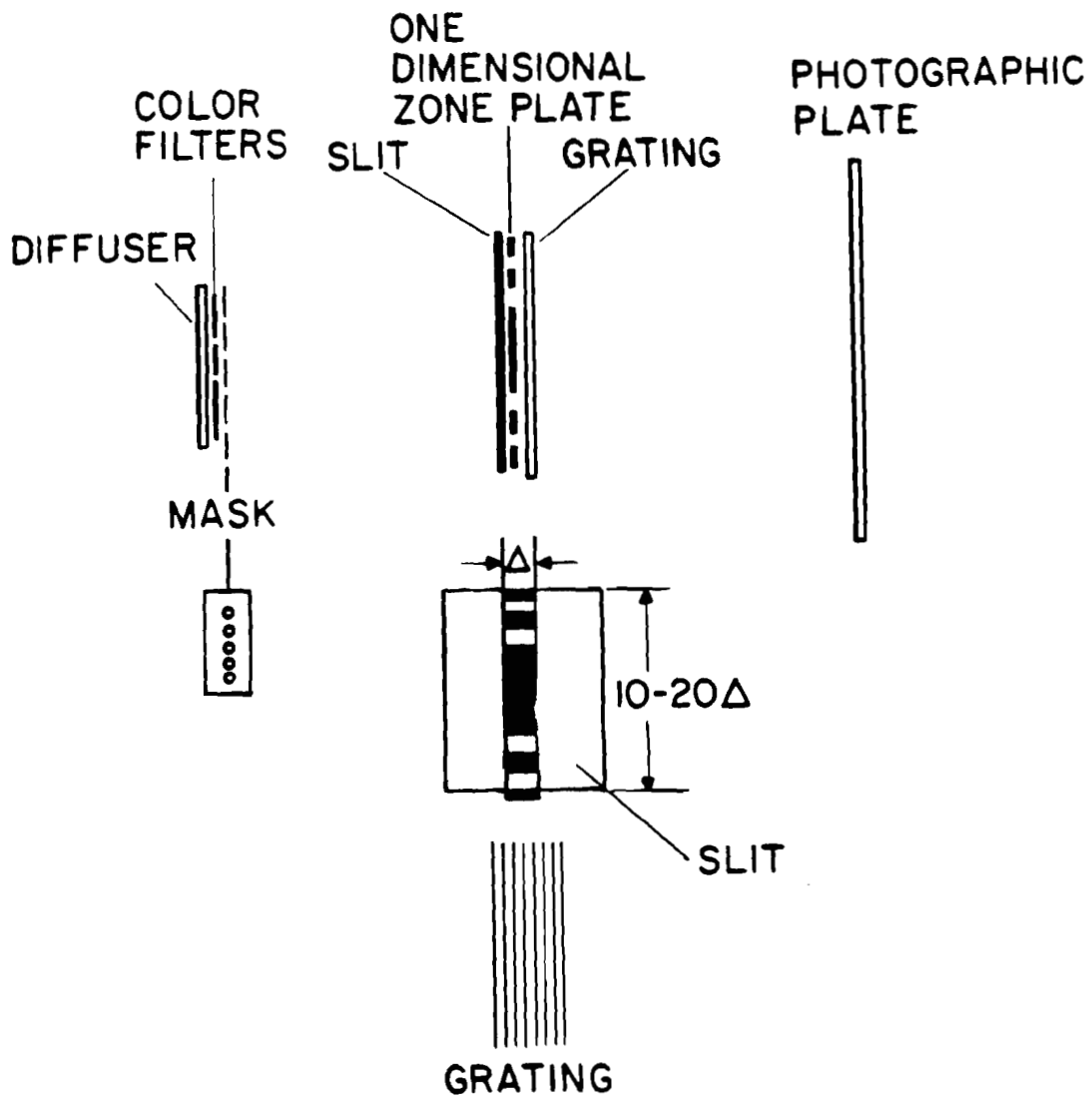


**Figure 3.26**  
Experimental configuration for optical simulation of recording of a pseudohologram of spatially resolved spectra.

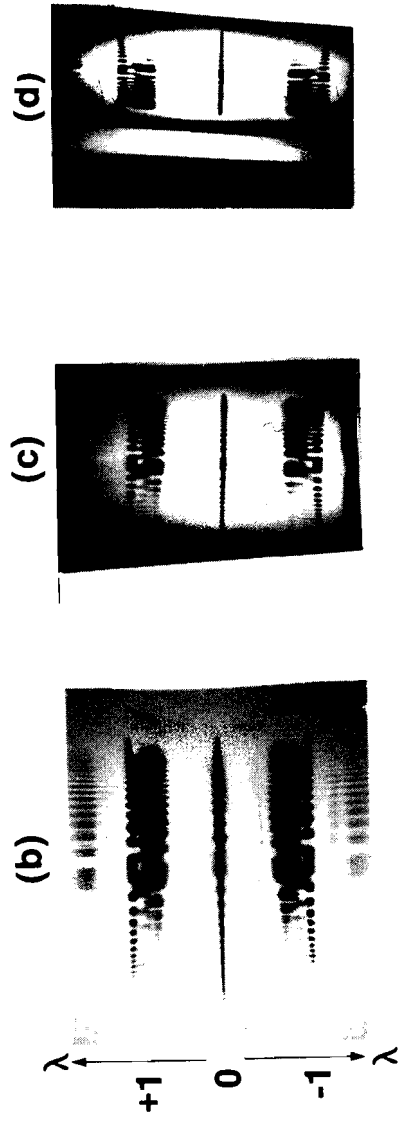
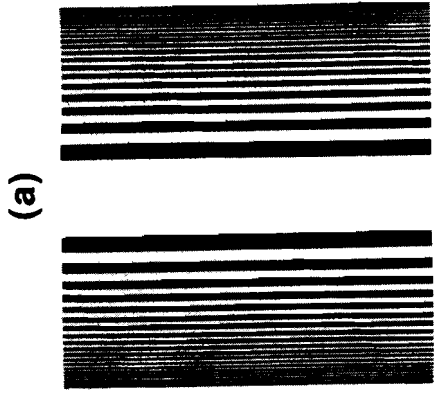


**Figure 3.27**  
 Linear pseudoholograms obtained from the simulation experiment described in Figure 3.26.  
 (a) The linear zone plate used, (b) the original pseudohologram, (c) first reduction with anamorphic lens, (d) second reduction.

observe different linear pseudoholograms at different wavelengths. In order to reconstruct we have to demagnify the hologram to get a convenient focal length. At the same time we would like to avoid the demagnification in the direction of the wavelength information in order not to decrease the spectral resolving power. We thus need a cylindrical lens that will reduce one dimension while keeping the other dimension unchanged. The only anamorphic system that is commercially available has at most 2.5X reduction capability. Since we need at least 6X reduction, we had to reduce in two steps, as shown in Fig. 3.27c and 3.27d. Finally, we reduced the pseudohologram by an additional 2X reduction with a macrolens. This is done to obtain a convenient focal length for the reconstruction.

However, the quality of the pseudohologram deteriorates because of so many photographic processes and we expect severe problems in the reconstruction.

The reconstructions are shown in Fig. 3.28. Fig. 3.28c is the object. Fig. 3.28a is the first order reconstruction and the spectra of the different holes are spatially resolved. In Fig. 3.28b the 2nd order reconstruction is shown. The signal to noise ratio is very low but the two blue holes are resolved.

The reconstruction was done using a He-Ne laser in a configuration similar to that described in Fig. 3.7(3).

To avoid a decrease in signal to noise ratio, a special cylindrical lens was designed and is being built. This cylindrical lens reduces one direction  $1\frac{1}{4}$  times while keeping the other direction unchanged. We hope that with such a lens we will be able to obtain much

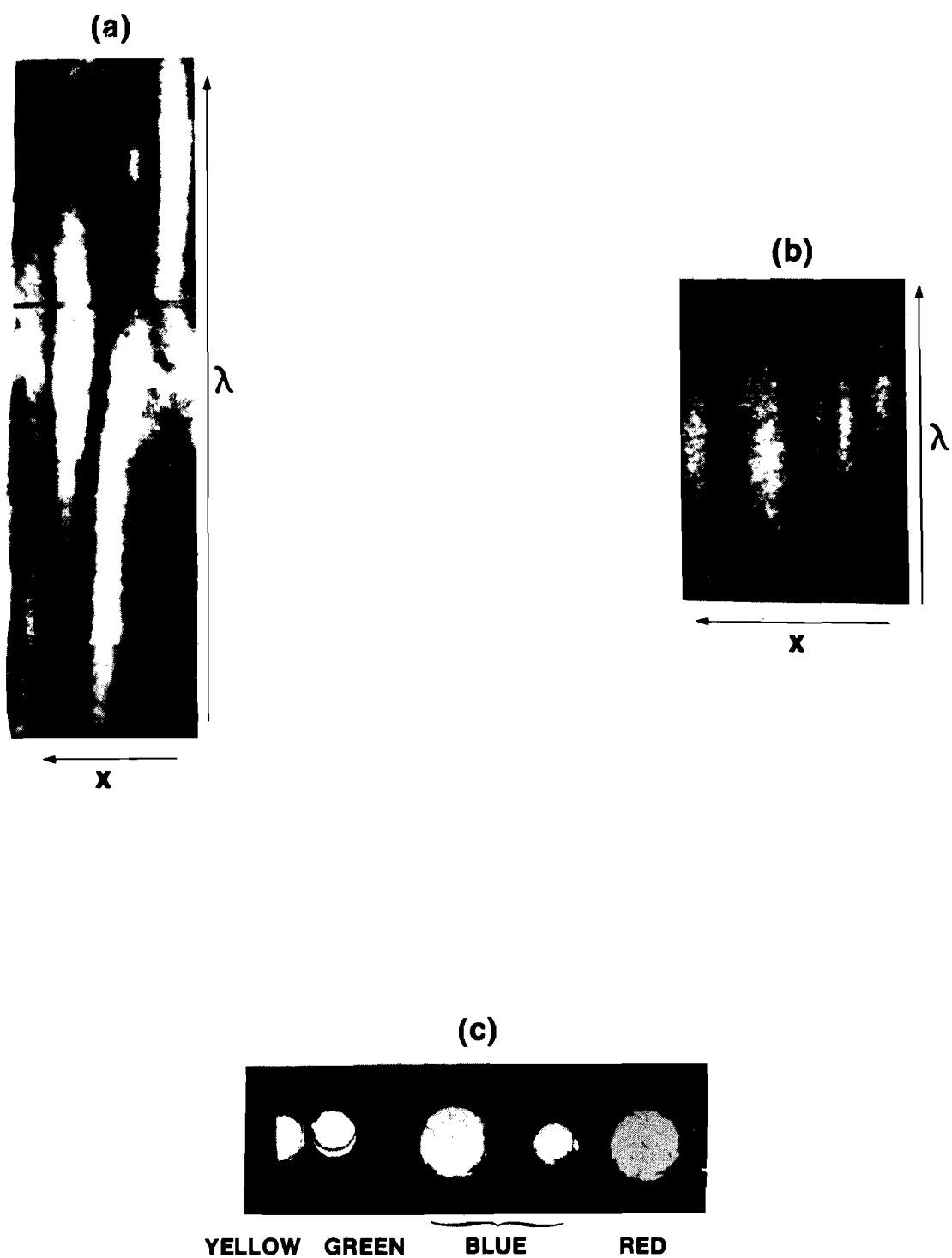


**Figure 3.28**  
Experimental results of the optical simulation experiment in spatially resolved spectroscopy. (a) First order reconstruction, (b) second order reconstruction, (c) the original object.

higher quality reconstructions than those shown in Fig. 3.28. In Fig. 3.29 the possibility of obtaining streaked one-dimensional pseudohologram is illustrated. Instead of using a slit in an x-ray streak camera, we can use a one-dimensional zone plate. One-dimensional pseudohologram is thus formed on the fluorescent screen at a time  $t_0$ , say, and recorded on a piece of film. At a later time  $t_1$ , the voltage across the plates will cause the electrons emitted from the gold cathode to shift and a different pseudohologram will be formed on the fluorescent screen. As in the case of spatially resolved spectroscopy, we can now reduce one direction to avoid decreasing the time resolution and reconstruct. This technique should enable one to get in 3rd order reconstructions, 2-3 $\mu$ m spatial resolution while maintaining the high temporal resolution in the x-ray streak camera.

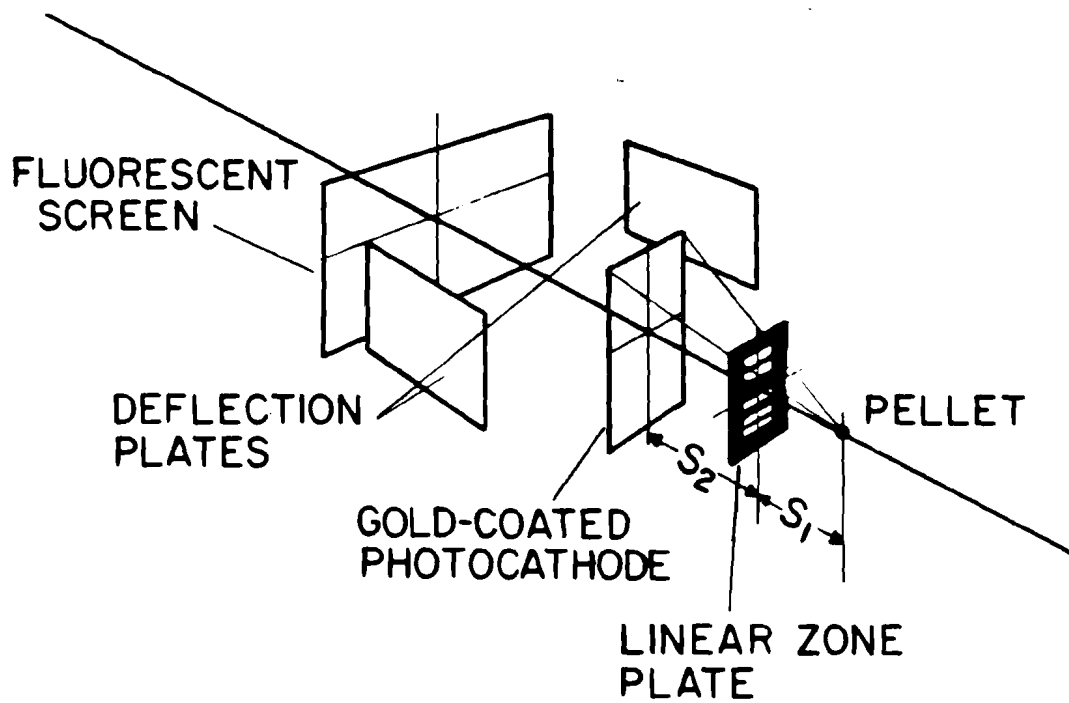


**Figure 3.29**  
Experimental configuration for recording a streaked pseudohologram. Linear pseudoholograms will appear at different locations on the fluorescent screen because the electrons are deflected during the emission from the pellet.

### 3.11 REFERENCES

- 3.1 D. J. Stigliani, Jr., R. Mittra, and R. Semonin, "Resolving power of a zone plate", J. Opt. Soc. Am., 57, 610 (1967).
- 3.2 a. H. H. M. Chau , "Properties of Two overlapping zone plates of different focal length", J. Opt. Soc. Am., 60, 255 (1970).  
b. H. H. M. Chau , "Moiré Patterns Resulting from Superposition of Two Zone Plates", Appl. Opt., 8, 1707 (1969).  
c. G. Oster, M. Wassrman, C. Zwerling, " Theoretical Investigation of Moiré Patterns", J. Opt. Soc. Am. 54, (1969).
- 3.3 a. Van G. Elwert Feitzinger, "The Image Improvement of Field Sources with Zone Plates, Especially of the Sun and Soft X Region", Optik, 31, 600 (1970).  
b. P. N. Keating, R. K. Mueller and T. Sawatari, "Fresnel Zone-Plate Spectrometer with Central Stop", J. Opt. Soc. Am., 62, 945 (1972).
- 3.4 N. M. Ceglie, "Zone Plate Imaging of Laser Produced Plasmas", Ph.D. Thesis, M.I.T., Aug. 1976, p. 130.
- 3.5 Laser Program Annual Report 1975, Lawrence Livermore Laboratory, p. 475.
- 3.6 Annual Report Laboratory of Laser Energetics, University of Rochester, 1977.
- 3.7 B. Yaakobi and A. Nee, "Spatially Resolved and Stark-Broadened X-Ray Lines from Laser-Imploded Targets", Phys. Rev. Let. 36, 1077 (1976).

CHAPTER IV

SUMMARY AND SUGGESTIONS FOR FURTHER INVESTIGATIONS

Summarizing the contributions of this work, suggestions for further analysis and experimentation will be pointed out. The potential of high order pseudoholography using zone plates for obtaining high resolution x-ray images has been demonstrated. The main results from the study of the analogies between zone plates and diffraction gratings are the following. The on-axis intensity of light focused by a Fresnel zone plate is equal at all orders. The on-axis intensity in high orders in zone plates depends strongly upon the shape of the individual zone. Smoothing the zone edges tends to decrease the efficiency at higher orders. Bleaching of pseudoholograms may be a useful technique to enhance high order reconstructions. One of the most important limitations on the pseudoholographic technique is the diffraction effects in the recording step of the pseudohologram. A rough rule of thumb was found for determining the geometrical configuration where diffraction effects are relatively unimportant. The stationary phase method was used to derive expressions for the diffraction effects. These expressions need to be evaluated numerically in order to get a reliable criterion. This problem should be tackled experimentally in order to find the upper limit on the wavelength of the soft x-ray radiation that is still useful in producing efficient pseudoholograms. The formal mathematical framework of pseudoholography is rederived this time including the reconstructions at higher orders. The theoretical study predicts practical submicron resolution. The study of unconventional zone plate design is initiated in order to improve the efficiency at high order resolutions. More research has to be done, however, to obtain an optimal zone plate design.

Investigations of the speckle noise at high order reconstructions include the film grain and the serration introduced by manufacturing processes in the zone plate structure. The grain noise could be modeled and expressions were derived. The speckle noise introduced by the serration is very hard to model and further research should be done. Computer simulations are a convenient way to investigate the various capabilities of various zone plates. A computer code that simulates the propagation of an optical field through an optical system was modified and the transverse intensity distributions were calculated for various zone plates. Two dimensional zone plates are found to be much more efficient for high order reconstructions than the one dimensional zone plates. Also, a computer program was written for calculating the intensity distributions along the optical axis. This program can be used to design a zone plate with a predetermined high order focusing capability. A third program was written for simulating the recording of a pseudohologram. The propagation code mentioned above is then used to reconstruct the recorded pseudohologram. Effects of the  $\gamma$  of the film on the quality of the reconstruction at various orders were investigated. The important conclusion is that by controlling both the  $\gamma$  and the zone plate design we can improve the quality of the reconstructions. A detailed study using these programs should be carried on to design an efficient pseudoholographic process.

Optical simulation experiments demonstrate the increase of resolution in high order reconstructions. The appearance of artifacts in the reconstructions depends strongly on the  $\gamma$  of the developed

pseudohologram, and a fidelity test of the technique is clearly warranted. Combining results of both computer simulation and experimental investigation will probably result in a more successful zone plate camera design. Results from some pellet compression experiments are shown demonstrating an increase of resolution at higher orders.

The application of zone plate pseudoholography to imaging of imploded pellets is by no means the only one. In fact, the backlighting technique, used in this work for determining the resolution of the system, may turn out to be a useful diagnostic tool for characterizing multicoated microballoons, where optical methods are impractical. Also, x-ray microscopy with submicron resolution of backlighted biological specimens seems feasible.